TRANSIENT ELECTROKINETIC PHENOMENA IN HYDROPHOBIC MICROFLUIDIC SUBSTRATES

A Dissertation

Presented to the Faculty of the Graduate School

of Cornell University

in Partial Fulfillment of the Requirements for the Degree of

Doctor of Philosophy

by

Vishal Tandon

May 2011

TRANSIENT ELECTROKINETIC PHENOMENA IN HYDROPHOBIC MICROFLUIDIC SUBSTRATES

Vishal Tandon, Ph.D.

Cornell University 2011

In this work we characterize electrokinetics in hydrophobic microfluidic substrates with aqueous working solutions as a function of the history of the fluid–solid interface. We utilize time-resolved streaming potential and current monitoring experiments to show that the electrokinetic potential in Zeonor and TOPAS substrates is a function of time after (i) initial formation of the fluid–solid interface, and (ii) after ethanol–water solvent exchanges. In these systems, the electrokinetic potential is initially large in magnitude, and decays exponentially with a time constant that is on the order of hours. We further show that the kinetics of the decay are affected by exposure to electric fields, and the ambient pressure of air surrounding the system. These data suggest that the state of dissolved gases in solution must be considered among the parameters that affect the electrokinetic potential of hydrophobic surfaces with aqueous solutions.

BIOGRAPHICAL SKETCH

Vishal was born in Southern California in 1984. His parents immigrated to the United States from India, and both have Ph.D.s in technical backgrounds. As a result, Vishal was exposed to science from a very early age, and throughout most of his life, expected to ultimately go to graduate school and earn a Ph.D. in a scientific field (as a child, he wanted to become a nuclear physicist, because he thought it was "cool").

Vishal became interested in bioengineering in high school, while learning about ATP synthase in his AP Biology class. The idea of a machine that could perform energy conversion with efficiency on the order of 90% (No, I'm not writing a reference for this) inspired Vishal to move into a scientific field that had the potential to harness this biomolecular machinery. He began his undergraduate education at UC Berkeley (Go Bears!) as a bioengineering major in 2001, and graduated in 2005 with highest honors. Toward the end of his undergraduate career, he was exposed to microfluidics and electrokinetics in Professor Luke Lee's MEMS course. He began working on these topics in the Kirby research lab at Cornell University in 2005.

In addition to research, Vishal has taken an interest in teaching. He was awarded an NSF GK-12 fellowship, and as part of the GK-12 program, developed and implemented a curriculum that brought cutting edge microfluidics research into a high school classroom. Outside of academia, Vishal has interests in tennis, basketball (he is a huge Lakers fan), cooking, and has developed recent interests in music and dance (though he has a long way to go in these interests).

ACKNOWLEDGEMENTS

Above all, I would like to acknowledge my parents, Komal and Jawahar Lal Tandon, for their continuing support and guidance throughout my life.

I would like to thank my advisor, Professor Brian J. Kirby, for all of his help throughout this process. He works to not only produce the highest quality research, but is a superlative mentor as well. All of his students have become much better writers, speakers, teachers, and researchers as a result of working with him. I would also like to thank my committee members, Professors Abraham D. Stroock and Gerald W. Feigenson. I was very lucky to find two professors with genuine interest and knowledge in my field to serve on my committee.

My friends and colleagues have given me invaluable assistance and advice during the course of my doctoral work. From Kirby Lab, I would like to thank Wyatt C. Nelson, Aditya N. Sharma, and Sharath K. Bhagavatula, who have all contributed to this project. Benjamin G. Hawkins and Alex C. Barbati have provided useful discussions, and have helped me by being more "handy" than I am. Sowmya Kondapalli helped me immensely with my GK-12 work by designing and fabricating devices, with assistance from Srinitya Arasanipalai. From outside of the Kirby Lab, I would like to thank Bernardo Cordovez, Juan P. Salazar, Edgar Cuji, and Michael T. Tolley for their help and advice.

From the GK-12 program, I would like to thank the following people: Walter Peck and his students for allowing me to teach in their classroom; Michael Shuler, Chris B. Schaffer, and Shivaun Archer for their guidance and suggestions; Nev Singhota and Kevin Dilley for their organizational efforts.

Finally, I would like to thank Marcia Sawyer (Sibley School of Mechanical and Aerospace Engineering) and Belinda Floyd (Biomedical Engineering) for helping to make things run smoothly.

TABLE OF CONTENTS

LIST OF TABLES

LIST OF FIGURES

CHAPTER 1

INTRODUCTION

The primary goal of this work is to characterize electrokinetics in hydrophobic microfluidic substrates with aqueous working solutions as a function of the history of the fluid-solid interface. Electroosmosis, the motion of fluids due to applied electric fields, is a useful mode of transport in microfluidic devices, as it scales favorably when compared to pressure driven flow as the size of the channel is reduced, and it is easier to implement in portable devices than mechanical pumps [1]. However, accurate prediction of electrokinetic actuation for device design requires rigorous models for interfacial charge formation as well as diffuse and condensed ion distributions. While the interfacial properties of some microfluidic substrates, such as silica, have been well-studied [2], interfacial properties are in dispute for many polymeric substrates [3–5].

Polymer substrates are attractive for microfluidics applications owing to their low cost, relative ease of fabrication, and potential for favorable biological, chemical, and optical properties [6–9]. Many polymers are hydrophobic, however, and the interfacial properties of hydrophobic substrates are poorly understood. While some have reported that electrokinetic actuation in hydrophobic polymers is impossible or unpredictable [10–12], others have measured significant ζ-potentials in hydrophobic substrates [3,4,6,13–16]. Analytical modeling of electrokinetics in hydrophobic substrates is challenging because the electrical, chemical, and fluid velocity boundary conditions are poorly defined. Molecular dynamics simulations are also challenging because long range electrostatic interactions between water molecules in aqueous solutions limit both the number of simulated molecules as well as the duration of the simulation [17–24]. Despite the complexity of hydrophobic substrates, measurements of material properties inferred from electrokinetics experiments in varied systems are often in agreement [4],

suggesting that accurate prediction of electrokinetic behavior is possible through careful consideration of slip, surface chemistry, and interfacial structure.

1.1 Summary of Experimental Research

In the following chapters, we present both a survey of literature and experimental data on electrokinetics in hydrophobic microfluidic substrates. The scope of this work is limited to aqueous solutions with small electrolytes; it excludes discussion of large amphipathic and organic surfactants. Throughout this work, silica is used as a model hydrophilic substrate for comparison, and the cyclic olefin copolymers TOPAS and Zeonor are the primary hydrophobic substrates that were studied in experiments.

In general, precise descriptions of electrokinetic phenomena require careful understanding of (i) the origin of interfacial charge, (ii) well-defined fluid velocity boundary conditions, and (iii) models for diffuse and condensed ion distributions [1]. Hydrophobic substrates are particularly challenging because the origin of charge is unknown, and uncertainty regarding slip leads to poorly defined fluid velocity boundary conditions [5,25]. Most hydrophobic polymers do not have reactive surface groups or a strong affinity for ions, but often exhibit electrokinetic potentials on the same order as charged hydrophilic surfaces (such as glass), and have similar pH dependence. Possible charge sources include (a) acid-base dissociation of surface groups from impurities, (b) preferential adsorption of electrolyte ions, and (c) adsorption of hydroxyl ions. In **Chapter 2**, we discuss these potential charge sources in a review of literature and experimental data relevant to understanding the origin of charge in hydrophobic substrates.

Some of the complexity in understanding the origin of charge at water-hydrophobe interfaces arises from the molecular/supramolecular structure of water at the fluid-solid

interface. Postulated structures include regions of reduced or depleted water density [19, 26, 27], ice-like hydrogen bonded water molecule networks [19, 22, 28], and nanobubbles [29]. Depletion layers and water molecule networks impact ion adsorption onto the fluid-solid interface, and are therefore important factors in understanding the origin of charge. Nanobubbles are of particular interest, since their presence would affect both interfacial charge formation and the fluid mechanical boundary condition, and their thermodynamic instability [25, 29–32] could lead to unpredictable or fluctuating electrokinetic behavior in hydrophobic systems. While no-slip boundary conditions on the fluid velocity are normally assumed in microfluidic systems [7, 33] (an accurate description for hydrophilic substrates [34–37]), hydrophobic substrates have been shown to have significant slip [36–53]. In **Chapter 3**, we survey data on slip and interfacial structures, and discuss their impact on electrokinetic phenomena.

The presence of unstable interfacial structures, such as nanobubbles, putatively suggests boundary conditions at the fluid-solid interface that change with time. This would result in electrokinetic behavior in hydrophobic substrates that is a function of the time-history of the fluid-solid interface. In **Chapter 4**, we present experimental data showing that the electrokinetic properties of hydrophobic, TOPAS microfluidic substrates do indeed vary with time. We furthermore show that these phenomena are sensitive to ethanol-water solvent exchanges, and to exposure to electric fields. We postulate that the mechanism for these transient electrokinetic phenomena is related to unstable interfacial nanobubbles that dissolve over time. The presence of interfacial nanobubbles is expected to lead to an apparent slip, and an inflated apparent ζ-potential magnitude that decays over time as the nanobubbles dissipate.

Both slip [54] and nanobubbles [55–59] have been shown to depend on the type and/or amount of gas dissolved in solution. The concentration of gas in solution de-

pends on the solvent, the gas, the ambient temperature, and the pressure of the gas in equilibrium with the solution. In **Chapter 4**, we show that switching from a solvent with relatively high gas solubility, ethanol, to one with relatively low gas solubility, water, leads to a temporary increase in the magnitude of the ζ potential. In **Chapter 5**, the time-dependence of the ζ potential is shown to also depend on the ambient pressure of air in contact with the working solution. The sensitivity of these systems to ethanol-water solvent exchanges and ambient pressure strongly suggest that the state of dissolved gases in solution must be considered among the parameters that affect the ζ-potential.

1.2 Summary of Educational Outreach

Over the course of this research, we also developed methods for introducing microfluidics education to students at the high school level. Three microfluidics-based laboratory exercises, discussed in **Chapter 6**, were developed and implemented in a high school physics classroom. One exercise was designed to give students the tools needed to qualitatively characterize flows. In the other two exercises, students characterized flows in PDMS microfluidic devices. Topics covered in these exercises included Reynolds number, turbulence, viscosity, hydraulic resistance, compressibility, mixing, and reversibility.

BIBLIOGRAPHY

[1] R.J. Hunter. *Zeta Potential in Colloid Science*. Academic Press, London, 1981.

[2] B.J. Kirby and E.F. Jr. Hasselbrink. Zeta potential of microfluidic substrates: 1. theory, experimental techniques, and effects on separations. *Electrophoresis*, 25:203–213, 2004.

[3] B.J. Kirby and E.F. Jr. Hasselbrink. Zeta potential of microfluidic substrates: 2. data for polymers. *Electrophoresis*, 25:203–213, 2004.

[4] V. Tandon, S.K. Bhagavatula, W.C. Nelson, and B.J. Kirby. Zeta potential and electroosmotic mobility in devices fabricated from hydrophobic polymers: 1. the origins of charge. *Electrophoresis*, 29:1092–1101, 2008.

[5] V. Tandon and B.J. Kirby. Zeta potential and electroosmotic mobility in devices fabricated from hydrophobic polymers: 2. slip and interfacial water structure. *Electrophoresis*, 29:1102–1114, 2008.

[6] P. Mela, A. van den Berg, Y. Fintschenko, E.B. Cummings, B.A. Simmons, and B.J. Kirby. The zeta potential of cyclo-olefin polymer microchannels and its effects on insulative (electrodeless) dielectrophoresis particle trapping devices. *Electrophoresis*, 26:1792–1799, 2005.

[7] H.A. Stone, A.D. Stroock, and A. Ajdari. Engineering flows in small devices: Microfluidics toward a lab-on-a-chip. *Annual Review of Fluid Mechanics*, 36:381–411, 2004.

[8] J.C. McDonald, D.C. Duffy, J.R. Anderson, D.T. Chiu, H. Wu, O.J.A. Schueller, and G.M. Whitesides. Fabrication of microfluidic systems in poly(dimethylsiloxane). *Electrophoresis*, 21:27–40, 2000.

[9] B.G. Hawkins, A.E. Smith, Y.A. Syed, and B.J. Kirby. Continuous-flow particle separation by 3d insulative dielectrophoresis using coherently shaped, dc-biased, ac electric fields. *Analytical Chemistry*, page Accepted, 2007.

[10] J. Gaudioso and H.G. Craighead. Characterizing electroosmotic flow in microfluidic devices. *Journal of Chromatography A*, 971(1):249–253, 2002.

[11] J. Kameoka, H.G. Craighead, H. Zhang, and J. Henion. A polymeric microfluidic chip for ce/ms determination of small molecules. *Analytical Chemistry*, 73:1935–1941, 2001.

[12] A. Tan, S. Benetton, and J.D. Henion. Chip-based solid-phase extraction pretreatment for direct electrospray mass spectrometry analysis using an array of monolithic columns in a polymeric substrate. *Analytical Chemistry*, 75:5504–5511, 2003.

[13] W. Schutzner and E. Kenndler. Electrophoresis in synthetic organic polymer capillaries: Variation of the electroosmotic velocity and zeta potential with ph and solvent composition. *Analytical Chemistry*, 64:1991–1995, 1992.

[14] C. Werner, H. Korber, R. Zimmermann, S. Dukhin, and H. Jacobasch. Extended electrokinetic characterization of flat solid surfaces. *Journal of Colloid and Interface Science*, 208(1):329–346, 1998.

[15] L.E. Locascio, C.E. Perso, and C.S. Lee. Measurement of electroosmotic flow in plastic imprinted microfluid devices and the effect of protein adsorption on flow rate. *Journal of Chromatography A*, 857(1):275–284, 1999.

[16] J. Caslavska and W. Thormann. Electrophoretic separations in pmma capillaries with uniform and discontinuous buffers. *Journal of Microcolumn Separations*, 13(2):69–83, 2001.

[17] C.Y. Lee, J.A. McCammon, and P.J. Rossky. The structure of liquid water at an extended hydrophobic surface. *Journal of Chemical Physics*, 80(9):4448–4455, 1984.

[18] J.R. Grigera, S.G. Kalko, and J. Fischbarg. Wall-water interface. a molecular dynamics study. *Langmuir*, 12:154–158, 1996.

[19] S.I. Mamatkulov, P.K. Khabibullaev, and RR. Netz. Water at hydrophobic substrates: Curvature, pressure, and temperature effects. *Langmuir*, 20:4756–4763, 2004.

[20] L. Joly, C. Ybert, E. Trizac, and L. Bocquet. Hydrodynamics within the electric double layer on slipping surfaces. *Physical Review Letters*, 93:257805, 2004.

[21] L. Vrbka, M. Mucha, B. Minofar, and P. Jungwirth. Propensity of soft ions for the air/water interface. *Current Opinion in Colloid and Interface Science*, 9:67, 2004.

[22] R. Zangi and J.B.F.N. Engberts. Physisorption of hydroxide ions from aqueous solution to a hydrophobic surface. *Journal of the American Chemical Society*, 127:2272–2276, 2005.

[23] D.M. Huang, C. Cottin-Bizonne, C. Ybert, and L. Bocquet. Ion-specific anomalous electrokinetic effects in hydrophobic nanochannels. *Physical Review Letters*, 98:177801, 2007.

[24] D.M. Huang, C. Cottin-Bizonne, C. Ybert, and L. Bocquet. Aqueous electrolytes near hydrophobic surfaces: Dynamic effects of ion specificity and hydrodynamic slilp. *Langmuir*, 24(4):1442–1450, 2007.

[25] E. Lauga, M.P. Brenner, and H.A. Stone. *Microfluidics: The No-Slip Boundary Condition*. Handbook of Experimental Fluid Dynamics. Springer, New York, 2005.

[26] A. Poynor, L. Hong, I.K. Robinson, S. Granick, Z. Zhang, and P.A. Fenter. How water meets a hydrophobic surface. *Physical Review Letters*, 97:266101, 2006.

[27] D.A. Doshi, E.B. Watkins, J.N. Israelachvili, and J. Majewski. Reduced water density at hydrophobic surfaces: Effect of dissolved gases. *PNAS*, 102(27):9458–9462, 2005.

[28] L.X. Dang and T. Chang. Molecular mechanism of ion binding to the liquid/vapor interface of water. *Journal of Physical Chemistry B*, 106:235–238, 2002.

[29] P. Attard, M.P. Moody, and J.W.G. Tyrell. Nanobubbles: the big picture. *Physica A*, 314:696–705, 2002.

[30] P. Attard. Electrolytes and the electric double layer. *Advances in Chemical Physics*, 92:1–159, 1996.

[31] P. Attard. Thermodynamic analysis of bridging bubbles and a quantitative comparison with the measured hydrophobic attraction. *Langmuir*, 16:4455–4466, 2000.

[32] P. Attard. Nanobubbles and the hydrophobic attraction. *Advances in Colloid and Interface Science*, 104:75–91, 2003.

[33] T.M. Squires and S.R. Quake. Microfluidics: Fluid physics at the nanoliter scale. *Review of Modern Physics*, 77:977–1026, 2005.

[34] E. Bonaccurso, M Kappl, and H-J. Butt. Hydrodynamic force measurements: Boundary slip of water on hydrophilic surfaces and electrokinetic effects. *Physical Review Letters*, 88(7):076103, 2002.

[35] E. Bonaccurso, H-J. Butt, and V.S.J. Craig. Surface roughness and hydrodynamic boundary slip of a newtonian fluid in a completely wetting system. *Physical Review Letters*, 90(14):144501, 2003.

[36] H. Hervet and L. Leger. Flow with slip at the wall: From simple to complex fluids. *C.R. Physique*, 4:241–249, 2003.

[37] C.L. Henry, C. Neto, D.R. Evans, S. Biggs, and V.S.J. Craig. The effect of surfactant adsorption on liquid boundary slippage. *Physica A*, 339:60–65, 2004.

[38] U.-C. Boehnke, T. Remmler, H. Motschmann, S. Wurlitzer, J. Hauwede, and Th. M. Fischer. Partial air wetting on solvophobic surfaces in polar liquids. *Journal of Colloid and Interface Science*, 211:243–251, 1999.

[39] C-H. Choi, K. Johan, A. Westin, and K.S. Breuer. Apparent slip flows in hydrophilic and hydrophobic microchannels. *Physics of Fluids*, 15(10):2897–2902, 2003.

[40] N.V. Churaev, J. Ralston, I.P. Sergeeva, and V.D. Sobolev. Electrokinetic properties of methylated quartz capillaries. *Advances in Colloid and Interface Science*, 96:265–278, 2002.

[41] N.V. Churaev, V.D. Sobolev, and A.N. Somov. Slippage of liquids over lyophobic solid surfaces. *Journal of Colloid and Interface Science*, 97:574–581, 1984.

[42] P. Joseph and P. Tabeling. Direct measurement of the apparent slip length. *Physical Review E*, 71:035303, 2005.

[43] D.C. Tretheway and C.D. Meinhart. Apparent fluid slip at hydrophobic microchannel walls. *Physics of Fluids*, 14(3):L9–L12, 2002.

[44] D.C. Tretheway and C.D. Meinhart. A generating mechanism for apparent fluid slip in hydrophobic microchannels. *Physics of Fluids*, 16(5):1509–1515, 2004.

[45] O.I. Vinogradova and G.E. Yakubov. Dynamic effects on force measurements. 2. lubrication and the atomic force microscope. *Langmuir*, 19:1227–1234, 2003.

[46] J. Baudry, E. Charlaix, A. Tonck, and D. Mazuyer. Experimental evidence for a large slip effect at a nonwetting fluid-solid interface. *Langmuir*, 17:5232–5236, 2001.

[47] C. Cheikh and G. Koper. Stick-slip transition at the nanometer scale. *Physical Review Letters*, 91(15):156102, 2003.

[48] J.J. Cho, B.M. Law, and F. Rieutord. Dipole-dependent slip of newtonian liquids at smooth solid hydrophobic surfaces. *Physical Review Letters*, 92(16):166102, 2004.

[49] O.A. Kisleva, V.D. Sobolev, and N.V. Churaev. Slippage of the aqueous solutions of cetyltrimethylammonium bromide during flow in thin quartz capillaries. *Colloid J.*, 61:263–264, 1999.

[50] D. Lumma, A. Best, A. Gansen, F. Feuillebois, J.O. Radler, and O.I. Vinogradova. Flow profile near a wall measured by double-focus fluorescence cross-correlation. *Physical Review E*, 67:056313, 2003.

[51] G. Sun, E. Bonaccurso, V. Franz, and H-J. Butt. Confined liquid: Simultaneous observation of a molecularly layered structure and hydrodynamic slip. *Journal of Chemical Physics*, 117(22):10311–10314, 2002.

[52] Yingxi Zhu and S. Granick. Limits of the hydrodynamic no-slip boundary condition. *Physical Review Letters*, 88(10):106102, 2002.

[53] Y. Zhu and S. Granick. No-slip boundary condition switches to partial slip when fluid contains surfactant. *Langmuir*, 18:10058–10063, 2002.

[54] S. Granick, Y. Zhu, and H. Lee. Slippery questions about complex fluids flowing past solids. *Nature Materials*, 2(4):221–227, 2003.

[55] L. Meagher and V.S.J. Craig. Effect of dissolved gas and salt on the hydrophobic force between polypropylene surfaces. *Langmuir*, 10:2736–2742, 1994.

[56] J. Mahnke, J. Stearnes, R.A. Hayes, D. Fornasiero, and J. Ralston. The influence of dissolved gas on the interactions betwen surfaces of different hydrophobicity in aqueous media. *Physical Chemistry Chemical Physics*, 1:2793–2798, 1999.

[57] N. Ishida, T. Inoue, M. Miyahara, and K. Higashitani. Nano bubbles on a hydrophobic surface in water observed by tapping-mode atomic force microscopy. *Langmuir*, 16:6377–6380, 2000.

[58] X.H. Zhang, X.D. Zhang, S.T. Lou, Z.X. Zhang, J.L. Sun, and J. Hu. Degassing and temperature effects on the formation of nanobubbles at the mica/water interface. *Langmuir*, 20:3813–3815, 2004.

[59] R.F. Considine, R.A. Hayes, and R.G. Horn. Forces measured between latex spheres in aqueous electrolyte: Non-dlvo behavior and sensitivity to dissolved gas. *Langmuir*, 15:1657–1659, 1999.

CHAPTER 2

ZETA POTENTIAL AND ELECTROOSMOTIC MOBILITY IN MICROFLUIDIC DEVICES FABRICATED FROM HYDROPHOBIC POLYMERS: 1. THE ORIGINS OF CHARGE

Abbreviations: **pzc**, point of zero charge; **pI**, isoelectric point; **EDL**, electrical double layer; **ATR-IR**, attenuated total reflection infrared; **XPS**, x-ray photoelectron spectroscopy; **SFG**, sum frequency generation; **SHG**, second harmonic generation; **MD**, molecular dynamics; **PTFE**, poly(tetrafluoroethylne); **PDMS**, poly(dimethylsiloxane); **PS**, polystyrene; **PE**, polyethylene; **PDFP**, plasma deposited fluoropolymer

2.1 Abstract

This paper combines new experimental data for electrokinetic characterization of hydrophobic polymers with a detailed discussion of the putative origins of charge at water-hydrophobe interfaces. Complexities in determining the origin of charge are discussed in the context of design and modeling challenges for electrokinetic actuation in hydrophobic microfluidic devices with aqueous working fluids. Measurements of interfacial charge are complicated by slip, and interfacial water structuring phenomena [2]. Despite these complexities, it is shown that (a) several hydrophobic materials, such as Teflon and Zeonor, have predictable electrokinetic properties and (b) electrokinetic data for hydrophobic microfluidic systems is most consistent with the postulate that hydroxyl ion adsorption is the origin of charge.

[0]The content of this chapter was submitted and published as a research article that is reproduced here with permission from *Electrophoresis*. This is the pre-peer reviewed version of the following article: "Zeta Potential and Electroosmotic Mobility in Devices Fabricated from Hydrophobic Polymers: 1. The Origins of Charge" [1].

2.2 Introduction

Polymers are attractive as microfluidic substrates owing to their biocompatibility, relatively low cost, ease of fabrication, and potential for both high chemical resistance and favorable optical properties [3–6]. Many commonly used polymers are hydrophobic, however, and electrokinetic actuation in hydrophobic microfluidic devices is not well-characterized owing to uncertainties in the chemistry of water–hydrophobe interfaces. This limits repeatability of experiments, accuracy of predictive models, and ultimately device design capabilities. Electrokinetic measurements in hydrophobic substrates are challenging (as evidenced by significant scatter in the data [7]) because these phenomena are difficult to measure and are sensitive to surfactants; theoretical models are also lacking because the physics of interfacial phenomena and the space of applicable input parameters are not well-defined. Most hydrophobic polymers do not have reactive surface groups or a strong affinity for ions, but often exhibit electrokinetic potentials on the same order as charged hydrophilic surfaces (such as glass), and have similar pH-dependence. In both hydrophilic and hydrophobic surfaces, accurate prediction of the electrokinetic potential depends on the veracity of models for both (a) interfacial charge formation, and (b) diffuse and condensed ion distributions. For hydrophobic surfaces in particular, these models are further complicated in that the origins of charge are less well-understood, and electrokinetic potentials inferred from experiments may be inflated due to hydrodynamic slip [2]. Despite the complexity of hydrophobic microfluidic systems, the fact that measurements of material properties inferred from electrokinetics experiments in varied systems are reproducible suggests that modeling electrokinetic behavior is possible through careful consideration of slip, surface chemistry, and surface morphology. In the sections to follow, we present general fundamental electrokinetic relations and then discuss the distinctive challenges in understanding the origins

of interfacial charge in hydrophobic microfluidic materials. In the companion to this paper [2], we present slip phenomena and interfacial molecular/supramolecular structures, and show that they are inherently coupled with surface charge. Here we focus on microfluidic devices with aqueous electrolyte solutions, and exclude discussion of large amphipathic and organic surfactants.

2.3 Fundamentals of Electrokinetics

Before we discuss the challenges that arise in characterizing hydrophobic microfluidic devices, we present a brief summary of the physical processes underlying electrokinetics in microfluidic systems in general.

2.3.1 Origins of Surface Charge

The spontaneous separation of charge at solid–liquid interfaces is ubiquitous in microfluidic devices, and is central to electrokinetic actuation of flow. Several chemical mechanisms can give rise to the spontaneous separation of charge between two phases [8]. The most relevant to microfluidics are (a) ionization of surface groups and (b) preferential adsorption of ions of one charge or the other.

(a) Ionization of surface groups

Many microfluidic substrates behave as weak acids in aqueous solutions, owing to reactivities of surface groups e.g., amines, carboxylic acids, or oxides. Glass/silica microdevices are a particularly well-studied example of such a system, due to their ubiquity in

devices used for capillary electrophoresis and other analytical techniques [9]. In glass substrates, surface silanol groups can be deprotonated, in aqueous solutions leaving a negative surface charge:

$$\mathrm{SiOH} \overset{K_a}{\rightleftharpoons} \mathrm{SiO^-} + \mathrm{H^+} \tag{2.1}$$

The pK_a for this reaction is approximately 4.7 [9]. In cases like this, where protonation/de–protonation of surface groups is the origin of charge, the charge-determining ions are $\mathrm{H^+}$ and $\mathrm{OH^-}$, and the electrokinetic properties of the system are a strong function of pH [10].

(b) Differences in affinity for ions between the solid and liquid phases

Differences in affinity between the liquid phase and the solid phase for particular ions leads to charge separation by (i) preferential adsorption of ions from an electrolyte solution onto the surface and/or (ii) preferential solution of ions from the crystal lattice of an ionic salt [8]. Many Nernstian surfaces exhibit mechanism (ii), leading to a surface potential that is well defined as a function of the salt concentration. Silver halides, such as AgI, are examples of Nernstian surfaces. Their surface potential, ζ, as a function of the silver ion concentration, $[\mathrm{Ag^+}]$, is defined by

$$\zeta = \frac{k_B T}{ze} \ln \frac{[\mathrm{Ag^+}]}{[\mathrm{Ag^+}]_{pzc}}, \tag{2.2}$$

where k_B is Boltzmann's constant, T is the temperature in K, z is the valence of the ion ($z = 1$ for AgI), e is the elementary charge, and pzc refers to the point of zero charge. Equation 2.2 assumes that as the bulk activity of $\mathrm{Ag^+}$ ions is altered, the activity of surface $\mathrm{Ag^+}$ ions remains constant. Microfluidic devices are in general not made from Nernstian materials [7, 10], but Nernstian surfaces can be useful in studying electrokinetics since their surface electrical potential boundary conditions are well-defined.

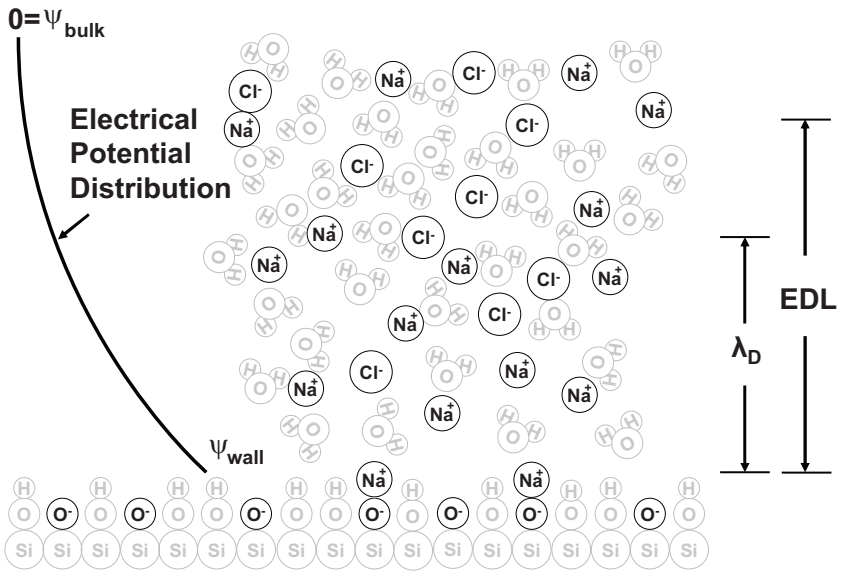

Figure 2.1: Schematic of the electrical double layer.

2.3.2 The Electrical Double Layer

The net charge density at fluid–solid interfaces coincides with an electrical potential and ion distribution structure within the fluid known as the electrical double layer (EDL). The surface charge generates an electric field, which pulls oppositely charged ions (counterions) toward the surface, and pushes like charges (coions) away from it. Counterions preferentially concentrate near the surface, effectively shielding the bulk solution from the surface charge. The shielding layer is often referred to as the Debye layer, or the EDL. A schematic diagram of the EDL is shown in figure 2.1.

Detailed descriptions of the internal structure of the EDL are often based on the Gouy–Chapman–Stern (GCS) model [11], where the EDL is comprised of a Stern layer and a diffuse layer. The Stern layer consists of counterions which are immobilized on the surface, and its thickness is dictated by the size of the ions. The diffuse layer lies just beyond the Stern layer, and is responsible for the electrokinetic phenomena relevant to microfluidic devices.

For descriptions of electroosmosis in this context, it is sufficient to treat the diffuse layer ion distribution in the Boltzmann limit in which ions are treated as point particles in a mean field. The Poisson equation for the electric charge density, ρ_e, in a medium of electrical permittivity ϵ, combined with the Boltzmann equation gives

$$\nabla^2\psi = -\frac{\rho_e}{\epsilon} = -\frac{1}{\epsilon}\sum_i n_{o,i} e z_i \exp\left(-\frac{e z_i}{k_B T}\psi\right) , \tag{2.3}$$

where ψ is the electrical potential, z_i is the valence of the *i*-th ionic species, and $n_{o,i}$ is the number density of the ith species where $\psi = 0$. A natural length scale that arises in solutions of the Poisson–Boltzman equation is

$$\lambda_D = \sqrt{\frac{\epsilon k_B T}{2e^2(\Gamma/2)}} \tag{2.4}$$

where λ_D, commonly referred to as the Debye length, is the length scale over which electrical potentials and ion distributions change and $\Gamma/2$ is the bulk ionic strength of the solution defined as:

$$\frac{\Gamma}{2} = \frac{1}{2}\sum_i n_{o,i} z_i^2 . \tag{2.5}$$

Solution of the Poisson–Boltzmann equation is non-trivial due to its non-linearity and uncertainty in the boundary conditions. While Equation 2.3 is usually sufficient for descriptions of macroscopically observable electrokinetic behavior in microdevices, the Boltzmann approximation breaks down at high electrolyte concentrations and in general fails to accurately describe ion distributions very close to the surface, where the ion size becomes important. Several, more sophisticated, theories have led to versions of the Poisson–Boltzmann Equation modified to include the effects of ion size, use of the Ornstein–Zernike equation with hypernetted chain approximations [12, 13], and semi-empirical corrections based on mean spherical approximations [14] and Monte Carlo simulations [15].

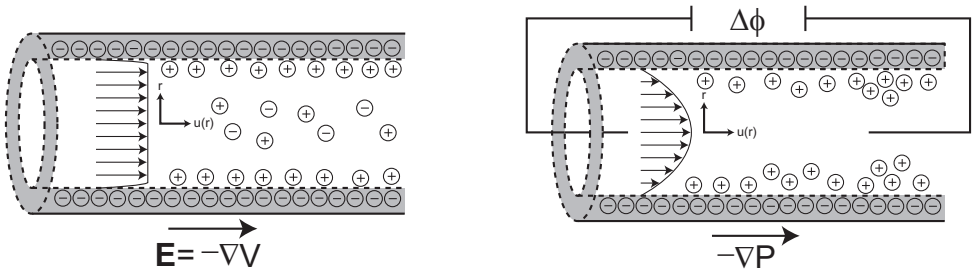

(a) (b)

Figure 2.2: (a) Schematic of uniform electroosmotic flow resulting from an applied electric field. (b) Schematic of the redistribution of ions in pressure driven flow in a microchannel, resulting in a streaming potential. Ion sizes and distributions in the schematics are not to scale.

2.3.3 Electrokinetic Phenomena at Solid–Liquid Interfaces in Microfluidic Devices

Electroosmosis

When an external electric field is applied to a fluid in a microchannel with an ion distribution described by Equation 2.3, flow results. This phenomenon is termed electroosmosis. If the channel is straight and homogeneous with a uniform surface charge density, and its dimensions are large as compared to the Debye length, the flow profile is essentially uniform (Figure 2.2a), and the bulk value of the fluid velocity is given by the Smoluchowski Equation, which stems from the assumptions that fluid properties are uniform and the no-slip boundary condition applies precisely at the "wall," at which $\psi = \zeta$.

$$\boldsymbol{u}_{EO} = -\frac{\epsilon\zeta}{\eta}\boldsymbol{E}\,, \tag{2.6}$$

where ζ is the electrokinetic potential, η is the fluid viscosity, and $\boldsymbol{E}$ is the applied electric field. In the Smoluchowski limit, then, the electroosmotic mobility, μ_{EO}, is

given by

$$\mu_{EO} = -\frac{\epsilon\zeta}{\eta} \,. \tag{2.7}$$

The ζ potential is often inferred from measurements of μ_{EO} [7, 10, 16–20], but the precise meaning of ζ in relation to the electrical potential at the surface is in dispute [8, 21]. Here we phenomenologically define ζ from Equation 2.7, and in simple models assume that ζ is equal to the difference in electrical potential between the bulk solution and the fluid–solid interface. Electroosmosis is commonly used to actuate flow in microfluidic channels, since it can dominate over pressure driven flow at small length scales.

Streaming Current and Streaming Potential

Pressure driven flow in a microchannel results in the bulk motion of charges. When there is charge separation at the fluid–solid interface, this results in the net motion of unbalanced charge in the fluid, and therefore a net electrical current. In flow driven by a uniform pressure gradient, $\frac{\Delta P}{L}$, in a channel with circular cross-section and in the Debye-Hückel approximation ($e\zeta << k_B T$), the electrical current, called streaming current, is

$$I_{\text{stream}} = \frac{\epsilon\zeta}{\eta}\frac{\Delta P}{L}A \,, \tag{2.8}$$

where A is the cross-sectional area of the channel and $\Delta P = P_{\text{downstream}} - P_{\text{upstream}}$. While the streaming current given by Equation 2.8 specifically applies to channels with circular cross-section, it is still a good approximation for other geometries in the limit where the double layers are thin compared to the channel height or radius and the flow is fully developed [10]. Similarly, if flow is driven by pressure but the current path is not closed (Figure 2.2b), an electrical potential, $\Delta\phi$, called streaming potential, results.

$$\Delta\phi = \frac{\epsilon\zeta}{\eta\sigma}\Delta P \,, \tag{2.9}$$

Here σ is the conductivity of the fluid. Equation 2.9 also uses the Debye–Hückel approximation, and assumes the thin EDL limit so that channel geometry effects are unimportant. The conductivity is also assumed to be uniform throughout the channel, though in small channels the non-uniform ion distribution and surface conduction may have significant effects [22]. Streaming potential is often used as an alternative method for measuring the ζ potential [3, 23–25].

2.4 Materials and Methods

Chemical reagents and solutions. All reagents were obtained from Sigma–Aldrich (St. Louis, MO) unless specified otherwise. Phosphate buffers were prepared from stock solutions of monobasic and dibasic potassium phosphate. Acetate buffers were prepared from sodium acetate and glacial acetic acid; Solution conductivity and pH were measured with a dual pH/conductivity meter (Mettler Toledo SevenMulti, Columbus, OH) with specialized electrodes (Mettler Toledo Inlab 730 and Inlab 413, Columbus, OH). Solution pH was adjusted by titration with sodium hydroxide and hydrochloric acid. Fluid viscosity was measured by monitoring the pressure drop of known laminar flow rates through microchannels of known fluidic resistance.

Polymer capillaries. PTFE capillaries were acquired from Scientific Commodities (Lake Havasu City, AZ). Zeonor and TOPAS capillaries were acquired from Paradigm optics (Vancouver, WA). PTFE, TOPAS, and Zeonor 1020R capillaries were used with inner/outer diamters of 330/762, 25/360, and 125/250 microns respectively. Capillaries were equilibrated with solution for 8 hours before testing.

Zeta potential measurement. Phase-sensitive streaming potential and automated current monitoring were used to measure the zeta potential in polymer microchannels. All experiments were run at room temperature (T$= 25^{\circ}$ C). For streaming potential, pressure (0–0.35 MPa) was applied to the inlet of the capillary using a push/pull syringe pump. Sinusoidal pressure waveforms were established via syringe actuation combined with a PID controller corrected for the pressure dependence of the system's pressure–displacement response. Control signals were implemented in LabView. Fluidic connections to the capillary, electrodes, and pressure transducer were made using 360 m stainless steel tubing and PEEK–ULTEM fittings (LabView, Livermore, CA) [26]. Platinized platinum electrodes connected to a 10 GΩ electrometer (6514 Electrometer, Kiethley, Cleveland, OH) measured the generated voltage across the channel and a strain gauge type transducer (Senso–Metrics SP70D, Simi Valley, CA) measured the pressure at the inlet. The forcing pressure and capillary diameters were chosen such that the flow was laminar (Reynolds number below 1200), surface conductivity was negligible, and errors due to hydrodynamic starting lengths could be ignored. The zeta potential was calculated using the Smoluchowski equation (Equation 2.9). Errors introduced by the wall curvature and the use of Equation 2.9 to describe non-Debye–Hückel charge distributions are ignored here since they are small as compared to temperature and conductivity uncertainties. Experiments were repeated a minimum of 20 times for each datum, and results are presented as the mean where error bars indicate the standard deviation.

For current monitoring [16, 27], 150–300V was applied across four 8 cm capillaries using an 8-channel high voltage sequencer (LabView HVS448, Livermore, CA) and platinum electrodes. Control signals were implemented in LabView. Current was monitored on the four remaining channels, after extensively calibrating the device with known resistors. The reservoirs at each end used solutions with conductivities that varied by 5–7.5%. Square-wave voltage sequences were applied with period designed to allow

electroosmosis to completely displace the fluid in the capillary during each half cycle. The resulting current waveforms were fit to a trapezoidal profile and the shape was converted into a velocity measure. Joule heating and the attendant overprediction of electroosmotic mobility was eliminated by measuring the electroosmotic mobility as a function of applied field, and extrapolating to the zero-field limit. Only those electric fields that lead to electrophoretic mobilities within 5% of the low-field limit were used. Pressure imbalances along the system were monitored during 8-hour test series and removed in postprocessing. The zeta potential was calculated using the Smoluchowski equation (Equation 2.6). Errors introduced by the wall curvature are ignored here also since they are small as compared to temperature and conductivity uncertainties.

2.5 The Origins of Charge at Water–Hydrophobe Interfaces

In §2.3, we provided a summary of standard equations and phenomena interpreted entirely from the standpoint of surfaces with well-understood surface charge formation mechanisms and no-slip boundary conditions, combined with assumptions that liquid properties such as viscosity and permittivity are uniform throughout and unaffected by (a) ion populations, (b) electric fields, and (c) short-range inter-molecular potentials associated with the surface. With these assumptions, the (i) governing equations (i.e., Poisson–Boltzmann equation), (ii) constitutive relations (i.e., constant permittivity and viscosity), and (iii) boundary conditions are all reasonably well-defined. While these assumptions are mostly valid for hydrophilic surfaces, many of them are questionable or inncorrect for hydrophobic substrates.

At water–hydrophobe interfaces, the origin of charge is not well-understood (electrostatic and chemical boundary conditions are not well-defined), there may be slip (the

fluid velocity boundary conditions are not well-defined), and interfacial water structuring can lead to significant deviations from mean field approximations (the governing equations and constitutive relations are not well-defined). Thus theoretical modeling and design of hydrophobic microfluidic devices is quite challenging, making careful experimentation with controlled input parameters crucial in this field. In the following and in the companion to this paper [2], we summarize and comment on the current state of experiments and modeling in this field, and provide recommendations for future studies.

The origins of surface charge in common hydrophobic microfluidic substrates are both (a) in dispute and (b) difficult to measure. Most hydrophobic materials are considered chemically inert, and are not expected to have reactive charge-forming surface groups or a strong affinity for ions. Nevertheless, several different hydrophobic materials, including poly(dimethylsiloxane) (PDMS), polystyrene (PS), polyethylene (PE), Zeonor®, and poly(tetrafluoroethylene) PTFE have been shown to have significant surface charge [7]. The hypotheses regarding the source(s) for charge include: (i) surface impurities are present owing to the manufacturing process; these undergo charge-forming chemical reactions when in contact with water; (ii) salt anions are specifically adsorbed, owing to differences in affinity or hydration energy; and (iii) hydroxyl ions are specifically adsorbed, owing to water orientation at a hydrophobic interface. These mechanisms and their relation to observed data are discussed in greater detail below.

2.5.1 Impurities

A common postulate for the origin of charge at polymer–water interfaces is that residual plasticisers, crosslinkers, and initiators from the manufacturing/polymerization process become functional surface groups capable of charge-forming chemical reactions, such

as acid–base dissociation [18, 20, 28]. The prevalence of trade secrets in the polymer industry often leads to uncertainty as to the makeup and concentration of these impurities. We assess the possible role of impurities in interfacial charge for several common microfluidic materials in the following paragraphs.

PDMS is one of the most commonly used microfluidic substrates, owing to its relatively low cost, ease of fabrication, permeability, and elastomeric properties [4,5]. It has been shown that both native and oxidized PDMS exhibit electroosmotic flow, though the electroosmotic mobility of plasma-oxidized PDMS is larger and similar to that of glass [5, 20]. In [20], Ocvirk et. al found that μ_{EO} for native PDMS has a pH dependence very similar to that of fused silica capillaries, and that μ_{EO} did not change with the introduction of different electrolytes, unless high concentrations of large organic surfactants such as sodium dodecyl sulfate (SDS) were used. As a result, they concluded that "silica fillers" introduced by the manufacturer are the origin of charge in native PDMS. Ren et. al [28] also cited silica fillers as the putative origin of charge. However, their attenuated total reflection infrared (ATR–IR) spectroscopy experiments showed that oxygen plasma treated PDMS has large O-H stretches (which suggests the existence of silanol groups on the surface), while native PDMS does not; the absence of silanol spectroscopic features on native PDMS seems inconsistent with the hypothesis that silica filler impurities account for the surface charge. More recently, Wheeler et. al [29] also found that μ_{EO} in PDMS does not depend on the relative amount of curing agent used, indicating that impurities, if important, seem insensitive to concentration.

PTFE is less common as a microfluidic substrate, but is often used as a spun coating (usually in the form of Teflon AF) to modify microfluidic channel surfaces to control contact angle or biocompatibility, especially in electrowetting-on-dieletric devices [30–33]. Data for μ_{EO} as a function of pH in PTFE (Figure 2.3) shows very good

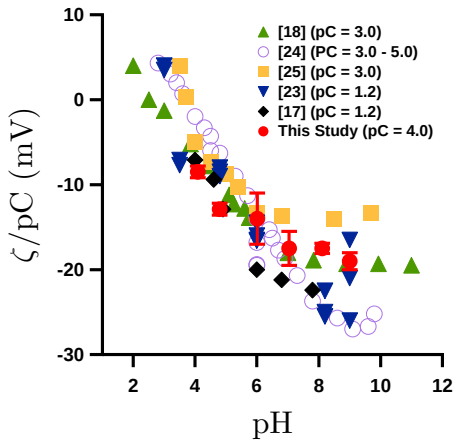

Figure 2.3: ζ normalized by pC ($= -\log C$, C is the counterion concentration in M) as a function of pH for PTFE. Modified from [7] with addition of recent current monitoring data from the authors.

agreement among different sources for pH values between 2 and 7, although there is a significant amount of scatter at high (> 7) pH [7, 17, 18, 23–25]. In Figure 2.3, ζ is normalized by $pC = -logC$, where C is the total counterion concentration in moles/liter. This representation stems from the engineering approximation $\zeta = a \log C$, proposed in [10] as a way to simplify representation of ζ-potential data for microfluidic substrates measured by multiple investigators. In order for impurities to be the origin of charge across the entire practical pH range, this agreement between data taken with different suppliers of PTFE manufactured with radically different methods, and with several different methods for measuring μ_{EO}, can only be explained if synthesis of PTFE produces similar impurities in all cases.

Olefins such as polystyrene (PS), polyethylene (PE), and poly (vinyl chloride) (PVC) were explored as substrates for microfluidics applications and analytical separations in the 1990s and the beginning of the 21st century [18, 19, 34–36]. More recently, cyclic olefin copolymers (COCs) such as Zeonor®, Zeonex®, and TOPAS®resins, have started to dominate use of olefins in microfluidics applications—owing to their good optical properties, high chemical resistance, and low water absorbance. Earlier work [18]

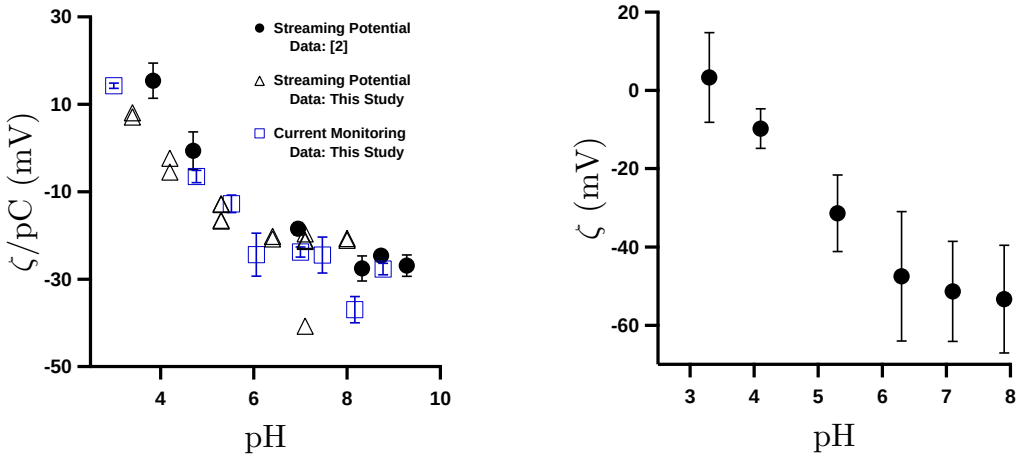

(a) (b)

Figure 2.4: (a) ζ normalized by pC$= -\log C$ (C is the counterion concentration in M) as a function of pH for Zeonor®. (b) Streaming potential data showning ζ as a function of pH for Topas®(pC = 3)

on polymer capillaries (PTFE, PE, PVC) observed sigmoidal pH dependence consistent with charged sites with pKa near 4.5, and postulated that carboxylic acids from impurities were responsible for the surface charge density. Mela et. al [3] have shown that μ_{EO} for Zeonor®resins exhibits sigmoidal pH dependence consistent with charged sites with $pK_a = 4.8$; here we report results with both current monitoring and streaming potential experiments that are consistent with those earlier results, despite using different laboratories, experimenters, fluidic platforms, and measurement techniques (Figure 2.4a). Our streaming potential measurements of ζ as a function of pH in Topas®(Figure 2.4b) showed very similar results, but simultaneously raise questions. Since the cyclopentadiene structure that dominates Zeonor does not have any ionizable sites, one possible explanation for this behavior is the existence of carboxylic acid groups, which would arise from either oxidation of the cyclopentadiene structure or from the presence of proprietary plasticizers. However, Mela et. al showed both via XPS and via chemical functionalization that no significant amount of carboxylic acid surface moieties exist. At present, it seems unlikely that surface functional groups that have eluded detection

via fluorescent and XPS techniques could be solely responsible for the electrokinetic behavior observed for these materials in contact with aqueous solutions.

While impurities certainly may affect the electrokinetic performance of some hydrophobic materials used in microsystems, impurities cannot explain the majority of the observed data. Many hydrophobic materials show consistent electrokinetic properties independent of the manufacturing process [7]. In fact, there is little, if any, support for the postulate that impurities are a primary source of charge in any polymeric microfluidic system. Relatively few experiments have been conducted to detect the role of impurities (a short summary of some is shown in Table 2.1), with minimal results.

2.5.2 Specific adsorption of (salt) ions

Specific adsorption of ions is known to affect many surfaces; for example, divalent cations, if present at high concentrations, have been shown to change the sign of the electrokinetic potential on glass surfaces at high pH [37]. While specific adsorption is often a minor issue for highly-charged hydrophilic surfaces, the effect of adsorption of free ions from solution may become more important and easier to measure when the surface has few, if any, charged groups. In buffered electrolyte solutions, salt ions can lead to a net surface charge density if some ions are preferentially adsorbed over others owing to differences in their affinity or hydration energy [38, 39]. While adsorption is of course critical for large surfactant molecules, amphipathic surfactants are beyond the scope of the current work, and we focus here on small salt ions. In order for a hydrated ion to be able to adsorb to a surface, water molecules must be removed, so less-hydrated ions tend to preferentially adsorb as compared to more-hydrated ions. A summary of experiments testing for interfacial electrolyte anion adsorption is shown in Table 2.2.

Table 2.1: Summary of experiments with discussion of impurities

	Interface	**Electrolytes used**	**Concentration ranges studied**	**Results**
Schutzner [18]: μ_{EO} measurements	Water in PVC, PS, and PTFE microchannels	Betaine	$10\ mM$	All materials had similar sigmoidal ζ vs. pH curves, with $pK_a = 4.8$. Surface carboxylate groups are postulated as the origin of charge, since the pK_a is similar to the value for aliphatic carboxylic acids.
Ocvirk [20]: Current monitoring	Water in oxidized and native PDMS microchannels	KCl, phosphate	$11\ mM$	ζ potentials are larger in magnitude for oxidized compared to native PDMS. The ζ vs. pH behavior for oxidized PDMS is similar to that for glass.
Ren [28]: Current monitoring, ATR–IR	Water in oxidized and native PDMS microchannels	Phosphate	10 and $20\ mM$	ATR–IR shows that surface $-OH$ groups in oxidized PDMS disappear over time with exposure to air. $\mu_{EP}$for native PDMS is stable over time. $\mu_{EP}$for oxidized PDMS is stable when the PDMS is stored in buffer, but unstable when it is exposed to air.
Mela [3]: Amine-functionalized dyes	Water in Zeonor® microchannels	Phosphate, Acetate, Tris, Borate	$10\ mM$	Zeonor®surfaces incubated with amine-functionalized dyes showed no fluorescence, indicating that they did not have significant surface concentration of carboxylic acid groups.

A number of spectroscopic and molecular dynamics (MD) studies have provided direct evidence for the adsorption of electrolyte ions at liquid–gas interfaces [40–43], which serve as model hydrophobic interfaces owing to the well-defined geometry and the absence of hydrogen bonding in the gas phase. Sum frequency generation (SFG) measurements of air–water systems indicate enhanced anion concentration at the interface at high (> 0.1 M) salt concentrations [40,41,44,45]. Recent XPS experiments per-

formed at water-vapor interfaces with very high (saturated) salt concentrations demonstrated similar behavior [43]. Second harmonic generation (SHG) data for these interfaces across a range of salt concentrations (1mM – 1M) show that ion adsorption follows Langmuir adsorption kinetics [42]. This attraction of ions to vapor–liquid interfaces has been used to explain anomalous electrokinetic effects seen in molecular dynamics simulations of hydrophobic nanochannels, where both the existence of a region of depleted water density and specific ion concentration were seen [46].

While spectroscopic data provides clear evidence for salt ion adsorption at vapor–liquid interfaces in solutions with high salt concentration, data from electrokinetics experiments involving hydrophobic surfaces and lower salt concentrations (0.1 – 1 mM) does not conclusively support salt ion adsorption [3, 7, 47]. Measurements of electrophoretic mobility as a function of the counterion concentration have been shown to be explained by Gouy–Chapman-type double layer shielding effects and are in general independent of the particular buffer ions used for a variety of hydrophobic microfluidic substrates [3,7]. The electrophoretic mobility of oil droplets was also found to be buffer-independent, and scaled in a manner consistent with double layer shielding [47]. The discrepancy between the spectroscopic measurements taken at high salt concentrations and the electrokinetic measurements taken at low concentrations suggests there may be certain regimes of experimental parameters where salt ion adsorption becomes more or less important; certainly effects seen at high concentrations of large anions such as Br^- and I^- may not be significant at low concentrations of smaller ions such as Na^+ or Cl^-. At low salt concentrations, poor signal-to-noise ratio could hinder SFG/SHG experiments, which could explain the lack of spectroscopic evidence for salt adsorption in the < 1 mM regime. However, the data in [42], which covers a concentration range which is between those studied in microfluidics and other spectroscopic measurements (1 mM – 1 M), shows that the degree of interfacial salt adsorption decreases rapidly as

Table 2.2: Summary of anion adsorption results

	Interface	**Electrolytes used**	**Concentration ranges studied**	**Salt ion adsorption behavior**
Franks [47]: μ_{EP} measurements	Hexadecane droplets in water	NaCl, NaBr, NaI, NaF, $NaClO_4$,$NaIO_3$, LiCl,CsCl	0.1 – $11\ mM$	No interfacial enhancement of salt anions; mobility changes with salt concentration are consistent with double layer shielding effects, independent of the ion type
Mela [3]: Streaming potential	Water in Zeonor® microchannels	Phosphate, Acetate, Tris, Borate	$10\ mM$	ζ-potential data taken with different electrolytes fit on the same sigmoidal curve
Petersen [42]: SHG	Air–water	NaN_3	10^{-3} – $1M$	Enhanced N_3^- concentration at the interface, following Langmuir kinetics
Huang [46]: MD simulations	Solid–water: contact angle $= 140°$ and $50°$	NaI, NaCl	$0.2M$ and $1M$	Interfacial enhancement of large ions, i.e. I^-
Liu [40]: SFG, Raman, ATR–FTIR	Air–water	NaCl, NaBr, NaI, NaF	$0.820M$, $2.07M$	Enhanced Br^- and I^- concentrations at the interface
Vrbka [41]: MD simulations	Air–water	NaCl, NaBr, NaI, NaF	$1.2M$	Enhanced Br^- and I^- concentrations at the interface
Ghosal [43]: XPS	Vapor–liquid	KBr, KI	saturated	Enhanced Br^- and I^- concentrations at the interface, more so for I^-

the salt concentration is decreased. This suggests that at low concentrations, salt anion adsorption is also physically less important, and may be very difficult to observe in the presence of other chemical processes (e.g., surface reactions or hydroxyl adsorption).

2.5.3 Specific adsorption of hydroxyl ions

The specific adsorption of hydroxyl ions onto hydrophobic interfaces has also been proposed as an origin of surface charge in microfluidic substrates [48, 49]. Even though hydroxyl ions tend to be more hydrated as compared to hydronium or salt ions [39], they are believed to preferentially adsorb onto aqueous-hydrophobic interfaces resulting in a net negative surface charge density [50]. This putative mechanism is analogous to the preferential adsorption of iodide at AgI crystal surfaces (Equation 2.2), which leads to a pzc at pAg=5.5 for AgI solutions at room temperature (see e.g. [51]). Molecular dynamics simulations have shown that structuring of water at the interface may facilitate this process [52, 53], which can be energetically favorable if hydroxyl ions hydrogen bond with ordered water molecules. This interfacial charging mechanism is consistent with experimental data for most hydrophobic surfaces, which have pH-dependent electrokinetic potentials that become increasingly negative with increasing pH [7]. However, simple models based solely on hydroxyl ion adsorption fail to explain positive charges on hydrophobic substrates [3], differences between different hydrophobic materials [18], and materials that have erratic behavior as a function of experimental parameters [7].

Interfacial charging by hydroxyl ion adsorption has been used to explain the electrokinetic behavior of oil droplets [47,50,54–56] and hydrophobic colloids [57] in aqueous electrolyte solutions (Table 2.3). Marinova et. al [50] studied the electrokinetic properties of oil droplets as a function of oil type, pH, and electrolyte concentration. They showed that xylene, dodecane, hexadecane, and perfluoromethyldecalin droplets all had nearly the same electrophoretic mobility, and that the electrolyte concentration dependence could be explained by compression of the double layer without specific salt ion adsorption. The pH dependence of μ_{EP} along with a hydroxyl ion adsorption model

based on Stern isotherms gave a specific adsorption energy of 25 kT per ion. Later studies demonstrated similar behavior [55, 56], including some that specifically examined salt concentration dependence at relatively low salt concentrations(in the 0.1 – 11 mM concentration range) [47]. In an experiment with solid colloids, Ametov et. al [57] found a significant decrease in the ζ potential when they increased the hydrophobicity of silica colloids by methylation. Though the magnitude of the ζ potential was reduced, colloids with contact angle $\sim 90^{\circ}$ still showed pH-dependence that can be modeled by hydroxyl ion adsorption.

Some researchers studying solid–liquid interfaces in microfluidic systems have also postulated hydroxyl ion adsorption as the origin of charge [24, 48, 58]. Streaming potential measurements on plasma deposited fluorpolymer (PDFP) systems demonstrated significant changes in the ζ potential with the addition of KOH or NaCl [24]. Werner et. al postulated that the changes were due to preferential adsorption of $\mathrm{H_3O^+}$ and $\mathrm{OH^-}$ ions, owing to the fact that PDFP has no ionizable surface groups. Zimmermann et. al [48] observed similar behavior with Teflon AF, and additionally postulated that preferential adsorption of $\mathrm{H_3O^+}$ and $\mathrm{OH^-}$ ions is facilitated by hydrogen bonding with ordered water structures [50], a mechanism which has since gained support from molecular dynamics simulations [52, 53, 59]. The idea of stabilizing ordered water structures is also experimentally supported by SFG spectra of liquid vapor interfaces, which show characteristic peaks corresponding to dangling surface hydroxyl bonds and ice-like hydrogen-bonded hydroxyl groups. [45]. The structure of water at hydrophobic interfaces is of critical importance, and is discussed in greater detail in the companion to this paper [2].

Table 2.3: Summary of oil droplet/colloidal experiments in the context of hydroxyl ion adsorption

	Interface	**Electrolytes used**	**Concentration ranges studied**	**Results**
Dickinson [54]: μ_{EP} measurements	Octadecane and paraffin droplets in water	NaCl, phosphate, borate	$0.01\ N$	All μ_{EP}vs. pH curves were similar, where μ_{EP}increases with increasing pH
Marinova [50]: μ_{EP} measurements	Xylene, dodecane, hexadecane and perfluoromethyldecalin droplets in water	NaCl, Na_2CO_3 urea	0.01 – $10\ mM$	The ζ potential does not depend on the oil type, is increasingly negative with increasing pH, and is unaffected by addition of Na_2CO_3 up to $1\ mM$. Dependence on NaCl concentration is consistent with double layer compression
Ho [55]: Dynamic light scattering	Palm olein droplets in water	NaCl, $MgCl_2$, $CaCl_2$	$1.5\ mM$, $0.15\ mM$	The ζ potential is is increasingly negative with increasing pH. Differences between monovalent and divalent ions are consistent with double layer shielding effects.
Graciaa [56]: Spinning tube zetameter	n-alkane droplets in water (6 to 14 carbon atoms)	NaCl	10^{-4} – $10\ mM$	Alkane length has little effect on ζ-potential. Results agree with [50]
Ametov [57]: Phase analysis light scattering	Methylated silica colloids in water	KNO_3	$1\ mM$	ζ potential is reduced for methylated silica spheres. The general shape of the ζ vs. pH curves is unaffected by methylation.

2.6 Conclusions and Recommendations

Identifying the origins of charge on hydrophobic surfaces is inherently challenging, owing to the added complexities of slip phenomena, uncertainties in interfacial structures, and unknown surface chemistry. While much of the microdevice and electrophoresis literature refers anecdotally to impurities as a source of charge, there are very few methodical studies of impurities in hydrophobic microfluidic substrates. At present, appreciable

electrokinetic potentials can be observed on a variety of hydrophobic surfaces [7,49], in a manner unexplained by postulated impurities and inconsistent with the lack of charged groups in the native material. The most direct studies of salt adsorption [47] indicate that salt ions are not appreciably adsorbed in a concentration range for which significant electrokinetic potentials are observed, thus making salt adsorption unsatisfactory for explaining many of the observed phenomena. Hydroxyl ion adsorption appears to be the most satisfactory explanation for the surface charge; however, this mechanism still lacks the comprehensive experimental and numerical validation required for general adoption. Beattie [49], for example, proposes hydroxyl ion adsorption as the source of charge on hydrophobic substrates owing to roughly consistent isolectric points (pIs) observed on several materials combined with other supporting data. While many hydrophobic polymers do have similar pIs, the differences between these pIs are significant as compared to experimental uncertainty, and these differences are not fully explained by OH^- adsorption. Further, many materials for which OH^- adsorption is not presumed to play a significant role (e.g., PC, PMMA, Silica) have pIs within the same range. At this point, the universality of OH^- adsorption as the source of charge on hydrophobic surfaces is promising, but yet to be demonstrated.

Experimentation in this area is challenging, owing to the large number of input parameters involved (e.g. pH, temperature, electrolyte ions, etc.), fluctuations in data due to transient or unstable chemical processes, and the coupling of slip with electrokinetic phenomena. Molecular dynamics simulations in this area are also challenging, owing to the complex nature of potentials for water and the inability of individual models to reproduce a wide variety of test parameters [60]. Further, the charge density expected on these surfaces is only moderate, and thus the spatial extent of the system required to achieve usable statistics requires an extensive calculation.

Future studies on the origin of charge in hydrophobic microfluidic devices should be focused on (i) bridging thermodynamic models with experimental data, and (ii) attempting to isolate the effects of each of the charge forming mechanisms independently through carefully designed experiments. Examination of the temperature dependence of these systems can lead to progress with the former, as chemical equilibria and ion distributions are both temperature-dependent. For the latter, there are several experiments which would lead to progress in this field, e.g.: (a) a methodical study of the effects of impurities, where impurities are implanted into a hydrophobic microfluidic substrate, and (b) electrokinetic characterization of hydrophobic substrates using solutions of high (> 0.1 M) salt concentration.

BIBLIOGRAPHY

[1] V. Tandon, S.K. Bhagavatula, W.C. Nelson, and B.J. Kirby. Zeta potential and electroosmotic mobility in devices fabricated from hydrophobic polymers: 1. the origins of charge. *Electrophoresis*, 29:1092–1101, 2008.

[2] V. Tandon and B.J. Kirby. Zeta potential and electroosmotic mobility in devices fabricated from hydrophobic polymers: 2. slip and interfacial water structure. *Electrophoresis*, 29:1102–1114, 2008.

[3] P. Mela, A. van den Berg, Y. Fintschenko, E.B. Cummings, B.A. Simmons, and B.J. Kirby. The zeta potential of cyclo-olefin polymer microchannels and its effects on insulative (electrodeless) dielectrophoresis particle trapping devices. *Electrophoresis*, 26:1792–1799, 2005.

[4] H.A. Stone, A.D. Stroock, and A. Ajdari. Engineering flows in small devices: Microfluidics toward a lab-on-a-chip. *Annual Review of Fluid Mechanics*, 36:381–411, 2004.

[5] J.C. McDonald, D.C. Duffy, J.R. Anderson, D.T. Chiu, H. Wu, O.J.A. Schueller, and G.M. Whitesides. Fabrication of microfluidic systems in poly(dimethylsiloxane). *Electrophoresis*, 21:27–40, 2000.

[6] B.G. Hawkins, A.E. Smith, Y.A. Syed, and B.J. Kirby. Continuous-flow particle separation by 3d insulative dielectrophoresis using coherently shaped, dc-biased, ac electric fields. *Analytical Chemistry*, page Accepted, 2007.

[7] B.J. Kirby and E.F. Jr. Hasselbrink. Zeta potential of microfluidic substrates: 2. data for polymers. *Electrophoresis*, 25:203–213, 2004.

[8] R.J. Hunter. *Zeta Potential in Colloid Science*. Academic Press, London, 1981.

[9] R.K. Iler. *The Chemistry of Silica*. Wiley, New York, 1979.

[10] B.J. Kirby and E.F. Jr. Hasselbrink. Zeta potential of microfluidic substrates: 1. theory, experimental techniques, and effects on separations. *Electrophoresis*, 25:203–213, 2004.

[11] R.J. Hunter. *Foundations of Colloid Science, Vol. 2*. Clarendon Press, Oxford, 1989.

[12] P. Attard. Asymptotic analysis of primitive model electrolytes and the electrical double layer. *Physical Review E*, 48(5):3604–3621, 1993.

[13] P. Attard. Electrolytes and the electric double layer. *Advances in Chemical Physics*, 92:1–159, 1996.

[14] W.R. Fawcett and D.J. Henderson. A simple model for the diffuse double layer based on a generalized mean spherical approximation. *Journal of Physical Chemistry B*, 104:6837–6842, 2000.

[15] D. Boda, D. Henderson, P. Plaschko, and W.R. Fawcett. Monte carlo and density functional theory study of the electrical double layer: The dependence of the charge/voltage relation on the diameter of the ions. *Molecular Simulation*, 30:137–140, 2004.

[16] X. Huang, M.J. Gordon, and R.N. Zare. Current-monitoring method for measuring the electroosmotic flow rate in capillary zone electrophoresis. *Analytical Chemistry*, 60:1837–1838, 1988.

[17] K.D. Lukacs and J.W. Jorgenson. Capillary zone electrophoresis: Effect of physical parameters on separation efficiency and quantitation. *Journal of High Resolution Chromatography*, 8(8):407–411, 1985.

[18] W. Schutzner and E. Kenndler. Electrophoresis in synthetic organic polymer capillaries: Variation of the electroosmotic velocity and zeta potential with ph and solvent composition. *Analytical Chemistry*, 64:1991–1995, 1992.

[19] L.E. Locascio, C.E. Perso, and C.S. Lee. Measurement of electroosmotic flow in plastic imprinted microfluid devices and the effect of protein adsorption on flow rate. *Journal of Chromatography A*, 857(1):275–284, 1999.

[20] G. Ocvirk, M. Munroe, T. Tang, R. Oleschuk, K. Westra, and D.J. Harrison. Electrokinetic control of fluid flow in native poly(dimethylsiloxane) capillary electrophoresis devices. *Electrophoresis*, 21:107–115, 2000.

[21] J. Lyklema. *Fundamentals of Interface and Colloid Science, Volume II: Solid-Liquid Interfaces*. Academic Press, London, 1995.

[22] J. Lyklema and M. Minor. On surface conduction and its role in electrokinetics. *Colloids and Surfaces A*, 140:33–40, 1998.

[23] J.C. Reijenga, G.V.A. Aben, T.P.E.M. Verheggen, and F.M. Everaerts. Capillary

zone electrophoresis: Effect of physical parameters on separation efficiency and quantitation. *Journal of High Resolution Chromatography*, 8:407–411, 1983.

[24] C. Werner, H. Korber, R. Zimmermann, S. Dukhin, and H. Jacobasch. Extended electrokinetic characterization of flat solid surfaces. *Journal of Colloid and Interface Science*, 208(1):329–346, 1998.

[25] U. Lappan, H.-M. Buchhammer, and K. Lunkwitz. Surface modification of poly(tetrafluoroethylene) by plasma pretreatment and adsorption of polyelectrolytes. *Polymer*, 40(14):4087–4091, 1999.

[26] B.J. Kirby, D.S. Reichmuth, R.F. Renzi, T.J. Shepodd, and B.J. Wiedenman. Microfluidic routing of aqueous and organic flows at high pressurs: fabrication and characterization of integrated polymer microvalve elements. *Lab on a Chip*, 5:184–190, 2005.

[27] D. Ross and L.E. Locascio. Effect of caged fluorescent dye on the electroosmotic mobility in microchannels. *Analytical Chemistry*, 75(5):1218–1220, 2003.

[28] X. Ren, M. Bachman, C. Sims, G.P. Li, and N. Allbritton. Electroosmotic properties of microfluidic channels composed of poly(dimethylsiloxane). *Journal of Chromatography B*, 762:117–125, 2001.

[29] A.R. Wheeler, G. Trapp, O. Trapp, and R.N. Zare. Electroosmotic flow in a poly(dimethylsiloxane) channel does not depend on percent curing agent. *Electrophoresis*, 25:1120–1124, 2004.

[30] H. Moon, S.K. Cho, R.L. Garrell, and C.-J. Kim. Low voltage electrowetting-on-dielectric. *Journal of Applied Physics*, 92(7):4080–4087, 2002.

[31] J. Lee, H. Moon, J. Fowler, T. Schoellhammer, and C.-J. Kim. Electrowetting and electrowetting-on-dielectric for microscale liquid handling. *Sensors and Actuators A*, 95:259–268, 2002.

[32] T.B. Jones, J.D. Fowler, Y.S. Chang, and C.-J. Kim. Frequency-based relationship of electrowetting and dielectrophoretic liquid microactuation. *Langmuir*, 19:7646–7651, 2003.

[33] S.K. Cho, H. Moon, and C-.J. Kim. Creating, transporting, cutting and merging liquid droplets by electrowetting-based actuation for digital microfluidic circuits. *Journal of Microelectromechanical Systems*, 12(1):70–80, 2003.

[34] A. Voight, H. Wolf, H. Lauckner, G. Neumann, R. Becker, and L. Richter. Electrokinetic properties of polymer and glass surfaces in aqueous solutions: Experimental evidence for swollen surface layers. *Biomaterials*, 4:299–304, 1983.

[35] M.A. Roberts, J.S. Rossier, P. Bercier, and H. Girault. Uv laser machined polymer substrates for the development of microdiagnostic systems. *Analytical Chemistry*, 69:2035–2042, 1997.

[36] T.J. Johnson, R. Ross, and L.E. Locascio. Rapid microfluidic mixing. *Analytical Chemistry*, 74(1):45–51, 2002.

[37] A.M. Gaudin and D.W. Fursteneau. *Trans. ASME*, 202:66–72, 1955.

[38] J. Lyklema. *Fundamentals of Interface and Colloid Science, Volume I: Fundamentals*. Academic Press, London, 1991.

[39] J.N. Israelachvili. *Intermolecular and Surface Forces*. Academic Press, London, 1992.

[40] D. Liu, G. Ma, L.M. Levering, and H.C. Allen. Vibrational spectroscopy of aqueous sodium halide solutions and air-liquid interface: Observation of increased interfacial depth. *Journal of Physical Chemistry B*, 108:2252–2260, 2004.

[41] L. Vrbka, M. Mucha, B. Minofar, and P. Jungwirth. Propensity of soft ions for the air/water interface. *Current Opinion in Colloid and Interface Science*, 9:67, 2004.

[42] P.B. Petersen and R.J. Saykally. Confirmation of enhanced anion concentration at the liquid water surface. *Chemical Physics Letters*, 397:51–55, 2004.

[43] S. Ghosal, J.C. Hemminger, H. Bluhm, B.S. Mun, E.L.D. Hebenstreit, G. Ketteler, D.F. Ogletree, F.G. Requejo, and M. Salmeron. Electron spectroscopy of aqueous solution interfaces reveals surface enhancement of halides. *Science*, 307:563–566, 2005.

[44] S. Baldelli, C. Schnitzer, M. Schultz, and D.J. Campbell. Sum frequency generation investigation of water at the surface of H_2O/H_2SO_4 and H_2O/Cs_2SO_4 binary systems. *Chemical Physics Letters*, 287:143–147, 1998.

[45] C. Raduge, V. Pflumio, and Y.R. Shen. Surface vibrational spectroscopy of sulfuric acid-water mixtures at the liquid-vapor interface. *Chemical Physics Letters*, 274(1):140–144, 1997.

[46] D.M. Huang, C. Cottin-Bizonne, C. Ybert, and L. Bocquet. Ion-specific anomalous electrokinetic effects in hydrophobic nanochannels. *Physical Review Letters*, 98:177801, 2007.

[47] G.V. Franks, A.M. Djerdjev, and J.K. Beattie. Abscence of specific cation or anion effects at low salt concentrations on the charge at the oil/water interface. *Langmuir*, 21:8670–8674, 2005.

[48] R. Zimmermann, S. Dukhin, and C. Werner. Electrokinetic measurements reveal interfacial charge at polymer films caused by simple electrolyte ions. *Journal of Physical Chemistry B*, 105:8544–8549, 2001.

[49] J.K. Beattie. The intrinsic charge on hydrophobic microfluidic substrates. *Lab on a Chip*, 6:1409–1411, 2006.

[50] K.G. Marinova, R.G. Alargova, N.D. Denkov, O.D. Velev, D.N. Petsev, I.B. Ivanov, and R.P. Borwankar. Charging of oil-water interfaces due to spontaneous adsorption of hydroxyl ions. *Langmuir*, 12:2045–2051, 1996.

[51] I. Larson and P. Attard. Surface charge of silver iodide and several metal oxides. Are all surfaces Nernstian? *Journal of Colloid and Interface Science*, 227:152–163, 2000.

[52] L.X. Dang and T. Chang. Molecular mechanism of ion binding to the liquid/vapor interface of water. *Journal of Physical Chemistry B*, 106:235–238, 2002.

[53] S.I. Mamatkulov, P.K. Khabibullaev, and RR. Netz. Water at hydrophobic substrates: Curvature, pressure, and temperature effects. *Langmuir*, 20:4756–4763, 2004.

[54] W. Dickinson. The effect of ph upon the electrophoretic mobility of emulsions of certain hydrocarbons and aliphatic halides. *Trans. Faraday Soc.*, 37:140, 1941.

[55] C.C. Ho and K. Ahmad. Electrokinetic behavior of palm oil emulsions in dilute electrolyte solutions. *Journal of Colloid and Interface Science*, 216:25–33, 1999.

[56] A. Graciaa, P. Creux, C. Dicharry, and J. Lachaise. Measurement of the zeta potential of oil drops with the spinning tube zetameter. *Journal of Dispersion Science and Technology*, 23:301–307, 2002.

[57] I. Ametov and C.A. Prestidge. Hydrophobic interactions in concentrated col-

loidal suspensions: A rheological investigation. *Journal of Physical Chemistry B*, 108(32):12116–12122, 2004.

[58] R. Schweiss, P. Welzel, W. Knoll, and C. Werner. Assembly modulates dissociation: electrokinetic experiments reveal peculiarities of the charge formation at monolayer films. *Chemical Communications*, 2:256–258, 2005.

[59] R. Zangi and J.B.F.N. Engberts. Physisorption of hydroxide ions from aqueous solution to a hydrophobic surface. *Journal of the American Chemical Society*, 127:2272–2276, 2005.

[60] B. Guillot. A reppraisal of what we have learnt during three decades of computer simulations on water. *Journal of Molecular Liquids*, 101(1):219–260, 2002.

CHAPTER 3

ZETA POTENTIAL AND ELECTROOSMOTIC MOBILITY IN MICROFLUIDIC DEVICES FABRICATED FROM HYDROPHOBIC POLYMERS: 2. SLIP AND INTERFACIAL WATER STRUCTURE

Abbreviations: **EDL**, electrical double layer; **ATR–FTIR**, attenuated total reflection Fourier transform infrared; **SFG**, sum frequency generation; **MD**, molecular dynamics; **SFA** surface force apparatus; **AFM**, atomic force microscopy; **PIV**, particle image velocimetry; **OTS**, octadecyl trichlorosilane

3.1 Abstract

We discuss the structure of water at hydrophobic interfaces from the standpoint of its impact on electrokinetic phenomena in microfluidic devices fabricated from hydrophobic polymers such as Teflon or Zeonor. Water structuring at hydrophobic interfaces has been described as a source of interfacial charge [2], and dewetting phenomena, whether via depletion layers or nanobubbles, contributes to slip and enhanced apparent electrokinetic potentials. Issues concerning the impact of hydrodynamic slip and the role of diffuse interfacial structures are discussed. These issues are coupled with each other and with interfacial charge concerns, providing challenges for measurements of individual parameters.

[0]The content of this chapter was submitted and published as a research article that is reproduced here with permission from *Electrophoresis*. This is the pre-peer reviewed version of the following article:"Zeta Potential and Electroosmotic Mobility in Devices Fabricated from Hydrophobic Polymers: 2. Slip and Interfacial Water Structure" [1].

3.2 Introduction

Water is among the most intriguing of materials. In addition to its ubiquity and engineering relevance, water poses challenges owing to the complexity of its interactions with itself, solutes, and interfaces. These complexities have made it difficult to define molecular models for water that predict all important phenomena.

The presence of a solid interface interferes with the structure of water's hydrogen-bonded lattice. For hydrophilic surfaces, this can lead, for example, to orientation of water dipoles [3] and an attendant reduction in electrical permittivity [4]. For hydrophobic surfaces, the results are not as well understood. The structure of water at hydrophobic interfaces may be a driving factor for interfacial charge, and it is closely related to observed hydrodynamic slip.

When considering the influence of hydrophobic surfaces on electrokinetic phenomena, we focus on those aspects of interfacial structure that affect the fluid mechanical problem, namely the actuation of mobile charge (the key source term in the hydrodynamic equations), and the influence on hydrodynamic slip (the boundary condition for the hydrodynamic equations). Study of electrokinetics in hydrophobic substrates is more complicated than in hydrophilic substrates because (a) modes of charge formation at the fluid–solid interface are less well-understood [2] and (b) the hydrodynamic slip boundary condition is highly coupled with macroscopically observable electrokinetic phenomena, leading to inflated apparent electrokinetic potentials. Modeling slip is non-trivial since the origin of slip is also currently in dispute [5]. Both slip and surface charge have been postulated to depend on the molecular/supramolecular structure of water at the hydrophobic interface; proposed structures include ice-like hydrogen-bonded networks of water molecules [6–8], regions of depleted water density [9], and

nanobubbles [10].

In the companion to this paper [2], we have presented fundamental electrokinetic relations and then discussed different models for the origins of charge on hydrophobic surfaces, most of which have few if any charged surface groups. Here, we discuss slip phenomena and interfacial molecular/supramolecular structures. As was the case in [2], we focus on microfluidic devices with aqueous electrolyte solutions, and exclude discussion of large amphipathic and organic surfactants.

3.3 Electrokinetics

Here we consider electrokinetic phenomena following the notation and discussion presented in [2]. We assume that charge separation phenomena lead to a net charge at the interface between the aqueous solution and the microdevice substrate, and that charge coincides with an interfacial potential (the zeta potential, ζ) as well as a diffuse electrical double layer that can be described with a Gouy–Chapman–Stern model [11]. The electrical potential distribution is given by the Poisson–Boltzmann equation:

$$\nabla^2\psi = -\frac{\rho_e}{\epsilon} = -\frac{1}{\epsilon}\sum_i n_{o,i} e z_i \exp\left(-\frac{e z_i}{k_B T}\psi\right) , \tag{2.3}$$

and nondimensionalization of the Poisson–Boltzman equation leads to the Debye length λ_D:

$$\lambda_D = \sqrt{\frac{\epsilon k_B T}{2e^2(\Gamma/2)}} \tag{2.4}$$

We interpret the effects of interfacial phenomena at hydrophobic surfaces primarily in the context of electroosmosis and streaming potential. Electroosmosis is described in the Smoluchowski limit by the electroosmotic mobility, μ_{EO}, given by

$$\mu_{EO} = -\frac{\epsilon\zeta}{\eta} , \tag{2.7}$$

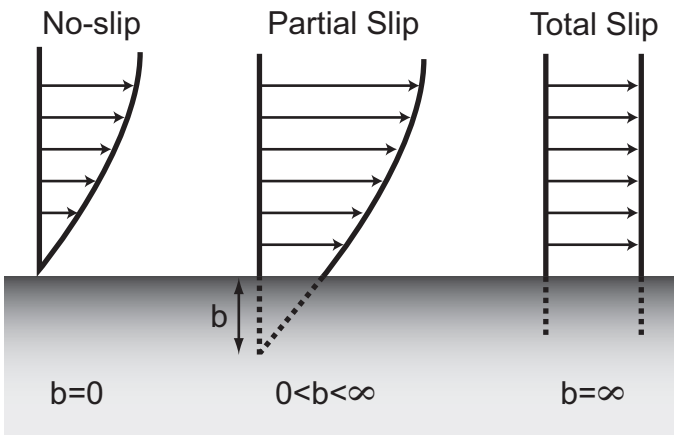

Figure 3.1: Schematic showing an interpretation of the slip length, b.

while streaming potential in the Debye–Huckel, thin double layer, and Smoluchowski limits is given by

$$\Delta\phi = \frac{\epsilon\zeta}{\eta\sigma}\Delta P \, . \tag{2.9}$$

Our focus in this paper is deviation from Smoluchowski-type relations such as Equation 2.9.

3.4 Slip Boundary Condition at Water–Hydrophobe Interfaces

In most physical descriptions of microfluidic systems, no-slip boundary conditions at solid–liquid interfaces are assumed [12,13]. Flows in hydrophobic microfluidic systems, however, have been shown to deviate from those predicted by models using no-slip boundary conditions [5, 14–31]. Here we focus on slip in hydrophobic systems with careful attention to electrokinetically driven flow.

3.4.1 Quantifying slip

Navier [32] and later Maxwell [33] proposed a linear boundary condition which remains as the standard description of slip. In this formalism, the fluid velocity field component tangent to the surface, u_t, is proportional to the shear rate at the surface.

$$u_t = b\,\boldsymbol{n}\cdot\left(\nabla\boldsymbol{u}+\nabla\boldsymbol{u}^T\right)\cdot\left(\mathbf{1}-\boldsymbol{nn}\right)\ , \tag{3.1}$$

where u_t is the slip velocity, $\mathbf{u}$ is the fluid velocity field, b is the slip length parameter, and $\mathbf{n}$ is the unit vector normal to the wall. In a simpler form,

$$u_t = b\left(\frac{\partial u_t}{\partial n}\right)_{wall}\ , \tag{3.2}$$

where the differential length ∂n is in the direction normal to the wall. Here the proportionality constant, b, has the units of length, and is referred to as the slip length. The slip length can be interpreted as representing the distance beyond the wall at which the fluid velocity field becomes zero, if the velocity field is extrapolated linearly (Figure 3.1). Physically, the slip length is analogous to a surface friction coefficient, as it relates a field property (shear rate) to the boundary condition. Typically, experimental measurements of slip are reported as slip lengths.

3.4.2 Measurement of slip in microsystems

Slip lengths can be measured directly or inferred through measurements of the macroscopic properties of a microfluidic system. In order for slip to have a significant and measurable effect on the macroscopic properties of a system, the slip length should approach the same order as the characteristic length scale for the system (roughly the length over which fluid velocity in the bulk solution changes to the value at the wall). There is a great deal of variation in slip length measurements, and we do not attempt to

list slip lengths for various materials here (see [5] for a summary of slip length measurements). In hydrophobic materials, slip lengths are typically on the order of nanometers, though some have recorded slip lengths of microns [21, 22]. In electroosmotic flow, the characteristic length, the Debye length, is typically on the order of nanometers, so slip can have a very significant impact on bulk flow properties.

Several observables have been used to infer slip properties, including the flow rate–pressure relation in a channel, drainage forces observed between sufaces moved in relation to each other, and electrokinetic phenomena. One standard indirect method for measuring slip is to apply a known pressure gradient across a channel and measure the flow rate [15, 17, 34–36]. Slip in the system will lead to a larger flow rate than that expected from a model based on the no-slip boundary condition. For a circular microchannel,

$$\frac{Q(b)}{Q_{NS}} = 1 + \frac{4b}{a} \tag{3.3}$$

where Q is the slip flow rate, Q_{NS} is the flow rate if no-slip is assumed, and a is the radius of the channel. Another macroscopic technique involves measuring the viscous force opposing the drainage of a liquid film between hydrophobic surfaces [18, 37–41] and comparing to theoretical models [9, 42–45]. The presence of slip in the system reduces the apparent viscous resistance to draining. Two techniques for measuring drainage force have been developed; the surface force apparatus (SFA) and atomic force microscopy (AFM). The SFA was originally invented to measure van der Waals forces through a gas [46], but was adapted to measure forces between solids immersed in liquids by Israelachvili et. al [37]. An SFA uses interferometry to measure the distance between a stationary solid surface and a mobile one, and a spring attached to the mobile surface to measure the force acting on the surfaces. The SFA is now routinely used for measurements of slip length [24]. In AFM, a colloidal sphere attached to a flexible cantilever with known mechanical properties is brought in close proximity to a surface, and the

deflection of the cantilever is measured [14, 26, 29]. Sedimentation has also been used to measure slip [14], where colloids experiencing slip sediment faster than expected.

Electrokinetic phenomena result in macroscopically observable quantities which are expected to be largely affected by slip, due to the localization of shear to the double layer, which is typically small as compared to the dimensions of a microchannel. Churaev et. al [16] used streaming potential to study slip in methylated quartz capillaries. Streaming potentials measured in the presence of slip are expected to be larger than those measured in the absence of slip (see §3.4.4, specifically Equation 3.7). When compared to traditional techniques, there is a key problem with electrokinetic observation, which limits its use in measurement of slip. Streaming potential and electroosmosis are both functions of two unknowns that are difficult to measure independently: the electrokinetic potential, ζ, and the slip length, b. In order to get an estimate of ζ, Churaev et. al used a non-ionic trisiloxane surfactant to render their methylated quartz hydrophilic, claiming that the surfactant influenced the surface potential only weakly, and made the surface no-slip. Precise measurements of slip lengths through electrokinetic observation, however, requires either a method for measuring the ζ potential that is unaffected by slip, or a combination of techniques that are affected by slip differently.

Various velocimetry techniques have been used for measuring slip at the solid–liquid interfaces more directly. In particle image velocimetry (PIV), passive tracer particles are added to the flow and observed optically [19, 21, 22, 47]. In microfluidics applications, the tracer particles can be hundreds of nanometers in diameter, and the technique is referred to as micro–PIV [19,21,22]. The resolution of micro–PIV is limited by the depth of field of the observation optics, and since tracer particles must be small enough to negligibly affect the flow field, errors may be introduced from particle diffusion, which must be corrected in post processing [21,22]. Evanescent field illumination has beeen utilized

in order to increase the resolution of PIV, in which case the technique is referred to as nano–PIV [47, 48]. When using velocimetry methods to observe electroosmotic flow, it is important to take the electrophoretic mobility of the tracer particles into account [48].

3.4.3 Dependence of slip on physical parameters

The origin of slip in microfluidic systems is not well understood. In general, hydrophilic systems have been shown to have very small or negligible slip lengths [18, 20, 40, 41], while hydrophobic systems have significant slip [14–31]. Although the slip length does systematically increase with hydrophobicity of the substrate, it is only weakly correlated with its contact angle [5]. Examining the dependence of slip on a variety of physical parameters can help in understanding how the surface properties of hydrophobic substrates lead to the generation of slip.

Molecular dynamics simulations [49] and experiments [30, 41, 50] have shown that roughness tends to decrease slip. This is critical because microfluidic devices are usually the product of chemical etches (on glass or silicon) and/or templated synthesis (soft lithography, hot embossing, injection molding, replica molding, etc.), and these processes typically lead to a surface that is rough on the atomic level. Results on atomically-smooth mica [29, 37, 50] or even organosilane-modified Si wafers [51–55] may not be representative of the results on microfluidic substrates, nor can colloidal results with oil droplets be assumed to be representative of the roughness expected on the surfaces of microfluidic devices. Roughness induces local flows which lead to viscous dissipation of mechanical energy; essentially the same mechanism which leads to the no-slip boundary condition in typical flows. A number of experiments have also shown slip to depend on the shear rate ($b = b(\dot{\gamma})$) [15, 17, 18, 30, 31, 56–59], in which case Equation

3.2 is non-linear. Models that have been developed for shear-dependent slip are often based on the postulate that a layer of gas bubbles exists at the interface [9, 60–64]. A layer of gas in between the bulk solution and the solid channel wall has in general a non-zero velocity at the fluid–fluid interface, which defines a local apparent slip length as

$$b = h\left(\frac{\eta_1}{\eta_2} - 1\right) , \tag{3.4}$$

where h is the thickness of the low viscosity layer, η_1 is the bulk solution viscosity and η_2 is the viscosity of the gas layer. Some slip measurements are unsteady, which means that the size of the gas/bubble layer will be a function of the instantaneous pressure distribution in the fluid. As is the case with interfacial charge formation, the structure of water at the interface can have a large effect on slip (See §3.5).

Slip has been shown to depend on the type and quantity of dissolved gas in solution [14, 65, 66], supporting the notion of nanobubbles or a region of depleted water density at fluid–hydrophobe interfaces. In [14], Boehnke et. al demonstrated that (1) solvophilic beads had sedimentation velocities that were not a function of dissolved gas and (2) beads in degassed solution had sedimentation velocities that were not a function of the solvophilic/solvophobic nature of the material; however, they showed that solvophobic beads in solutions in contact with air had higher sedimentation velocities than the same system in contact with vacuum. Using an SFA to study a tetradecane interface, Granick et. al [65] showed that a system saturated with CO_2 obeyed no-slip boundary conditions, while a system saturated with Ar deviated significantly from no-slip. This can be explained by specific bonding of CO_2 with H_2O, which differentiates it from other gases such as Ar, N_2, and O_2, and is also responsible for the anomalously high solubility of CO_2 [67–69]. With PIV experiments, Tretheway et. al [66] measured the slip length as a function of absolute pressure, and showed that the measured slip length decreases with increasing absolute pressure. From these observations, it is clear that

dissolved gases influence slip phenomena, though the mechanism by which it occurs is unclear (to be discussed more in §3.5).

3.4.4 Slip in electrokinetic systems

If the slip boundary condition given by Equation 3.2 is applied to electroosmotic flow, then in the Debye–Hückel limit with uniform fluid properties, the resulting electroosmotic velocity, u_{EO} is

$$u_{EO} = -\frac{\epsilon E}{\eta}\zeta\left(1 + b^*\right) \ , \tag{3.5}$$

where $b^* = b/\lambda_D$ is the slip length normalized by the Debye length. Similarly, in pressure driven flow, the streaming potential with the slip boundary condition becomes [16]

$$\Delta\phi = \frac{\epsilon \Delta P}{\eta\sigma}\zeta\left(1 + b^*\right) \ , \tag{3.6}$$

where once again the Debye–Hückel limit and spatially uniform solution conductivity have been assumed. In both cases, if the effect of slip is ignored, the measured or apparent zeta potential, ζ_a, inferred from electrokinetic measurements will be larger than the potential drop across the EDL.

$$\zeta_a = \zeta\left(1 + b^*\right) \tag{3.7}$$

The Debye parameter, λ_D, can be quite small ($\sim$ 10 nm when the counterion concentration is 1 mM), so slip can have a significant effect on electrokinetic systems. Since slip leads to an effective ζ potential that has precisely the same form in both the electroosmotic velocity and the streaming potential, measurements of these two quantities cannot be used to infer both the slip length and the ζ potential in the Debye–Hückel limit. In order to decouple the slip length parameter from the ζ potential, either a ζ-potential

measurement which is not affected by slip, or an independent measurement of the slip length is necessary.

In the Debye–Hückel limit, Yang and Kwok have expanded this result for infinite flat plates. They have reported via an analytical result for thin double layers [70] that an additional correction term needs to be added, which accounts for the relative increase in flow-induced ion transport (current) attendant with increasing slip:

$$\zeta_a = \frac{\zeta\,(1+b^*)}{1+\frac{b}{a}\frac{\epsilon}{\eta D}\zeta^2}\,, \tag{3.8}$$

where $2a$ is the distance between the plates and D is the diffusivity of the ions. Relaxing the thin DL limit, they have reported results numerically for flat plates [71], circular channels [72], and rectangular channels [73], with qualitatively similar results.

In the presence of slip, the errors introduced by linearizing the Poisson–Boltzmann as in Equation 3.5 can be quite large. It is illustrative to examine the full non-linear Poisson–Boltzmann equation for the case of a symmetric z:z electrolyte on a flat plate with a given ζ potential. The apparent zeta potential, ζ_a, now takes the form

$$\zeta_a = \zeta\left[1+b^*\frac{2}{z\zeta^*}\sinh\left(\frac{z\zeta^*}{2}\right)\right]\,, \tag{3.9}$$

where $\zeta^* = \frac{\zeta}{k_B T/e}$. Apparent ζ potentials are plotted in Figure 3.2 for a variety of parameters. It is clear from all of the plots in Figure 3.2 that the linearized solution fails as ζ increases. In addition, the non-linear Poisson–Boltzmann equation introduces a dependence on the valence of the electrolyte, z, which is not present in the linearized solution. Comparison of Figure 3.2a to Figure 3.2b (or Figure 3.2c to Figure 3.2d) shows that the Debye–Huckel approximation becomes worse for ions of larger charge. Finally, Figures 3.2c and 3.2d show that the Debye–Hückel approximation becomes worse as the slip length increases. For cases of a general electrolyte solution, Equation 2.3 must be solved numerically. Numerical results for an electrolyte with a 2:1 ratio of

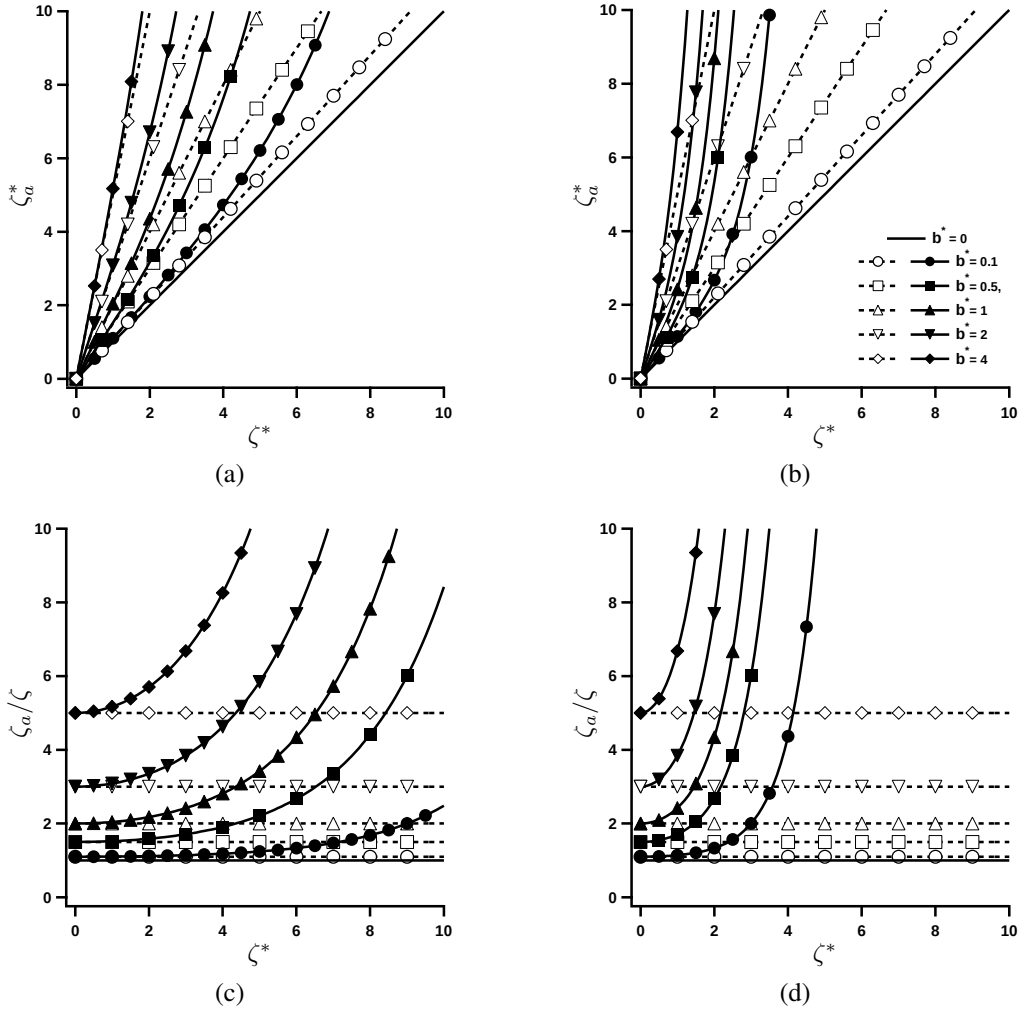

Figure 3.2: Plots of (a) ζ_a^* vs. ζ^* for a 1:1 electrolyte, (b) ζ_a^* vs. ζ^* for a 3:3 electrolyte, (c) ζ_a/ζ vs. ζ^* for a 1:1 electrolyte, and (d) ζ_a/ζ vs. ζ^* for a 3:3 electrolyte. Closed symbols and solid lines correspond to the nonlinear solution to the Poisson-Boltzmann Equation (Equation 3.9). Open symbols and dashed lines correspond to the Debye–Hückel approximation (Equation 3.5). $\zeta_a^* = \frac{\zeta_a}{k_B T/e}$ and $\zeta^* = \frac{\zeta}{k_B T/e}$. For reference, $k_B T/e$ at room temperature (293K) is 25 mV.

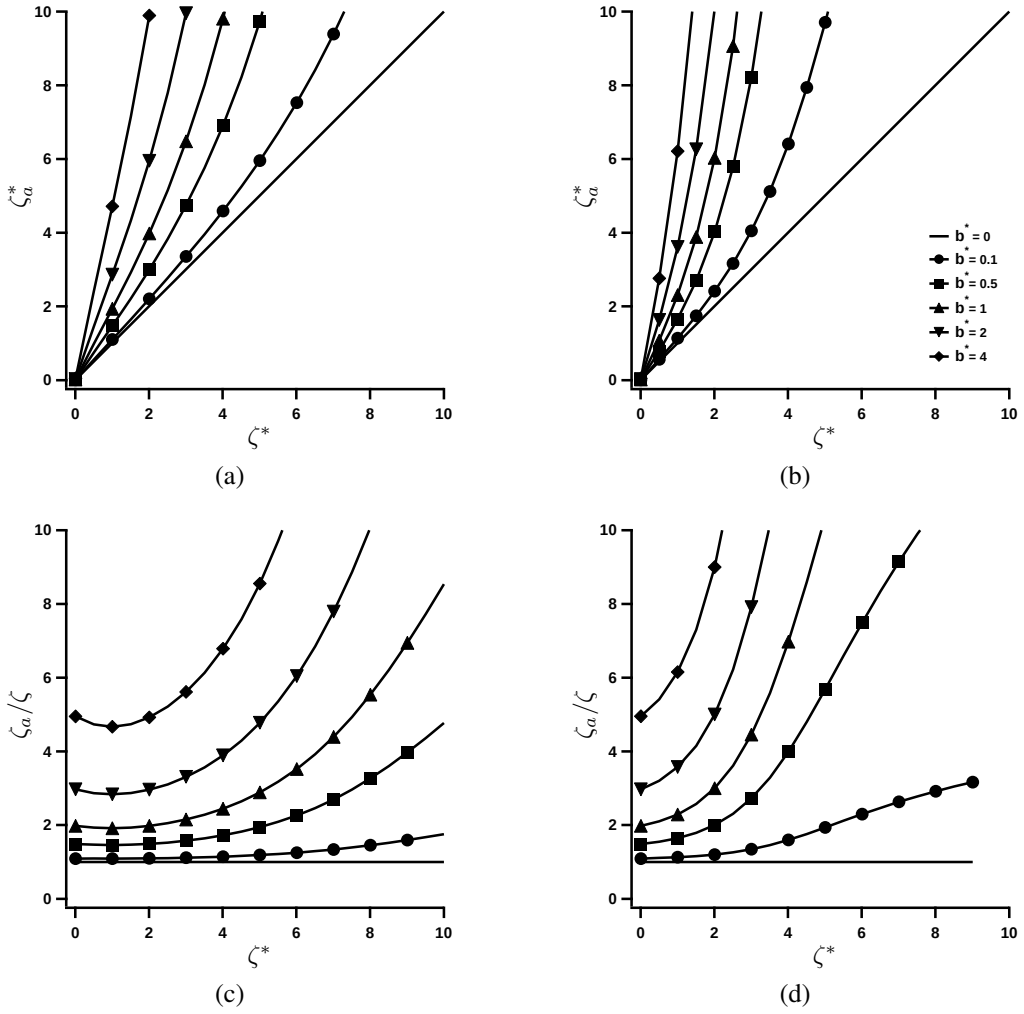

Figure 3.3: Numerical solutions to Equation 2.3 for a 2:1 ratio of monovalent anions to divalent cations over a flat plate. (a) ζ_a^* vs. ζ^* for a positively charged plate, (b) ζ_a^* vs. ζ^* for a negatively charged plate, (c) ζ_a/ζ vs. ζ^* for a positively charged plate, and (d) ζ_a/ζ vs. ζ^* for a negatively charged plate. $\zeta_a^* = \frac{\zeta_a}{k_B T/e}$ and $\zeta^* = \frac{\zeta}{k_B T/e}$. For reference, $k_B T/e$ at room temperature (293K) is 25 mV.

monovalent anions to divalent cations are shown in Figure 3.3. Interestingly, the ratio ζ_a/ζ goes through a minimum as a function of ζ for large enough slip lengths. This simple analysis demonstrates that the presence of slip in electrokinetic systems can lead to large deviations from no-slip behavior. It should be noted, however, that this analysis assumes a constant slip length to facilitate analytical treatment. At present, the true nature of slip and its dependence on input parameters is largely unknown.

Few experiments directly addressing the effects of slip in electrokinetic systems have been conducted. As discussed earlier, Churaev et. al [16] used streaming potential measurements in an attempt to infer the slip length for methylated quartz in aqueous solution. They used a surfactant to render the substrate hydrophilic, and claimed that the modified quartz gave a good estimate for the true (slip-free) ζ potential. This is at best an estimate, however, and in general it is very difficult to decouple b from ζ.

MD simulations of electrokinetics in hydrophobic microfluidic channels at finite temperature predict a breakdown of the Boltzmann approximation assumed in Equation 2.3 [74]. Ion concentration distributions oscillate near the fluid–solid interface, in a manner consistent with some modified Poisson–Boltzmann approaches. The immobile Stern layer of charges is present in hydrophilic surfaces, but absent in hydrophobic surfaces. Motion of ions near the interface result in slip in the hydrophobic case, which is well-described by Equations 3.2 and 3.5. In this study, Joly et. al chose to describe charge interaction via an effective dielectric media. This description was very successful in demonstrating the role of condensed ion layers effects in slip, though full atomistic simulation of the water molecules may be necessary in order to understand the interplay between slip and charge formation at the interface. Such a simulation is very challenging, since electrostatic interactions are long range, and computations of long range pair potentials for significant numbers of molecules is very costly.

3.4.5 Slip: Conclusions and Recommendations

Slip can be of utmost importance in electrokinetic systems; however, detecting its presence is difficult owing to the close coupling between the slip length and the interfacial potential, both of which are typically unknown *a priori*. The complexities involved in

these phenomena are closely related to ion condensation and ambiguity in the location of the Outer Helmholtz Plane [75] — both of these issues lead to additional challenges when linking origins of surface charge to electrokinetic phenomena. Slip most likely is ubiquitous in hydrophobic systems, though the relationship between slip and any measurable quantification of hydrophobicity (e.g. contact angle) is unclear. The presence of dissolved gases has consistently been shown to affect slip, possibly through interfacial gas/vapor layers (to be discussed further in §3.5). Slip is especially important in electrokinetic systems, owing to the high shear rates present in the double layer during electroosmosis, and the sensitivity of electrical currents to fluid motion near the channel wall in streaming potential. We have shown through simple analytical/numerical calculations that the presence of slip reduces the applicability of the Debye–Hückel approximation; an effect that is worse for electrolyte ions of larger charge. Furthermore, the slip length, b, and the electrokinetic potentia, ζ, are coupled in macroscopically observable electrokinetic phenomena, making their independent measurement difficult.

Since the presence of slip increases the importance of the non-linearity of the Poisson–Boltzmann equation, it may be possible to design experiments where deviations from the Debye–Hückel approximation are measurable. Induced-charged electrokinetic effects may play a role, since they provide more convenient access to large surface potentials, though these limits also require more advanced double layer modeling [76, 77]. In that case, different electrokinetic phenomena, such as streaming potential and electroosmosis, may exhibit measurably different dependencies on b and ζ. It may also be possible to find surfactants that remove slip from electrokinetic systems, but leave the surface potential unchanged, as was attempted in [16]. More experiments characterizing such surfactants are necessary, though determining their effect on the electrokinetic potential is nontrivial. Owing to the challenges involved, very few attempts have been made to measure slip in electrokinetic systems, but such experiments are necessary in

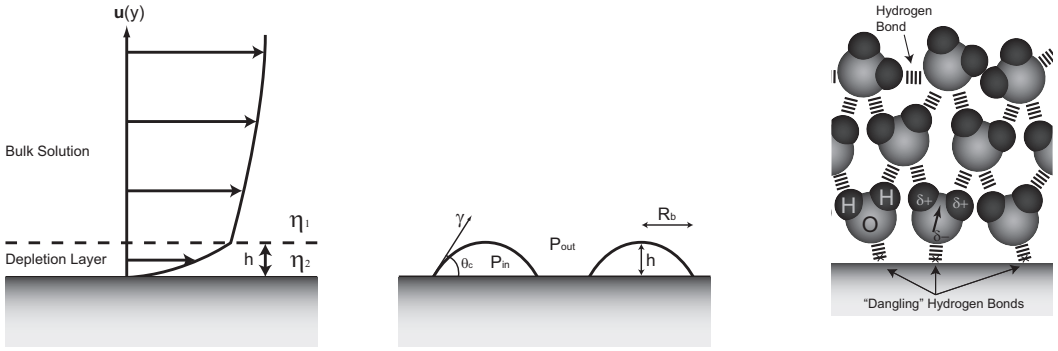

(a) (b) (c)

Figure 3.4: Schematics of (a) a depletion layer, (b) roughly hemispherical nanobubbles, and (c) structuring of water on hydrophobic microfluidic substrates. In (c), the dipole moment direction on a representative water molecule is indicated by an arrow.

order to better understand the interplay between slip and electrokinetics.

3.5 Interfacial Water Structure

Both the molecular (1 $\mathring{A}$) and nanofluidic (1–100 nm) structure of water at hydrophobic interfaces are related to the electrokinetic performance of microfluidic devices through their roles in interfacial slip, chemistry, and adsorption. For hydrophobic substrates in particular, water structuring effects may even dominate the surface properties e.g., interfacial charge, slip, and viscosity [78], in which case they would also dominate the electrokinetic response of the system. Macroscopic thermodynamic modeling suggests that changes in entropy drives the formation of ordered water structures at hydrophobic interfaces [79], and that such structures can facilitate preferential adsorption of ions [80, 81]. In the context of slip in hydrophobic microfluidic devices, the interfacial structure has been described in terms of a vapor/gas layer or a layer of depleted water density [60, 61]. Data from recent AFM experiments supports an alternative description, where instead of a continuous gas layer, there exist unstable gaseous nanobubbles at the hydrophobic

interface [82].

3.5.1 Depletion Layers

When examining slip in hydrophobic systems, Ruckenstein et. al [60] considered the possibility of a gaseous gap existing between the solid surface and the liquid due to partial or complete dewetting, rather than treating the molecules of liquid as slipping directly on the channel wall. This idea was later extended to include the role of dissolved gases in determining the size and density of the gap [61, 62], and generalized into a notion of a boundary layer of depleted liquid density (Figure 3.4a) [9]. This depletion layer would have a lower viscosity than the bulk solution (leading to apparent slip as described by Equation 3.4), but need not be an essentially frictionless liquid–gas interface. In addition to introducing apparent slip, the existence of a depletion layer also alters the surface chemistry and ion adsorption [78], which could lead to some of the ion concentration effects measured at air water interfaces discussed in [2].

X-ray reflectivity [54, 55, 83], neutron reflectivity [52, 53, 84], and AFM [85] experiments have been used to observe depletion layers at various hydrophobic interfaces, allowing for quantitative estimates of depletion layer thicknesses and densities (Table 3.1). X-ray reflectivity measurements generally report depletion layer thicknesses on the order of Angstroms, while the neutron reflectivity measurements report thicknesses on the order of nanometers. MD simulations [7, 83, 86] tend to agree more closely with the x-ray measurements than with the neutron experiments. Reported depletion layer densities vary in both types of measurement, though there is some ambiguity involved in defining both the thickness and the density. For example, Doshi et. al [53] fit their measured density profile to error functions, and defined the depletion layer thickness as

the point at which the water density is equal to half the bulk value; Grigera et. al [86] examined the angular distribution function of water molecules near the surface, which becomes constant in the bulk. AFM has also been used to measure a depletion layer thickness of 10 nm for stearylated silica particles in water [85], but AFM gives no information about the density. For water–octadecyl trichlorosilane (OTS) interfaces, Mezger et. al [55] also explored the effect of dissolved gases (Ar, Xe, Kr, N_2,O_2,CO,CO_2,and HCl), and concluded that they did not significantly influence the depletion layer. Doshi et. al, however, also worked with OTS interfaces, and found that the depletion layer thickness varied across Ar treated, CO_2 treated, degassed and naturally aerated solutions , though the variations were not more than 25%. Observation of the existence of a depletion layer even in degassed solutions [53–55] is quite significant, because it suggests that dissolved gases are not required for dewetting, and that the depletion layer is inherent to water–hydrophobe interfaces. Thus understanding of micro/nano fluidics in hydrophobic substrates requires careful attention to these non-uniform fluid density effects at the interface.

3.5.2 Nanobubbles

Nanobubbles, irregular networks of unstable gas bubbles approximately 30 nm in height and 100–300 nm in radius (Figure 3.4b), are an alternative (though not necessarily contradictory) description of the structure of hydrophobic interfaces [10]. The existence of nanobubbles at water–hydrophobe interfaces was initially postulated to explain the long-range (10–100 nm) attraction observed between two hydrophobic surfaces, where the attractive force as a function of separation distance was found to have large step changes [87–94]. These step changes are attributed to the coalescence of nanobubbles, and the magnitude of the expected attractive force change resulting from a bridging

Table 3.1: Summary of depletion layer measurements

	Interface	**Contact Angle**	**Depletion Layer Thickness**	$\frac{\rho\text{depletion layer}}{\rho\text{bulk}}$
Jensen et al. [83]: X-ray reflectivity and MD	Water–paraffin	112°	15 $\AA$	0.9
Poynor et al. [54]: X-ray reflectivity	Water on methyl-terminated octadecyl silane monolayers	$> 100°$	2–4 $\AA$	0.4
Mezger et al. [55]: X-ray reflectivity	Water-OTS	$> 100°$	3.8 $\AA$	0.71
Steitz et al. [84]: Neutron reflectivity	D_2O–polystyrene	–	20–50 Å	.88–.94
Schwendel et al. [52]: Neutron reflectivity	D_2O on SAMs	–	41.8 $\AA$	.869
Doshi et al. [53]: Neutron reflectivity	D_2O–OTS	100.7–113.4°	28–35 $\AA$	.5
Knoben et al. [85]: AFM	Stearylated silica in water	100–110°	10 nm	–
Mamatkulov et al. [7]: MD	SPC/E water model with hydrophobic alkane slab	–	2.5 $\AA$	–
Grigera et al. [86]: MD	SPC/E water model with a wall of neutral atoms	–	4 $\AA$	–

event has been shown to be thermodynamically consistent with experimental observations [87, 95].

Though nanobubbles are compelling in light of the hydrophobic force measurements, they are controversial owing to the fact that their thermodynamic stability requires nanocavities, double layer interactions, diffusive non-equilibrium, or a breakdown in the applicability of classical descriptions of surface tension and its effects via the Young–Laplace equation. The Young–Laplace equation gives the relationship between a bubble's size and its internal pressure.

$$P_{in} = P_{out} + \frac{2\gamma}{R_b} \tag{3.10}$$

where P_{in} and P_{out} are the pressures inside and outside of the bubble respectively, γ is the surface tension, and R_b is the radius of curvature of the nanobubble. Thus, a nanobubble 10 nm in radius requires an internal pressure of about 144 atm, meaning that it cannot be in equilibrium with the atmosphere, and is expected to dissolve very quickly. An estimate of the time scale for the dissolution of nanobubbles is given by the time scale for diffusion of a spherical gas bubble into the liquid [96, 97].

$$\tau \sim \frac{M p_o a^2}{D c_o R T} \left(1 + \frac{p_o R_b}{\gamma}\right) \tag{3.11}$$

where M is the molar mass, p_o is the far field pressure, D is the diffusion coefficient of the gas in the liquid, c_o is the concentration of the gas, T is the temperature, R is the gas constant, R_b is the radius of the bubble, and γ is the surface tension. Lauga et. al [5] point out that $\tau \approx 10\mu$s for R_b =10 nm, though it is important to realize that Equations 3.10 and 3.11 strictly apply for a gas bubble surrounded by fluid in equilibrium with the atmosphere; they do not take into account the presence of a hydrophobic surface, which through surface interactions may slow the kinetics of dissolution. Nevertheless, nanobubbles have experimentally been shown to be stable for much longer than expected. One possible explanation is offered by Attard et. al [10, 87, 90, 95], who showed that if the bubbles are not in diffusive equilibrium with the atmosphere over macroscopically observable timescales (i.e. they are in a supersaturated solution), the nanobubbles can be thermodynamically stable, and should be modeled using an isobaric chemical potential (fixed number of gas molecules) rather than the grand chemical potential (global equilibrium). For this to be possible, they further proposed that the nanobubbles are in equilibrium with a locally supersaturated solution, though the origin of the supersaturation is unclear. Attard et. al also showed that it is thermodynamically feasible for the interfacial structres to instead take the form of supramolecular vapor voids, a description supported by Ljunggren et. al [97]. Experiments show the bubbles/voids to be stable for hours, which could be indicative of a diffusion limited process. The pres-

ence of nanocavities allow nanoscale gas regions to exist without nanoscale curvature, which further explains nanobubble stability. The microscale analogy of nanocavities are superhydrophobic surfaces [98].

Perhaps the most compelling evidence for the existence of nanobubbles comes from direct observation of water–hydrophobe interfaces with tapping mode AFM [10, 51, 82, 84, 99–102]. Hydrophobic surfaces in water have distinct roughness features, which are absent in dry hydrophobic or wet hydrophilic surfaces. Phase AFM images reveal that the roughness features consist of a much softer material than the bulk substrate [10]. Furthermore, the roughness features are not observable with contact mode AFM imaging, suggesting that the force applied in contact mode destroys or displaces these roughness features. Thee roughness features have thus been postulated to be gas nanobubbles. Average/typical values for nanobubble morphology are summarized in Table 3.2. Descriptions of the general features of nanobubble morphology have differed among different investigators. Attard's group has generally observed bubbles of irregular cross-section [10, 82, 99], while others have observed hemispherical objects of regular circular cross-section [51, 84, 100–102]. Both descriptions may be correct, as the nanobubble morphology is likely to be a function of both the solution conditions and the substrate material. For example, experiments by Tyrrell et. al [99] showed that nanobubble morphology varies as a function of solution pH. At pH 3, the bubbles coalesced into larger regular structures, while at pH 9.4, the mean area of the bubbles was reduced and the distinction between nanobubble domains was enhanced. They propose that this is likely due to enhanced surface charge on the bubbles at higher pH, leading to stabilization due to electrostatic repulsion.

Examination of the role of dissolved gases [88, 91, 94, 102, 103] on the formation and morphology of nanobubbles may elucidate information about their composition

(gas vs. vapor), and may also help determine the effect of nanobubbles on the performance of electrokinetically driven microfluidic devices. Measurements of the hydrophobic force with AFM/SFA have shown that its range decreases in degassed solutions [88, 91, 94, 103]. Using an optical cavitation method, Vinogradova et. al [104] found that the addition of dissolved gases enhances nucleation of nanobubbles on hydrophobic surfaces. This contradicts the findings of Ishida et. al [94], who found with AFM measurements of OTS on Si substrates that dissolved gases had no effect on the range of the hydrophobic force. However, they also found that surfaces that were not exposed to air before they were immersed in water and measured with AFM did not have nanobubbles, while surfaces which had been exposed to air prior to measurement did [51, 51]. Zhang et. al [102] compared tapping mode AFM images of water–mica interfaces taken with non-degassed and degassed solutions, and found that the nanobubble density decreased from 2.9 per μm^2 to nearly zero with degassing. Further study is required in this area in order to draw conclusions about the composition of nanobubbles, but it is clear that exposure to air and/or dissolved gases leads to nanobubble morphology changes, which can lead to uncertainties in electrokinetic actuation in hydrophobic microfluidic devices.

As with depletion layers, nanobubbles can drastically affect the electrokinetic performance of microfluidic devices by introducing a slip boundary condition and altering the surface chemistry. Lauga et. al [5, 63, 64] have modeled the effect of nanobubbles on slip, and point out three key differences between nanobubbles and depletion layers. First, the flow inside nanobubbles recirculates, decreasing the slip length estimate given by Equation 3.4. Second, no-slip regions between the bubbles decrease slip further. Third, nanobubbles are generally not flat, which decreases the slip further. In addition, owing to instabilities and coalescence, nanobubbles are dynamic, which means that their formation and dissolution over time will lead to transients in the electrokinetic response

Table 3.2: Summary of AFM nanobubble measurements

	Interface	**Bubble Radius of Curvature (nm)**	**Bubble height (nm)**
Ishida et al. [51]	Water–OTS	220–600	38
Tyrrell et al. [10,82, 99]	Water–Methylated Glass	100–300	20–30
Lou et al. [100]	Water–Graphite	–	–
Steitz et al. [84]	Water–Polystyrene	25–60	20
Simonsen et al. [101]	Water–Polystyrene	66.7	6.6
Zhang et al. [102]	Water–Mica	–	–

of a system. This can be crucial in hydrophobic microfluidic devices, since solvent and/or temperature changes can lead to the nucleation and dissolution of nanobubbles.

3.5.3 Hydrogen-Bonded Water Molecule Networks

When considering ion adsorption onto hydrophobic surfaces in aqueous media, it is important to understand that the structure of water at the interface is likely to dominate the thermodynamics of binding events [6, 79]. In addition to the macroscopic (depletion layers) and supramolecular (nanobubbles) structures which have already been discussed, the molecular structure of water at hydrophobic surfaces has been shown to impact both slip and ion adsorption [6–8, 81, 105–108]. Using MD simulations, Lee et. al [105] showed that water forms an oriented ice-like structure at extended hydrophobic surfaces. The molecules nearest to the surface are oriented such that only one hydrogen bonding group faces the surface, an arrangement referred to as dangling hydrogen bonds (Figure 3.4c). This structure results from the competition between the tendencies of the liquid to maximize hydrogen bonds, and to maximize packing density. Zangi et. al [8] further showed that the ordered structure leads to an electrical potential gradient

that strongly and favorably interacts with the dipole moments of hydroxyl ions, leading to their spontaneous adsorption. Additional MD studies have shown that oriented water molecules can also stabilize adsorbed ions, and that the dynamics of ion hydration play a significant role during an electrolyte ion's approach to a hydrophobic surface [6,7,106]. Mamatkulov et. al [7] observed the formation of a depletion layer as a result of the water's molecular structure, relating the structure of water at the hydrophobic interface to slip phenomena.

The tendency of water to form ordered hydrogen-bonded structures near extended hydrophobic surfaces has been confirmed experimentally through spectroscopic measurements of air–water interfaces [81,107,108]. Raduge et. al [107] used sum frequency generation (SFG) to observe the interface between air and aqueous sulfuric acid. They reported three characteristic peaks at 3670 cm^{-1}, 3200 cm^{-1} and 3400 cm^{-1}, which correspond to dangling OH bonds at the surface, hydrogen bonded OH groups associated with ice-like structures, and less ordered local bonding structures respectively. As they increased the H_2SO_4concentration, they found that the 3670 cm^{-1} peak disappeared, which they attributed to the interaction of H_2SO_4 molecules with the dangling OH groups. Baldelli et. al [108] obtained similar results, but interpreted them differently, stating that ionic species tend to orient water molecules into ordered structures more than in the neat air–water interface. Using SFG and ATR–FTIR (attenuated total reflection Fourier transform infrared) spectroscopy, Liu et. al [81] demonstrated that different ions can affect the hydrogen bonded water structure differently. The water structure in the presence of smaller ions such as Fl^- and Cl^- is very similar to that of the neat air–water interface, while larger ions such as Br^- and I^- tend to distort the hydrogen bonded network significantly. Consequently, Liu et. al also observed enhanced concentration of the larger ions only, suggesting that the distortion and/or reorientation of the hydrogen bonded network plays a crucial role in preferential ion adsorption. This

is critical in microfluidics, as it affects the surface charge, and ultimately the electrokinetic performance of hydrophobic devices.

3.5.4 Interfacial Water Structure: Conclusions and Recommendations

Interfacial charge formation and slip on hydrophobic surfaces are likely to be dependent on (a) the structure of water at the interface, and (b) the presence of dissolved gases. The existence of ordered water structures at hydrophobic interfaces is predicted by MD simulaitons [6–8], which are in good agreement with spectroscopic experiments [81, 107, 108]. The impact of these structures on interfacial charge formation is an area that warrants further investigation. MD simulations have shown that ordered water structures can facilitate adsorption of hydroxyl ions [8], though to the authors' knowledge direct experimental evidence for this phenomenon is lacking. The distortion of these water structures has been shown via spectroscopic measurements to correspond with preferential anion adsorption [81]; future investigations here should be focused on thermodynamic modeling of these systems.

Observed regions of depleted water density near the interface are likely to be related to water structuring [7]. From neutron/x-ray reflectivity [52–55, 83, 84] and AFM [85] experiments, the characteristics of the depletion layer appear to be only marginally affected by the presence of dissolved gases, if at all. These depletion regions are also generally observed regardless of whether solutions are degassed. Though the composition of the depletion layer is essentially unknown, these data suggest that the depletion region is better described as a vapor layer, rather than as a gas layer. In either case, the fluid in the depletion region has properties that differ from their bulk values (e.g., viscos-

ity, permittivity); this lends credibility to the postulate that a low viscosity layer near the interface leads to slip. Nanobubbles are likely to exist at hydrophobic interfaces in addition to the depletion region, though unlike depletion layers, they tend to be less prolific in degassed solutions [51,88,91,94,103]. This suggests that the bubbles are more likely to contain of gas rather than vapor, though their composition is also uncharacterized at this point. Future experiments should focus on determining the composition of these interfacial structures either spectroscopically or chemically. Nanobubbles also introduce slip at the interface, though there are fundamental differences between depletion layers and nanobubbles in this respect as discussed in [5].

Since nanobubbles are unstable, and likely to be linked with slip and interfacial charge, they are expected to lead to transients in the macroscopically observable properties of hydrophobic microfluidic systems as they form/dissolve over time. Thus, it would interesting to see how changes in the molecular/nanofluidic structures at water–hydrophobe interfaces correspond to changes in the macroscopic properties of the system when the input parameters (i.e. pH, ionic strength, etc.) are varied, and over time.

3.6 Conclusions

It has been shown that the complex interplay between diffuse interfacial structures, interfacial chemistry, and slip phenomena result in electrokinetic behavior that is difficult to predict, and is highly dependent on both the solvent and the electrolytes considered. Despite the general complexity of these systems and a dearth of firm and rigorous conclusions, several noteworthy trends have been demonstrated.

Given interfacial charge and the attendant zeta potential as discussed in [2], we discuss the impact of interfacial slip on microdevice performance. The presence of slip can

be crucial in hydrophobic electrokinetic systems, due to the presence of high shear rates owing to the localization of shear to the double layer. Electrokinetic measurements in the presence of slip are especially difficult, since the slip length and electrokinetic potential are coupled in macroscopically observable phenomena, and both are unknown *a priori*. The concentration of dissolved gas in solution has consistently been shown to affect slip, suggesting that presence of gas or vapor at the interface could be the fundamental origin of slip. Given the important roles of dissolved gases in many bioanalytical systems, most microdevices will use working solutions with dissolved gases, and the effects of these gases, especially when perturbed by experimental protocols, must be taken into account. Through simple analytical and numerical calculations, we have shown that slip in electrokinetic systems also limits the applicability of the Debye–Hückel approximation. The Debye–Hückel approximation fails at lower ζ potentials in systems with larger slip lengths; this effect worsens with ions of larger valence.

Both slip and interfacial charge are likely to be affected by interfacial nanostructures on molecular or supramolecular scale. Hydrogen-bonded water networks at hydrophobic interfaces, which are important in both electrolyte and hydroxyl ion interfacial adsorption [2], may also correspond with a region of depleted water density at the interface, which has reduced viscosity when compared to the bulk solution, and generates an apparent slip boundary condition on the fluid velocity. Nanobubbles observed at these interfaces have a peculiarly slow dissolution rate, given their classically predicted instability. Thus the thermodynamics of nanobubble formation/dissolution are particularly interesting and challenging, though not currently well understood. Nanobubble dynamics are of critical interest when considering design of electrokinetic systems, as the dissolution of nanobubbles over time will lead to transient electrokinetic behavior owing to changes in surface chemistry and slip.

BIBLIOGRAPHY

[1] V. Tandon and B.J. Kirby. Zeta potential and electroosmotic mobility in devices fabricated from hydrophobic polymers: 2. slip and interfacial water structure. *Electrophoresis*, 29:1102–1114, 2008.

[2] V. Tandon, S.K. Bhagavatula, W.C. Nelson, and B.J. Kirby. Zeta potential and electroosmotic mobility in devices fabricated from hydrophobic polymers: 1. the origins of charge. *Electrophoresis*, 29:1092–1101, 2008.

[3] V.M. Gun'ko, V.V. Turov, V.M. Bogatyrev, V.I. Zarko, R. Leboda, E.V. Goncharuk, A.A. Novza, A.V. Turov, and A.A. Chuiko. Unusual properties of water at hydrophilic/hydrophobic interfaces. *Advances in Colloid and Interface Science*, 118:125–172, 2005.

[4] O. Teschke, G. Ceotto, and E.F. de Souza. Interfacial aqueous solutions dielectric constant measurements using atomic force microscopoy. *Chemical Physics Letters*, 326:328–334, 2000.

[5] E. Lauga, M.P. Brenner, and H.A. Stone. *Microfluidics: The No-Slip Boundary Condition*. Handbook of Experimental Fluid Dynamics. Springer, New York, 2005.

[6] L.X. Dang and T. Chang. Molecular mechanism of ion binding to the liquid/vapor interface of water. *Journal of Physical Chemistry B*, 106:235–238, 2002.

[7] S.I. Mamatkulov, P.K. Khabibullaev, and RR. Netz. Water at hydrophobic substrates: Curvature, pressure, and temperature effects. *Langmuir*, 20:4756–4763, 2004.

[8] R. Zangi and J.B.F.N. Engberts. Physisorption of hydroxide ions from aqueous solution to a hydrophobic surface. *Journal of the American Chemical Society*, 127:2272–2276, 2005.

[9] O.I. Vinogradova. Drainage of a thin liquid-film confined between hydrophobic surfaces. *Langmuir*, 11:2213–2220, 1995.

[10] P. Attard, M.P. Moody, and J.W.G. Tyrell. Nanobubbles: the big picture. *Physica A*, 314:696–705, 2002.

[11] R.J. Hunter. *Foundations of Colloid Science, Vol. 2*. Clarendon Press, Oxford, 1989.

[12] H.A. Stone, A.D. Stroock, and A. Ajdari. Engineering flows in small devices: Microfluidics toward a lab-on-a-chip. *Annual Review of Fluid Mechanics*, 36:381–411, 2004.

[13] T.M. Squires and S.R. Quake. Microfluidics: Fluid physics at the nanoliter scale. *Review of Modern Physics*, 77:977–1026, 2005.

[14] U.-C. Boehnke, T. Remmler, H. Motschmann, S. Wurlitzer, J. Hauwede, and Th. M. Fischer. Partial air wetting on solvophobic surfaces in polar liquids. *Journal of Colloid and Interface Science*, 211:243–251, 1999.

[15] C-H. Choi, K. Johan, A. Westin, and K.S. Breuer. Apparent slip flows in hydrophilic and hydrophobic microchannels. *Physics of Fluids*, 15(10):2897–2902, 2003.

[16] N.V. Churaev, J. Ralston, I.P. Sergeeva, and V.D. Sobolev. Electrokinetic properties of methylated quartz capillaries. *Advances in Colloid and Interface Science*, 96:265–278, 2002.

[17] N.V. Churaev, V.D. Sobolev, and A.N. Somov. Slippage of liquids over lyophobic solid surfaces. *Journal of Colloid and Interface Science*, 97:574–581, 1984.

[18] C.L. Henry, C. Neto, D.R. Evans, S. Biggs, and V.S.J. Craig. The effect of surfactant adsorption on liquid boundary slippage. *Physica A*, 339:60–65, 2004.

[19] P. Joseph and P. Tabeling. Direct measurement of the apparent slip length. *Physical Review E*, 71:035303, 2005.

[20] H. Hervet and L. Leger. Flow with slip at the wall: From simple to complex fluids. *C.R. Physique*, 4:241–249, 2003.

[21] D.C. Tretheway and C.D. Meinhart. Apparent fluid slip at hydrophobic microchannel walls. *Physics of Fluids*, 14(3):L9–L12, 2002.

[22] D.C. Tretheway and C.D. Meinhart. A generating mechanism for apparent fluid slip in hydrophobic microchannels. *Physics of Fluids*, 16(5):1509–1515, 2004.

[23] O.I. Vinogradova and G.E. Yakubov. Dynamic effects on force measurements. 2. lubrication and the atomic force microscope. *Langmuir*, 19:1227–1234, 2003.

[24] J. Baudry, E. Charlaix, A. Tonck, and D. Mazuyer. Experimental evidence for a

large slip effect at a nonwetting fluid-solid interface. *Langmuir*, 17:5232–5236, 2001.

[25] C. Cheikh and G. Koper. Stick-slip transition at the nanometer scale. *Physical Review Letters*, 91(15):156102, 2003.

[26] J.J. Cho, B.M. Law, and F. Rieutord. Dipole-dependent slip of newtonian liquids at smooth solid hydrophobic surfaces. *Physical Review Letters*, 92(16):166102, 2004.

[27] O.A. Kisleva, V.D. Sobolev, and N.V. Churaev. Slippage of the aqueous solutions of cetyltrimethylammonium bromide during flow in thin quartz capillaries. *Colloid J.*, 61:263–264, 1999.

[28] D. Lumma, A. Best, A. Gansen, F. Feuillebois, J.O. Radler, and O.I. Vinogradova. Flow profile near a wall measured by double-focus fluorescence cross-correlation. *Physical Review E*, 67:056313, 2003.

[29] G. Sun, E. Bonaccurso, V. Franz, and H-J. Butt. Confined liquid: Simultaneous observation of a molecularly layered structure and hydrodynamic slip. *Journal of Chemical Physics*, 117(22):10311–10314, 2002.

[30] Yingxi Zhu and S. Granick. Limits of the hydrodynamic no-slip boundary condition. *Physical Review Letters*, 88(10):106102, 2002.

[31] Y. Zhu and S. Granick. No-slip boundary condition switches to partial slip when fluid contains surfactant. *Langmuir*, 18:10058–10063, 2002.

[32] C.L.M.H. Navier. *Mmoire sur les lois du mouvement des fluides*. Mem. Acad. R. Sci. France, 1823.

[33] J.C. Maxwell. On stresses in rarefied gases arisng from inequalities in temperature. *Philosophical Transactions of the Royal Society of London*, 170:231–256, 1879.

[34] J. Pfahler, J. Harley, H. Bau, and J. Zemel. Liquid transport in micron and submicron channels. *Sensors and Actuators*, A21-A23:431–434, 1990.

[35] T. Hasegawa, M. Suganuma, and H. Watanabe. Anomaly of excess pressure drops of the flow through very small orifices. *Physics of Fluids*, 9(1):1–3, 1997.

[36] J.T. Cheng and N. Giordano. Fluid flow through nanometer-scale channels. *Physical Review E*, 65:031206, 2002.

[37] J.N. Israelachvili and G.E. Adams. Measurement of forces between two mica surfaces in aqueous-electrolyte solutions in range 0 to 100 nm. *J. Chem. Soc. Faraday Trans. I*, 74:975–1001, 1978.

[38] J.N. Israelachvili. Measurement of the viscosity of liquids in very thin films. *Journal of Colloid and Interface Science*, 110:263–271, 1986.

[39] O.I. Vinogradova, G.E. Yakubov, and H-J. Butt. Forces between polystyrene surfaces in water-electrolyte solutions: Long-range attraction of two types? *Journal of Chemical Physics*, 114(18):8124–8131, 2001.

[40] E. Bonaccurso, M Kappl, and H-J. Butt. Hydrodynamic force measurements: Boundary slip of water on hydrophilic surfaces and electrokinetic effects. *Physical Review Letters*, 88(7):076103, 2002.

[41] E. Bonaccurso, H-J. Butt, and V.S.J. Craig. Surface roughness and hydrodynamic boundary slip of a newtonian fluid in a completely wetting system. *Physical Review Letters*, 90(14):144501, 2003.

[42] O.I. Vinogradova. Hydrodynamic interaction of curved bodies allowing slip on their surfaces. *Langmuir*, 12:5963–5968, 1996.

[43] O.I. Vinogradova. Possible implications of hydrophobic slippage on the dynamic measurements of hydrophobic forces. *J. Phys. - Condens. Matter*, 8:9491–9495, 1996.

[44] O.I. Vinogradova. Implications of hydrophobic slippage for the dynamic measurements of hydrophobic forces. *Langmuir*, 14:2827–2837, 1998.

[45] O.I. Vinogradova and R.G. Horn. Attractive forces between surfaces: What can and cannot be learned from a jump-in study with the surface forces apparatus? *Langmuir*, 17:1604–1607, 2001.

[46] J.N. Israelachvili and D. Tabor. The measurement of van der waals dispersion forces in the range 1.5 to 130 nm. *Proceedings of the Royal Society of London A*, 331:19–38, 1972.

[47] C.M. Zettner and M. Yoda. Particle velocity field measurements in a near-wall

flow using evanescent wave illumination. *Experiments in Fluids*, 34:115–121, 2003.

[48] R. Sadr, M. Yoda, Z. Zheng, and A.T. Conlisk. An experimental study of electro-osmotic flow in rectangular microchannels. *Journal of Fluid Mechanics*, 506:357–367, 2004.

[49] A. Jabberzadeh, J.D. Atkinson, and R.I. Tanner. Effect of the wall rougness on slip and rheological properties of hexadecane in molecular dynamics simulation of couette shear flow between two sinusoidal walls. *Physical Review E*, 61(1):690–699, 2000.

[50] J.M. Georges, S. Millot, J.L. Loubet, and A. Tonck. Drainage of thin liquid films between relatively smooth surfaces. *Journal of Chemical Physics*, 98(9):7345–7360, 1993.

[51] N. Ishida, T. Inoue, M. Miyahara, and K. Higashitani. Nano bubbles on a hydrophobic surface in water observed by tapping-mode atomic force microscopy. *Langmuir*, 16:6377–6380, 2000.

[52] D. Schwendel, T. Hayashi, R. Dahint, A. Pertsin, M. Grunze, R. Steitz, and F. Schreiber. Interaction of water with self-assembled monolayers: Neutron reflectivity measurements of the water density in the interface region. *Langmuir*, 19:2284–2293, 2003.

[53] D.A. Doshi, E.B. Watkins, J.N. Israelachvili, and J. Majewski. Reduced water density at hydrophobic surfaces: Effect of dissolved gases. *PNAS*, 102(27):9458–9462, 2005.

[54] A. Poynor, L. Hong, I.K. Robinson, S. Granick, Z. Zhang, and P.A. Fenter. How water meets a hydrophobic surface. *Physical Review Letters*, 97:266101, 2006.

[55] M. Mezger, H. Reichert, S. Schoeder, J. Okasinski, H. Schroeder, H. Dosch, D. Palms, J. Ralston, and V. Honkimaki. High-resolution in situ x-ray study of the hydrophobic gap at the water-octadecyl-trichlorosilane interface. *PNAS*, 103(49):18401–18404, 2006.

[56] V.S.J. Craig, C. Neto, and D.R.M. Williams. Shear-dependent boundary slip in an aqueous newtonian fluid. *Physical Review Letters*, 87(5):054504, 2001.

[57] C. Neto, V.S.J. Craig, and D.R.M. Williams. Evidence of shear-dependent boundary slip in newtonian fluids. *Eur. Phys. J. E*, 12(s01):S71–S74, 2003.

[58] Y. Zhu and S. Granick. Rate-dependent slip of newtonian liquid at smooth surfaces. *Physical Review Letters*, 87(9):096105, 2001.

[59] Y. Zhu and S. Granick. Apparent slip of newtonian fluids past adsorbed polymer layers. *Macromolecules*, 35:4658–4663, 2002.

[60] E. Ruckenstein and N. Churaev. On the no-slip boundary condition of hydrodynamics. *Journal of Colloid and Interface Science*, 96:488–491, 1983.

[61] E. Ruckenstein and N. Churaev. A possible hydrodynamic origin of the forces of hydrophobic attraction. *Journal of Colloid and Interface Science*, 147:535–538, 1991.

[62] P.G. de Gennes. On fluid/wall slippage. *Langmuir*, 18:3413–3414, 2002.

[63] E. Lauga and H.A. Stone. Effective slip in pressure-driven stokes flow. *Journal of Fluid Mechanics*, 489:55–77, 2003.

[64] E. Lauga and M.P. Brenner. Dynamic mechanisms for apparent slip on hydrophobic surfaces. *Physical Review E*, 70:026311, 2004.

[65] S. Granick, Y. Zhu, and H. Lee. Slippery questions about complex fluids flowing past solids. *Nature Materials*, 2(4):221–227, 2003.

[66] D.C. Tretheway, S. Stone, and C.D. Meinhart. Effects of absolute pressure and dissolved gases on apparent fluid slip in hydrophobic microchannels. *Bull. Am. Phys. Soc.*, 49:215, 2004.

[67] H. Sato, N. Matubayasi, M. Nakahara, and F. Hirata. Which carbon oxide is more soluble? ab initio study on carbon monoxide and dioxide in aqueous solution. *Chemical Physics Letters*, 323:257–262, 2000.

[68] G.K. Anderson. Enthalpy of dissociation and hydration number of carbon dioxide hydrate from the clapeyron equation. *J. Chem. Thermodynamics*, 35:1171–1183, 2003.

[69] A. Khan. Theoretical studies of $CO_2(H_2O)$ 20,24,28 culsters: stabilization of cages in hydrates by CO_2 guest molecules. *J. Mol. Struct. (Thermochem)*, 664-665:237–245, 2003.

[70] J. Yang and D.Y. Kwok. A new method to determine zeta potential and slip

coefficient simultaneously. *Journal of Physical Chemistry B*, 106:12851–12855, 2002.

[71] J. Yang and D.Y. Kwok. Effect of liquid slip in electrokinetic parallel-plate microchannel flow. *Journal of Colloid and Interface Science*, 260:225–233, 2003.

[72] J. Yang and D.Y. Kwok. Microfluid flow in circular microchannel with electrokinetic effect and navier's slip condition. *Langmuir*, 19:1047–1053, 2003.

[73] J. Yang and K.Y. Kwok. Time-dependent laminar electrokinetic slip flow in infinitely extended rectangular microchannles. *Journal of Chemical Physics*, 118(1):354–363, 2003.

[74] L. Joly, C. Ybert, E. Trizac, and L. Bocquet. Hydrodynamics within the electric double layer on slipping surfaces. *Physical Review Letters*, 93:257805, 2004.

[75] R.J. Hunter. *Zeta Potential in Colloid Science*. Academic Press, London, 1981.

[76] M.Z. Bazant and T.M. Squires. Induced-charge electrokinetic phenomena: Theory and microfluidic applications. *Physical Review Letters*, 92(6):066101, 2004.

[77] T.M. Squires and M.Z. Bazant. Induced-charge electro-osmosis. *Journal of Fluid Mechanics*, 509:217–252, 2004.

[78] R.R. Netz. Water and ions at interfaces. *Current Opinion in Colloid and Interface Science*, 9:192–197, 2004.

[79] C. Tanford. *The Hydrophobic Effect: Formation of Micelles and Biological Membranes*. John Wiley and Sons, New York, 1980.

[80] K.G. Marinova, R.G. Alargova, N.D. Denkov, O.D. Velev, D.N. Petsev, I.B. Ivanov, and R.P. Borwankar. Charging of oil-water interfaces due to spontaneous adsorption of hydroxyl ions. *Langmuir*, 12:2045–2051, 1996.

[81] D. Liu, G. Ma, L.M. Levering, and H.C. Allen. Vibrational spectroscopy of aqueous sodium halide solutions and air-liquid interface: Observation of increased interfacial depth. *Journal of Physical Chemistry B*, 108:2252–2260, 2004.

[82] J.W.G. Tyrrell and P. Attard. Images of nanobubbles on hydrophobic surfaces and their interactions. *Physical Review Letters*, 87(17), 2001.

[83] T.R. Jensen, M.O. Jensen, N. Reitzel, K. Balashev, G.H. Peters, K. Kjaer, and T. Bjornholm. Water in contact with extended hydrophobic surfaces: Direct evidence of weak dewetting. *Physical Review Letters*, 2003.

[84] R. Steitz, T. Gutberlet, T. Hauss, B. Klosgen, R. Krastev, S. Schemmel, A.C. Simonsen, and G.H. Findenegg. Nanobubbles and their precursor layer at the interface of water against a hydrophobic substrate. *Langmuir*, 19:2409–2418, 2003.

[85] W. Knoben, A.M. Besseling, and M.A. Cohen Stuart. Direct measurement of depletion and hydrodynamic forces in solutions of a reversible supramolecular polymer. *Langmuir*, 23:6095–6105, 2007.

[86] J.R. Grigera, S.G. Kalko, and J. Fischbarg. Wall-water interface. a molecular dynamics study. *Langmuir*, 12:154–158, 1996.

[87] J.L. Parker, P.M. Claesson, and P. Attard. Bubbles, cavities, and the long-ranged attraction between hydrophobic surfaces. *Journal of Physical Chemistry*, 98:8468–8480, 1994.

[88] L. Meagher and V.S.J. Craig. Effect of dissolved gas and salt on the hydrophobic force between polypropylene surfaces. *Langmuir*, 10:2736–2742, 1994.

[89] J. Wood and R. Sharma. How long is the long-range hydrophobic attraction? *Langmuir*, 11:4797–4802, 1995.

[90] P. Attard. Bridging bubbles between hydrophobic surfaces. *Langmuir*, 12:1693–1695, 1996.

[91] J. Mahnke, J. Stearnes, R.A. Hayes, D. Fornasiero, and J. Ralston. The influence of dissolved gas on the interactions betwen surfaces of different hydrophobicity in aqueous media. *Physical Chemistry Chemical Physics*, 1:2793–2798, 1999.

[92] A. Carambassis, L.C. Jonker, P. Attard, and M.W. Rutland. Forces measured between hydrophobic surfaces due to a submicroscopic bridging bubble. *Physical Review Letters*, 80(24):5357–5360, 1998.

[93] G.E. Yakubov, H-J. Butt, and O.I. Vinogradova. Interaction forces between hydrophobic surfaces. attractive jump as an indication of formation of "stable" submicrocavities. *Journal of Physical Chemistry B*, 104:3407–3410, 2000.

[94] N. Ishida, M. Sakamoto, M. Miyahara, and K. Higashitani. Attraction between

hydrophobic surfaces with and without gas phase. *Langmuir*, 16:5681–5687, 2000.

[95] P. Attard. Thermodynamic analysis of bridging bubbles and a quantitative comparison with the measured hydrophobic attraction. *Langmuir*, 16:4455–4466, 2000.

[96] P.S. Epstein and M.S. Plesset. On the stability of gas bubbles in liquid-gas solutions. *Journal of Chemical Physics*, 18(11):1505–1509, 1950.

[97] S. Ljunggren and J.C. Eriksson. The lifetime of a colloid-sized gas bubble in water and the cause of the hydrophobic attraction. *Colloids and Surfaces A*, 130:151–155, 1997.

[98] M. Ma and R.M. Hill. Superhydrophobic surfaces. *Current Opinion in Colloid and Interface Science*, 11(4):193–202, 2006.

[99] J.W.G. Tyrrell and P. Attard. Atomic force microscope images of nanobubbles on a hydrophobic surface and corresponding force-separation data. *Langmuir*, 18:160–167, 2002.

[100] S. Lou, J. Gao, X. Xiao, X. Li, G. Li, Y. Zhang, M. Li, J. Sun, X. Li, and J. Hu. Studies of nanobubbles produced at liquid/solid interfaces. *Materials Characterization*, 48:211–214, 2002.

[101] A.C. Simonsen, P.L. Hansen, and B. Klosgen. Nanobubbles give evidence of incomplete wetting at a hydrophobic interface. *Journal of Colloid and Interface Science*, 273:291–299, 2004.

[102] X.H. Zhang, X.D. Zhang, S.T. Lou, Z.X. Zhang, J.L. Sun, and J. Hu. Degassing and temperature effects on the formation of nanobubbles at the mica/water interface. *Langmuir*, 20:3813–3815, 2004.

[103] R.F. Considine, R.A. Hayes, and R.G. Horn. Forces measured between latex spheres in aqueous electrolyte: Non-dlvo behavior and sensitivity to dissolved gas. *Langmuir*, 15:1657–1659, 1999.

[104] O.I. Vinogradova, N.F. Bunkin, N.V. Churaev, O.A. Kisleva, A.V. Lobeyev, and B.W. Ninham. Submicrocavity structure of water between hydrophobic and hydrophilic walls as revealed by optical cavitation. *Journal of Colloid and Interface Science*, 173:443–447, 1995.

[105] C.Y. Lee, J.A. McCammon, and P.J. Rossky. The structure of liquid water at an extended hydrophobic surface. *Journal of Chemical Physics*, 80(9):4448–4455, 1984.

[106] L. Vrbka, M. Mucha, B. Minofar, and P. Jungwirth. Propensity of soft ions for the air/water interface. *Current Opinion in Colloid and Interface Science*, 9:67, 2004.

[107] C. Raduge, V. Pflumio, and Y.R. Shen. Surface vibrational spectroscopy of sulfuric acid-water mixtures at the liquid-vapor interface. *Chemical Physics Letters*, 274(1):140–144, 1997.

[108] S. Baldelli, C. Schnitzer, M. Schultz, and D.J. Campbell. Sum frequency generation investigation of water at the surface of H_2O/H_2SO_4 and H_2O/Cs_2SO_4 binary systems. *Chemical Physics Letters*, 287:143–147, 1998.

CHAPTER 4

TRANSIENT ZETA POTENTIAL MEASUREMENTS IN HYDROPHOBIC, TOPAS MICROFLUIDIC SUBSTRATES

4.1 Abstract

We utilize time-resolved electrokinetic measurements in order to study the electrokinetic properties of silica and TOPAS microfluidic channels as a function of the time history of the fluid–solid interface. In pressure driven flow through TOPAS microchannels, the ζ potential as inferred from streaming potential measurements decays exponentially by a factor of 1.5 with a characteristic decay time of 3 hours after the initial formation of the fluid–solid interface. A similar exponential decay is observed immediately after water is exchanged for ethanol as the solvent in the system. In electroosmotically driven flow through TOPAS microchannels, the ζ potential as inferred through current monitoring experiments was constant in time[1]. No electrokinetic transients were observed in silica microchannels under these flow conditions.

4.2 Introduction

Polymers are increasing in popularity for microfluidics applications because of their low cost, ease of fabrication, and often favorable optical and chemical properties [2–5]. Many polymers are hydrophobic, however, and the material properties of hydrophobic

[0]The content of this chapter was submitted and published as a research article that is reproduced here with permission from *Electrophoresis*. This is the pre-peer reviewed version of the following article: "Transient ζ-Potential Measurements in Hydrophobic, TOPAS Microfluidic Substrates" [1].

[1]We postulate that this difference is due to a more rapid equilibration of the fluid–solid interface owing to the increased transport and shear stress at the wall attendant with electroosmotic flow as compared to pressure-driven flow. This does not represent a breakdown in Onsager reciprocity, but rather a difference in the structure of the fluid–solid interface between the two cases.

polymers relevant to electroosmosis are in dispute; some have reported that electrokinetic actuation in hydrophobic polymers is impossible or unpredictable [6–8], while others have measured significant ζ potentials in hydrophobic substrates [2, 9–14]. The challenge in modeling and measuring electrokinetic phenomena in hydrophobic substrates stems from a poor understanding of the surface chemistry of water–hydrophobe interfaces [14]. The uncertainty in the material properties of hydrophobic substrates limits predictive capabilities for device design, and complexities arising from poorly understood interfacial phenomena can lead to poor repeatability and accuracy of experiments.

Significant scatter is observed in existing electrokinetic data for polymers [13] since these phenomena are difficult to measure and can be very sensitive to surfactants. In general, precise descriptions of electrokinetic phenomena require careful understanding of (i) the origin of interfacial charge, (ii) well-defined fluid velocity boundary conditions, and (iii) models for diffuse and condensed ion distributions [15]. Hydrophobic substrates are particularly challenging because the origin of charge is unknown, and uncertainty regarding slip leads to poorly defined fluid velocity boundary conditions [16, 17]. In addition, molecular dynamics simulations are challenging because of the aqueous solutions involved; long range electrostatic interactions between water molecules limit both the number of simulated molecules as well as the duration of the simulation [18–25].

Some of the complexity in understanding the origin of charge in hydrophobic electrokinetic systems arises from the molecular/supramolecular structure of water at the fluid–solid interface [17]. Postulated structures include regions of reduced or depleted water density [20, 26, 27], ice-like hydrogen bonded water molecule networks [20, 23, 28], and nanobubbles [29]. Depletion layers and water molecule networks im-

pact ion adsorption onto the fluid–solid interface, and are therefore important factors in understanding the origin of charge. Nanobubbles are of particular interest, since their presence would affect both interfacial charge formation and the fluid mechanical boundary condition, and their thermodynamic instability [16, 29–32] could lead to unpredictable or fluctuating electrokinetic behavior in hydrophobic systems. This suggests that electrokinetic properties of hydrophobic systems may depend on the time history of the interface, even though hydrophobic materials are usually chemically inert in aqueous solutions.

In this study, we use time-resolved electrokinetic measurements in order to study the behavior of hydrophobic microfluidic systems as a function of the time history of the interface after initiating (i) pressure driven flow, (ii) electroosmotic flow, and (iii) exchanges between ethanol and water as the solvent in the system. We then compare those results to hydrophilic microfluidic systems. In the past, electrokinetic measurements in hydrophobic systems have been shown to be repeatable and predictable when the fluid–solid interface has reached a sufficient equilibrium [13, 14]. Through time-resolved measurements, we look to determine (a) if the time scale for equilibration differs in hydrophobic and hydrophilic systems, (b) whether the behavior of the system during the approach to equilibrium is erratic or deterministic, and (c) how different flow conditions affect the equilibration time.

4.3 Materials and Methods

4.3.1 Methodology

Here we model electrokinetics by assuming that interfacial phenomena lead to charge separation at fluid–solid interfaces, resulting in a double layer and a charge distribution that can be described by a Gouy–Chapman model [33]. In this context, it is sufficient to treat the ion distribution in the diffuse part of the double layer in the Boltzmann limit, where ions are considered to be point particles experiencing a bulk electrical potential, which has the value ζ at the wall. The electrical potential distribution is then given by the Poisson–Boltzmann equation:

$$\nabla^2\psi = -\frac{\rho_e}{\epsilon} = -\frac{1}{\epsilon}\sum_i C_{o,i} z_i F \exp\left(-\frac{z_i F}{RT}\psi\right) , \tag{2.3}$$

where ψ is the electrical potential, ϵ is the permittivity of the fluid medium, z_i is the valence of the *i*-th ionic species, R is the gas constant, F is Faraday's constant, and $C_{o,i}$ is the concentration (moles/m^3) of the *i*-th species at a location where $\psi = 0$. This ion distribution leads to electroosmosis when subjected to a transverse electric field, and streaming potential when subjected to a pressure driven flow, which we use to study electrokinetics at hydrophobic interfaces. Non dimensionalization of the Poisson–Boltzmann equation leads to a length scale that describes the spatial extent of the double layer, the Debye length.

$$\lambda_D = \sqrt{\frac{\epsilon RT}{2F^2 I}} \tag{2.4}$$

Here I is the ionic strength of the solution in moles/m^3.

In electroosmosis, an external electric field is applied to a fluid in a microchannel with a net unbalanced ion distribution as described by equation 2.3, resulting in bulk flow. If the channel is straight and homogeneous, its dimensions are large as compared to

the Debye length, and there are no pressure gradients, the flow is approximated as being uniform. The bulk flow velocity, u_{EO}, is then given by the Smoluchowski equation,

$$u_{EO} = -\frac{\epsilon\zeta}{\eta}E \,, \tag{2.6}$$

where η is the fluid viscosity, and E is the applied electric field. In Equation 2.6, we assume that fluid properties are uniform, and that the no-slip fluid boundary condition applies precisely at the wall, at which $\psi = \zeta$. In electroosmotic flow, we infer values for the ζ potential from measurements of the electroosmotic velocity, where ζ represents the electrical boundary condition at the fluid–solid interface in the Gouy–Chapman model. The precise physical relationship between the inferred ζ potential and the interfacial charge at the wall is complicated and in dispute [15, 34]. In this paper, we focus on experimental measurements of u_{EO} and do not address double layer models per se.

An imposed pressure-driven flow in a microchannel with an ion distribution described by Equation 2.3 results in the bulk redistribution of unbalanced charges, and the equilibrium condition if there is no net electrical current coincides with an electrical potential called the streaming potential. The streaming potential, $\Delta\phi$, is given by

$$\Delta\phi = \frac{\epsilon\zeta}{\eta\sigma}\Delta P \,, \tag{2.9}$$

where $\Delta P = P_{\text{downstream}} - P_{\text{upstream}}$ is the applied pressure difference, and σ is the bulk fluid conductivity. Equation 2.9 uses the Debye–Hückel approximation, and assumes a thin double layer as compared to the channel radius, so that channel geometry effects are unimportant. Fluid conductivity is assumed to be uniform, and surface conductivity is neglected since the microchannels used in this study are relatively large (the surface area to volume ratio is low). In pressure driven flow, we use streaming potential measurements to infer values for the ζ potential.

In order to compare experiments conducted with solutions of different ionic

strengths, we normalize our ζ-potential data by pC $= -\log C$, where C is the counterion concentration in mol/L, as described in [35].

4.3.2 Chemical Reagents and Capillaries

All reagents were obtained from Sigma–Aldrich (St. Louis, MO). Phosphate buffer solutions were prepared from stock solutions of monobasic and dibasic potassium phosphate. Solution conductivity and pH measurements were conducted using a dual pH/conductivity meter (Mettler Toledo SevenMulti, Columbus, OH) with specialized electrodes (Mettler Toledo Inlab 730 and Inlab 413, Columbus, OH) prior to each experiment, and buffers were checked periodically to ensure that there were no pH or conductivity changes over time. Solution pH was adjusted by titration with hydrochloric acid and/or sodium hydroxide. All buffers were at room temperature (T = 25 °C) for all of our experiments.

Silica and TOPAS were chosen as model hydrophilic and hydrophobic systems for this study, respectively. Silica capillaries were acquired from Polymicro Technologies Inc. (Phoenix, AZ) and TOPAS capillaries were acquired from Paradigm Optics (Vancouver, WA). TOPAS (manufactured by Zeon Chemicals, Louisville, KY) is a cyclo olefin copolymer thermoplastic that has similar properties to Zeonor, but is manufactured with less stringent processes [36]. Both capillaries had outer and inner diameters of 360 μm and 25 μm respectively. A fresh section of capillary was used in each trial of each experiment.

4.3.3 Automated Current Monitoring

An automated current monitoring method was used to measure the ζ potential under electroosmotic flow conditions [37, 38]. For our current monitoring experiments, 250–600V was applied simultaneously across four microchannels 5 cm in length using platinum electrodes and an 8-channel high voltage sequencer (LabSmith HVS448, Livermore, CA). The sequencer was carefully calibrated prior to experiments to ensure consistent readings across channels in both forward and reverse polarity operation. Reservoirs (1.5 mL in volume) at each end of a particular microchannel contained phosphate buffer solutions that varied in conductivity by 7.5%. Control signals were implemented in LabView, where four channels in the sequencer were used to apply voltage, and four were used to monitor the current through the microchannels. Square-wave electric field sequences were applied with periods designed so as to allow electroosmosis to completely displace the fluid within the microchannels during each half cycle. Voltage was controlled via LabView so as to keep the electric field across the microchannels constant during displacement.

The resulting current waveforms (Figure 4.1) were analyzed in one-period segments by taking advantage of the characteristic trapezoidal profile (Figure 4.2). First, we subtracted the mean (I_{mean}) from the waveform ($I(t)$), and then took its absolute value. We then integrated the resulting function over one period, τ, in order to get the area under the curve.

$$A = \int_0^\tau |I(t) - I_{\text{mean}}|\, dt \tag{4.1}$$

The area, A, is simply the area of the two trapezoids in Figure 4.2. The displacement time (the time it takes for the current signal to change from a constant high value to a constant low value and vice versa), Δt, is then related to A as in

$$\Delta t = \tau - \frac{A}{h}\,, \tag{4.2}$$

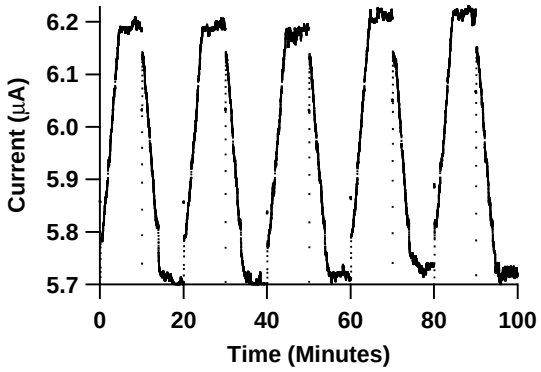

Figure 4.1: Example of a current monitoring raw data trace. For this data, 10 mM, pH 7 phosphate buffer was used in a silica capillary.

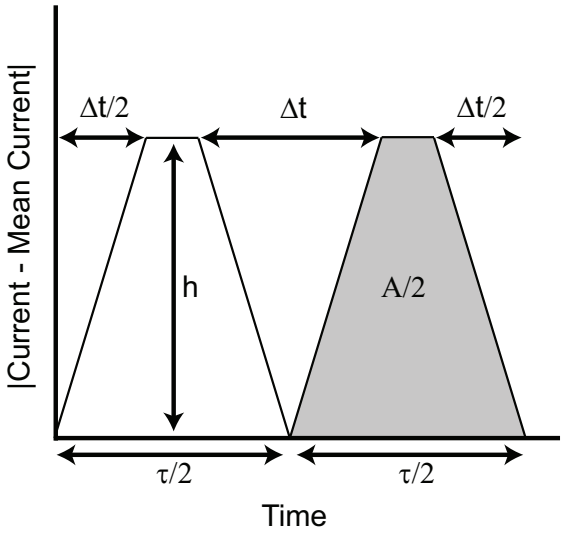

Figure 4.2: Schematic showing how current monitoring data was converted into a velocity measure using a trapezoidal profile.

where h is the height of the trapezoids, or the maximum value of the function ($|I(t) - I_{\text{mean}}|$). Dividing the length of the microchannel, L, by Δt then gives the electroosmotic velocity,

$$u_{EO} = \frac{L}{\Delta t}\,, \tag{4.3}$$

which is converted into a zeta potential value using equation 2.6.

Joule heating was avoided in the system by measuring electroosmotic mobility as a function of electric field magnitude and extrapolating to the zero-field limit. Only fields

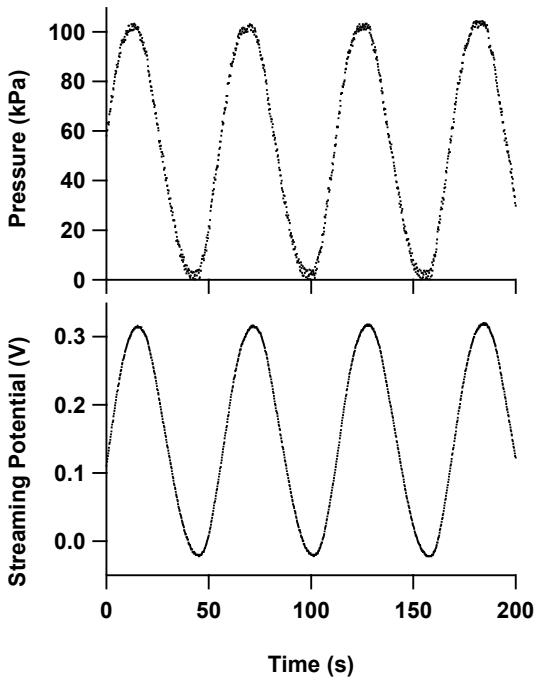

Figure 4.3: Example of raw streaming potential data. For this data, 1 mM, pH 7 phosphate buffer was used in a TOPAS capillary.

that produced mobilities that were within 5% of the zero-field limit were used. Any temperature change due to Joule heating would also result in readily detectable changes in the mean current, and any data in which the mean current varied by more than 10% was not used. Velocity errors due to any pressure imbalances between reservoirs were removed in post processing by averaging the data from the positive and negative half cycles in each period of the square wave input. The ζ potential was calculated from velocity data using the Smoluchowski Equation (Equation 2.6).

4.3.4 Phase-Sensitive Streaming Potential

Phase-sensitive streaming potential experiments were used to measure the ζ potential under pressure driven flow conditions. Pressure (0–103 kPa) was applied to the inlet

of a 5 cm section capillary composed of the material under study using a push/pull syringe pump (KD Scientific, Holliston, MA). Sinusoidal pressure waveforms were established via LabView control of syringe actuation utilizing a PID controller corrected for the pressure dependence of the system's pressure–displacement response. Pressure at the capillary inlet was measured by a strain gauge type transducer (Senso–Metrics SP70D, Simi Valley, CA). PEEK–ULTEM fittings (LabSmith, Livermore, CA) and 360 μm stainless steel tubing were used to make the fluidic connections between the syringe, capillary, electrodes, and pressure transducer [39]. A 10 TΩ electrometer (6514 Electrometer, Keithley, Cleveland, OH) and platinized platinum electrodes were used to measure the generated voltage across the capillary (Figure 4.3). Platinized platinum electrodes were fabricated using an electrochemical reaction as described in [40]. The platinizing solution consisted of 3.5% w/v hydrogen hexachloroplatinate, 0.005% w/v lead acetate, and 2.5% v/v 1M HCl solution. The working platinum electrode was immersed in the platinizing solution against a counter electrode, and a potential of 7 V was applied for 120 s, resulting in a macroscopically black (platinized) platinum electrode. Electrodes were visually inpsected in order to check for degradation prior to each experiment.

Forcing pressures and capillary diameters were chosen such that the flow was laminar in all cases (Reynolds number below 1200), and hydrodynamic starting lengths could be ignored. Streaming potential data that did not correlate with the applied pressure waveform generally corresponded to the presence of an air bubble in the microchannel, and was rejected. The measured pressure and streaming potential waveforms were Fourier processed and the response at the fundamental mode was measured. The ζ potential was then calculated from Equation 2.9 as follows:

$$|\zeta| = \frac{\eta\sigma}{\epsilon}\left(\frac{|\mathcal{F}\{\phi(t)\}|}{|\mathcal{F}\{\Delta P(t)\}|}\right)\Bigg|_{f=f_0}, \tag{4.4}$$

where $\mathcal{F}$ denotes the discrete Fourier transform, and f_o is the frequency of the funda-

mental mode, i.e. the driving frequency of the pressure waveform. Errors due to surface conductivity, non-Debye–Hückel charge distributions, and wall curvature were ignored as they were small as compared to conductivity and temperature uncertainties, which were on the order of 10%. Since Equation 2.9 holds strictly at equilibrium, the period of the applied pressure waveform was chosen to be slow enough (120 s) so as to allow for a quasi-static measurement. If the system is not allowed to reach equilibrium, there will be a phase lag between the streaming potential waveform and the pressure driven waveform. The damping of the streaming potential waveform magnitude that occurs in a system with a phase lag can be corrected for if the phase lag is simultaneously measured:

$$\zeta = \zeta_0 \left(1 + \tan^2 \alpha\right) \ , \tag{4.5}$$

where ζ_0 is the uncorrected ζ potential, and α is the phase difference between the streaming potential and pressure waveforms. The phase lag, however, was negligible in all of our experiments.

4.4 Results

We conducted experiments in both hydrophobic, TOPAS microfluidic channels and hydrophilic, silica microchannels in order to measure their electrokinetic properties as a function of the time history of the fluid–solid interface. In particular, we measured the ζ potential as a function of time (a) in pressure driven flow inferred from streaming potential measurements, (b) in electroosmotic flow inferred from current monitoring experiments, (c) in pressure driven flow after an initial exposure to an electric field, and (d) after exchanging ethanol as the solvent in the system for water.

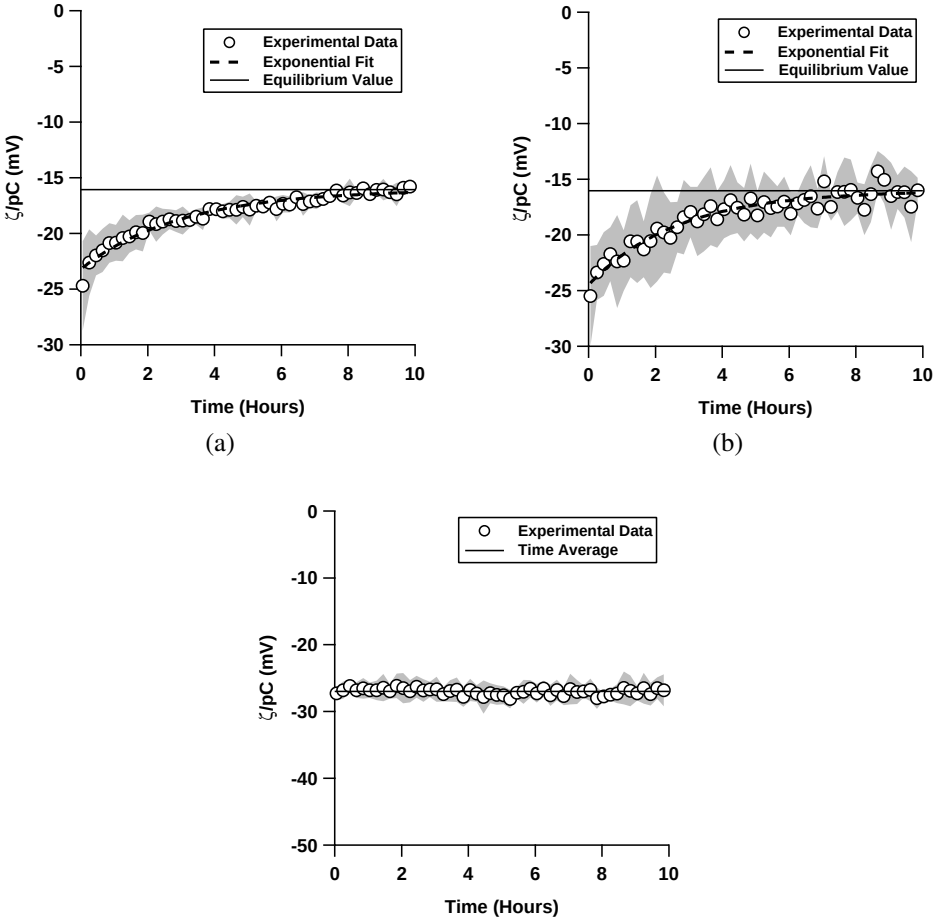

Figure 4.4: Normalized ζ potential, ζ/pC (pC = $-\log C$, C is the counterion concentration in M) inferred from streaming potential measurements in pressure driven flow, as a function of time for (a) a TOPAS microfluidic channel with 1 mM, pH 7 phosphate buffer solution (4 trials), (b) a TOPAS microfluidic channel with 10 mM, pH 7 phosphate buffer solution (6 trials), and (c) in a silica microfluidic channel with 1 mM, pH 7 phosphate buffer solution (4 trials). The inset in (b) shows a comparison of the 1 mM and the 10 mM data for TOPAS. Data shown is an average of the independent trials, where the shaded region represents the standard deviation between the trials.

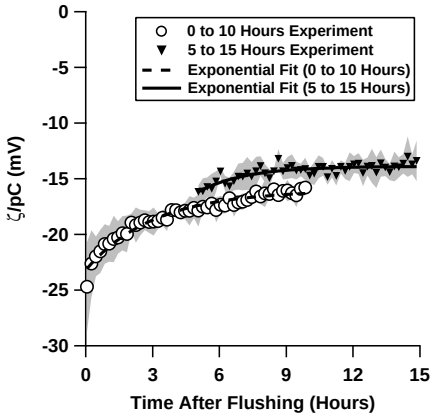

Figure 4.5: Normalized ζ potential, ζ/pC (pC = $-\log C$, C is the counterion concentration in M) in a TOPAS microchannel inferred from streaming potential measurements in pressure driven flow after 5 hours of equilibration (the data was taken from 5 hours to 15 hours after the initial filling of the microchannel). The data is compared to the direct measurement (0 to 10 hours, Figure 4.4a). pH 7, 1 mM phosphate buffer solution was used, and the data shown is an average of 4 independent trials, where the shaded region represents the standard deviation between the trials.

4.4.1 Time-Resolved Electrokinetic Measurements in Pressure Driven Flow

We measured the ζ potential as a function of time after filling with aqueous solution in both hydrophobic (TOPAS) and hydrophilic (silica) microchannels under pressure driven flow, utilizing the phase sensitive streaming potential technique. In both materials, we flushed a pH 7, 1 mM phosphate buffer solution through the microchannels using an applied pressure sinusoidally varying from 0 to 103 kPa (gauge), with a period of 120 s. In TOPAS, we also measured the ζ potential for a 10 mM, pH 7 phosphate buffer solution with the same pressure wave parameters. The resulting sinusoidal streaming potential signals were monitored continuously and recorded with a sampling rate of 5 Hz for 10 hours. The applied pressure and resulting streaming potential waveforms were analyzed in 12 minute segments using Equation 2.9 to give an inferred ζ potential as a function of time.

In the TOPAS microchannels filled with 1 mM phosphate buffer, the normalized ζ potential was initially high in magnitude at -25 mV, but decayed to an equilibrium value of -16.1 mV (Figure 4.4a). The transient is well fit by an exponential decay, with a time constant of 3.0 hours. The normalized ζ potential for 10 mM phosphate buffer in TOPAS had a very similar exponential decay, with an equilibrium value of -16.0 mV and a time constant of 2.7 hours (Figure 4.4b). ζ/pC in the silica microchannels, on the other hand, was constant over the 10 hour period (Figure 4.4c), with a time average of -27.0 mV that varied by less than 3% for the duration.

When the phosphate buffer solution was allowed to equilibrate with the TOPAS microchannels for 5 hours prior to a streaming potential measurement, ζ/pC decayed exponentially from -16.8 mV to -13.9 mV over the next 10 hours, with a time constant of 2.1 hours (Figure 4.5). A comparison of our ζ/pC vs. time data for 0 to 10 hours after flushing with our data for 5 to 15 hours after flushing shows that the two trends are consistent during the overlap period (5 to 10 hours), though the time constants for the exponential decays are slightly different.

4.4.2 Time-Resolved Electrokinetic Measurements in Electroosmotic Flow

We conducted time-resolved measurements of the ζ potential in both hydrophobic TOPAS and hydrophilic silica microchannels under electroosmotic flow using the current monitoring technique. For measurements of the electrokinetic properties of TOPAS, an electric field magnitude of 120 V/cm was applied across the microchannel for a half cycle period of 6 min. For the silica microchannels, an electric field magnitude of 50 V/cm was used with a half cycle period of 10 min. A 10 mM, pH 7 solution of phosphate

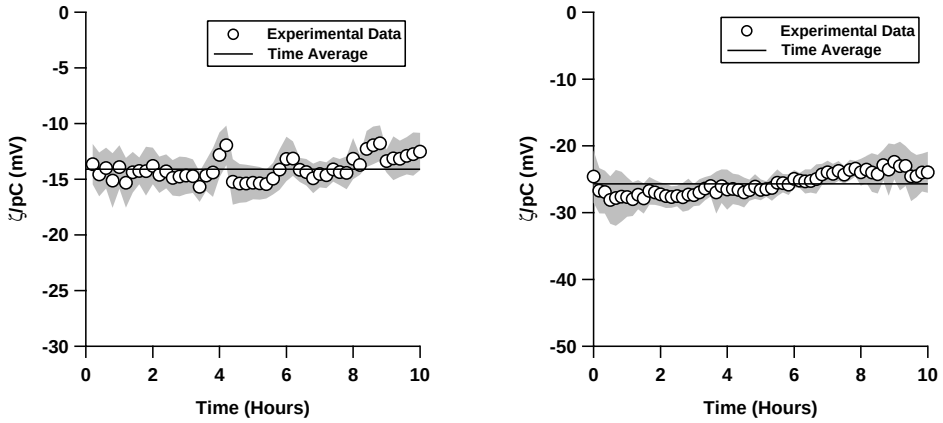

Figure 4.6: Normalized ζ potential, ζ/pC (pC = $-\log C$, C is the counterion concentration in M) in electrokinetically driven flows as inferred via current monitoring in (a) TOPAS and (b) silica microchannels. pH 7, 10 mM phosphate buffer solution was used in both experiments. Data shown is an average of 4 independent trials, where the shaded region represents the standard deviation between the trials.

buffer was used in both the silica and the TOPAS experiments. In contrast to our experiments in pressure driven flow, the ζ potential in both TOPAS and silica was constant and varied by less than 7% over a period of 10 hours (Figure 4.6). The time averaged value of the normalized ζ potential, ζ/pC, for TOPAS was -14.1 mV with a standard deviation of 1.0 mV or 7%. The time average of ζ/pC in silica was -25.7 mV with a standard deviation of 1.6 mV or 6%.

4.4.3 Effect of an Applied Electric Field on Transients in Pressure Driven Flow

In these experiments, we examined the effect of an initially applied electric field in disrupting electrokinetic transients in pressure driven flow. TOPAS microchannels were initially filled with a 1 mM, pH 7 phosphate buffer solution. An electric field of mag-

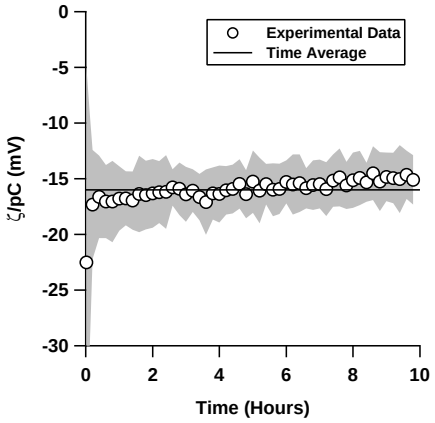

Figure 4.7: Normalized ζ potential as a function of time in a TOPAS microchannel under a pressure driven flow, as inferred via streaming potential. Flow was initially driven through the channel electroosmotically for 12 min. A pH 7 solution with 1 mM phosphate buffer was used. Data shown is an average of 4 independent trials, where the shaded region represents the standard deviation between the trials.

nitude 500 V/cm was then applied across the microchannel for 12 min so as to actuate electroosmotic flow. The electric field magnitude was chosen so that the shear stress at the fluid–solid interface during the initial period of electroosmotic flow would be roughly a factor of 3 larger that in the current monitoring experiments (see Discussion for shear stress calculations). The electric field was then switched off, flow actuated via a sinusoidal pressure waveform, and the streaming potential measured as described in the pressure driven flow experiments from section 4.4.1, using the same experimental parameters.

In contrast to pressure driven flow without an initially applied electric field (Figure 4.4a), the ζ potential remained relatively constant from the time the electric field was switched off over a period of 10 hours (Figure 4.7). The normalized ζ potential decayed from -17.3 mV to -15.1 mV, and had a time average of -15.9 mV, with a standard deviation of 0.8 mV or 5%. The variation is not explained by an exponential decay, as an exponential fit to the data in Figure 4.7 resulted in a non-sensical time constant and a low R^2 value. The data point at t=0 was not used in this analysis, since one of the four

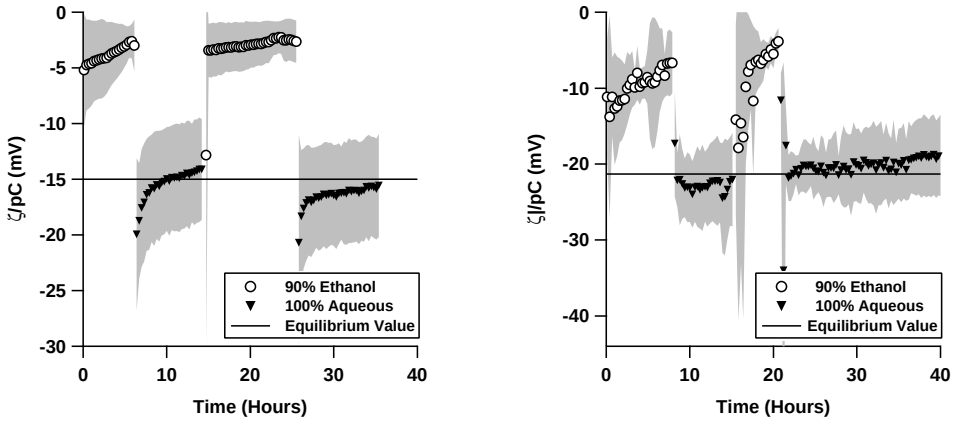

(a) (b)

Figure 4.8: Normalized ζ potential, ζ/pC (pC = $-\log C$, C is the counterion concentration in M) as a function of time in (a) a TOPAS microfluidic channel, and (b) in a silica microfluidic channel. Data shown is an average of 4 independent trials, where the shaded region represents the standard deviation between the trials.

trials for that datum was determined to be a statistical outlier by Chauvenet's criterion.

4.4.4 Solvent Exchange Experiment

Since solvent exchanges have been shown to affect the interfacial properties of water–hydrophobe interfaces [41], we conducted experiments to determine the effects of ethanol–water solvent exchanges on the electrokinetic properties of hydrophobic microfluidic channels.

In each of four trials, a TOPAS microchannel was initially filled with a solution of 90% ethanol and 10% 10 mM, pH 7 phosphate buffer (resulting in an overall counterion concentration of 1 mM). The ethanol solution was then driven through the microchannel via a sinusoidally varying applied pressure, with a peak magnitude of 15 psig, and a period of 120 s. The resulting streaming potential signal was monitored continuously and recorded for a minimum of 6 hours. An aqueous, 1mM, pH 7 phosphate buffer

was then flushed through the microchannel, with flow actuated with the same pressure waveform, and the streaming potential monitored again for a minimum of 6 hours. An additional ethanol cycle and an additional aqueous cycle followed in the same fashion. The applied pressure and resulting streaming potential waveforms were analyzed in 18 minute segments using Equation 2.9 to give an inferred ζ potential as a function of time.

Whenever the aqueous solution replaced the ethanol solution as the solvent, there was an initial transient in which the magnitude of the apparent ζ potential was initially large, with a normalized value of -22 mV (Figure 4.8a). During the first ethanol cycle, the inferred ζ potential changed gradually from -5.2 mV to -3.2 mV, but during the second ethanol cycle, the ζ potential remained relatively constant. As was the case for the initial transients found in pressure driven flow, the ζ-potential magnitude variation during the aqueous cycles is well fit by exponential decays, with a normalized equilibrium value of -14.5 mV and a time constant of 1.5 hours for the first aqueous cycle; -15.8 mV and 3.0 hours for the second aqueous cycle.

We repeated the same experiment in hydrophilic silica microchannels in order to determine whether these transients are unique to hydrophobic systems. Similar transients were not observed during the aqueous cycles in silica microchannels (Figure 4.8b). There is some variation in the inferred ζ potential with time after the exchange from the aqueous solution to the ethanol solution, but in this case the ζ potential gradually changes from the aqueous value to the ethanol value. $|\zeta|/pC$ has a mean value of -22.7 mV during the first aqueous cycle in silica, with a standard deviation of 2.8 mV (13%). During the second aqueous cycle, the mean and standard deviation are -20.0 mV and 2.1 mV (11%).

Table 4.1: Summary of Results. In cases where the ζ potential is considered to be relatively constant in time, the time average with a standard deviation is listed as the equilibrium value. In those cases, exponential fits to the data produced non-sensical (extremely high or low) time constants, and low R^2 values.

	Equilibrium $\frac{\zeta}{pC}$ (mV)	**Time Constant (Hours)**
Pressure Driven Flow		
TOPAS (1 mM PB)	-16.1	3.0
TOPAS (1 mM PB)(After 5 hr Equilibration)	-13.9	2.1
TOPAS (10 mM PB)	-16.0	2.7
Silica (1 mM PB)	-27.0 ± 0.7	–
Electroosmotic Flow		
TOPAS (10 mM PB)	-14.1 ± 1.0	–
Silica (10 mM PB)	-25.7 ± 1.6	–
Pressure Driven Flow after EO		
TOPAS (1 mM PB)	-15.9 ± 0.8	–
After Solvent Exchange		
TOPAS (1 mM PB) – First Aqueous Cycle	-14.5	1.5
TOPAS (1 mM PB) – Second Aqueous Cycle	-15.8	3.0
Silica (1 mM PB) – First Aqueous Cycle	-22.7 ± 1.3	–
Silica (1 mM PB) – Second Aqueous Cycle	-20.0 ± 2.1	–

Table 4.2: Comparison of ζ potential measurements in Silica microchannels at pH 7. Data is temperature corrected to 20° C, as reported in [35].

Measurement Technique	**$\frac{\zeta}{pC}$ (mV)**
This study, Current Monitoring	-25.7
This study, Streaming Potential	-27.0
Dickens et. al [42], Capillary Electrophoresis	-29.0
Scales et. al [43], Streaming Potential	-30.7
Kosmulski et. al [44], Particle Electrophoresis	-32.2
Caslavska et. al [12], Capillary Electrophoresis	-40.4
Schwer et. al [45], Capillary Electrophoresis	-52.2

4.5 Discussion

In general, transients in the inferred ζ potential were only observed in hydrophobic microchannels, and not in hydrophilic microchannels (Table 4.1). Furthermore, no transients were observed if the microchannels were exposed to electroosmotic flow at a field strength of 120 V/cm, even if only for 12 min. If these transients are present in other hydrophobic substrates, they may explain much of the uncertainty in ζ-potential measurements in the literature for polymeric substrates [13], as the time history of the fluid–solid interface is rarely given careful consideration. There is significant disagreement between various ζ-potential measurements for PDMS [38,46–50], polystyrene [11,51,52],

polyethylene [9, 53, 54], PTFE [9, 10, 14, 55–57], and Zeonor [2, 6–8, 14], for example; in particular some have reported that Zeonor has zero electroosmotic mobility [6–8]. Schutzner and Kenndler [9] reported a decrease in the electroosmotic mobility in PTFE capillaries through subsequent experimental measurements, which is consistent with the trends we have observed in TOPAS, though those measurements were made under electroosmotic flow conditions. Our experiments have shown that this decrease over time is likely to be the result of a physical phenomenon at the fluid–solid interface, and not an artifact of the measurement. By explicitly measuring the time dependence of the decay with high resolution, we have shown that the transient behavior is repeatable and predictable, and have quantified the equilibration time to be on the order of hours in TOPAS substrates. In addition to the implications of these results for experimental ζ-potential measurements, this is also important for placing molecular dynamics simulations of water–hydrophobe interfaces in context, as they typically run on very short ($<<$ 1 s) time scales [18–25]. We discuss our observations in each of our specific experiments further in the following sections.

4.5.1 Time-Resolved Electrokinetic Measurements in Pressure Driven Flow

Electrokinetic transients have been studied in the context of pH hysteresis in silica [58], and electroosmotic mobilities have been reported to decrease over time in PTFE microchannels [9]. However, to the authors' knowledge, no explicit measurements of the inferred ζ potential as a function of time with high temporal resolution have been reported. Though the inferred ζ potential in TOPAS varied with time, the equilibrium value for ζ/pC (-16.1 mV) is in good agreement with previously reported results

(-17.4 mV $\pm$ 4.3 mV), where channels were equilibrated with solution for 8 hours before testing [14]. The normalized ζ potential as a function of time was nearly identical for both 1 mM and 10 mM phosphate buffer solutions (See Figure 4.4b, inset), suggesting that the transient does not depend on the solution ionic strength in this range. Furthermore, when we equilibrated the TOPAS microchannels with solution for 5 hours before time-resolved measurements, the results were largely consistent with the assertion that the decay is caused by exposure to solution, not an artifact of the measurement. This suggests that the transient is related to a physical equilibration phenomenon at the fluid–solid interface. Our value for $|\zeta|/pC$ in silica microchannels, -27.0 mV, also agrees with those from experiments found in the literature [35, 42–44], though it is at the low end of the range of reported values (Table 4.2) [35]. The largest values shown in Table 4.2 were generated from capillary electrophoresis experiments, a technique known to at times overestimate the ζ-potential magnitude due to Joule heating errors.

The long time-scale decay observed here in TOPAS microchannels and previously in PTFE microchannels [9] is related to a slow equilibration process at the fluid–solid interface, and this particular form of transient is likely to be unique to hydrophobic surfaces, as similar transients were not observed in silica microchannels. The effects of a slow chemical reaction are not expected to be the cause of this, since TOPAS is chemically inert, and such a reaction is not consistent with our current monitoring data. Unexpected behavior involving impurities in the TOPAS left over from the manufacturing process is unlikely since (a) the observed trends are repeatable and predictable, as evidenced by the low standard deviation across measurements (See Figure 4.4a, shaded region) and agreement with previously published results [14], (b) no reactive impurities were found on similar Zeonor substrates [2], and (c) impurities cannot explain the repeatability of ζ-potential measurements for a given material across substrates fabricated by different manufacturing processes [14]. Stabilization or equilibration of salt ions in the double

layer does not explain the data, as 1 mM and 10 mM phosphate buffer solutions had transients with identical time scales.

Nanobubbles have been observed via AFM to form at water–hydrophobe interfaces [29, 32, 59–62], but not at hydrophilic interfaces [59], and, since they are thermodynamically unstable, they have a lifetime on the order of hours [29–32], which is similar to the time scale of the transients observed in our experiments. The existence of gas at the interface would affect the boundary condition for fluid flow, and introduce apparent slip [16]. Since we infer the ζ potential from macroscopic fluid mechanical electrokinetics experiments, slip, if present, would lead to an inflated apparent ζ potential [17]. Thus nanobubbles are one example of a physical phenomenon at the fluid–solid interface which is unique to hydrophobic surfaces that equilibrates on a similar time scale to our measured electrokinetic transients.

4.5.2 Time-Resolved Electrokinetic Measurements in Electroosmotic Flow

In both the hydrophobic, TOPAS microchannels and the hydrophilic, silica microchannels, the ζ potential was constant over time when flow was driven electroosmotically by electric fields of 120 V/cm and 50 V/cm, respectively. The ζ potential measured for TOPAS in electroosmotic flow matches the equilibrium ζ potential measured from pressure driven flow to within 14%, and with previously published results to within 23% (The standard deviation in that measurement was 25%) [14]. Our value for the ζ potential in silica inferred from electroosmotic flow, -25.7 mV, agrees with our pressure driven flow result to within 5%, and is at the low end of the distribution of data found in the literature (Table 4.2) [35, 42–44].

There are several differences between the electroosmotic flow and the pressure driven flow experiments that may explain the presence of a transient in only the latter case including: (1) possible temperature changes due to Joule heating, (2) differing shear stress at the fluid–solid interface due to the difference in the flow profiles, and (3) the presence of an electric field. Temperature changes due to Joule heating do not explain the transient, as there is no current in the system during a streaming potential experiment, and any current monitoring data in which there was evidence of Joule heating was rejected. The shear stress at the fluid–solid interface was roughly an order of magnitude higher in our electroosmotic flow experiments than it was in our pressure driven flow experiments. The shear in each of the two flow conditions is given by

$$\tau_w = \quad \eta \left(\frac{\partial u}{\partial n} \right)_{wall} = \begin{cases} -\frac{\Delta P}{2\Delta L} R & \text{for pressure driven flow} \\ -\frac{\epsilon \zeta E}{\lambda_D} & \text{for electroosmotic flow,} \end{cases} \tag{4.6}$$

where R is the channel radius, and the electroosmotic shear is an approximation that assumes thin double layers and the Debye–Hückel limit. In our experiments, the average shear stress in pressure driven flow was calculated to be 13 Pa, while in electroosmotic flow, it was 850 Pa. Either the electric field or the increased shear stress at the wall may cause a physical change to the fluid–solid interface that disrupts the transient. If the transient is disrupted by an initial change to the system caused by the application of an electric field and the attendant electroosmotic flow, then it should be possible to disrupt the transient in pressure-driven flow by initially applying an electric field, and then measuring the ζ potential as a function of time via streaming potential. We explored this further in another experiment.

4.5.3 Effect of an Applied Electric Field on Transients in Pressure Driven Flow

The transient observed in our pressure driven flow experiments was disrupted in this case by the initial application of an electric field. The time-averaged ζ potential is in excellent agreement with the equilibrium value from our pressure driven flow experiments, differing by less than 2%. It is also in good agreement with our previously reported results [14], differing by less than 10%. The ζ potential varied by only 5% from the time average over the 10 hours, and in contrast to our simple pressure driven flow experiment, the variation in this case was not well-described by an exponential decay, indicating that it was essentially constant. The solution ionic strength was the same in this experiment as it was in the pressure driven flow experiment (1 mM), so differing solution ionic strengths between experiments does not explain differences in transient electrokinetic behavior. The shear stress during the 12 min of electroosmotic flow, however, was two orders of magnitude larger than it was during the subsequent pressure driven flow. During the time the electric field was applied, the shear stress was calculated from Equation 4.6 to be 2476 Pa. When the electric field was switched off and the flow actuated via pressure, the shear stress was 13 Pa, the same as it was in the pressure driven flow experiments. The constant ζ potential observed in this experiment demonstrates that an initial period of electroosmotic flow disrupts the transient, which is consistent with our hypothesis that exposure to an electric field with the attendant higher shear stress at the wall causes a physical change at the fluid–solid interface that affects the electrokinetic properties of the system. Future experiments with high-shear pressure-driven flow may allow for the shear and electric field effects to be decoupled.

4.5.4 Solvent Exchange Experiment

In this set of experiments, we demonstrated that we can induce transients in the electrokinetic response of a hydrophobic microfluidic channel by replacing ethanol as the solvent in the system for water. Since the solubility of air is higher in ethanol than it is in an aqueous solution [63], replacing ethanol with water is expected to result in the evolution of gas, some of which is trapped at the fluid–solid interface in the form of nanobubbles. The generation of such nanobubbles after ethanol–water solvent exchanges has been demonstrated on OTS–slicon surfaces via tapping mode AFM microscopy [41]. Since the nanobubbles are unstable and impact the chemical and fluid boundary conditions for the system, the solvent exchanges are expected to lead to observable changes in the electrokinetic behavior of microfluidic systems.

During the aqueous cycles of the the solvent exchange experiment in TOPAS, the equilibrium values for $|\zeta|/pC$ (-14.5 mV and -15.8 mV) were essentially the same as those observed in pressure-driven flow with no solvent exchanges (-16.1 mV, see Table 4.1), differing by less than 11% in both cycles. They also match both the nearly constant ζ-potential magnitude observed in electroosmotically driven flow (-14.1 mV), as well as the value from previously published results (-17.4 mV) [14]. As was the case in our pressure-driven flow experiments, the transients during the aqueous cycles here were well-described by exponential decays with time constants on the order of hours. As before, the transients are not likely to have been caused by a slow, reversible chemical reaction with the substrate or with impurities, since TOPAS is non-reactive and the transients were consistent across multiple trials (See Figure 4.8a, where the shaded region indicates variation across trials). Furthermore, the transients were regenerated after a second solvent exchange, discounting the possibility of a permanent chemical modification to the surfaces.

In the silica microchannels, the same transients were not observed during the aqueous cycles. There was some time dependence of the ζ potential when the aqueous solution was exchanged for ethanol, but in this case the ζ potential gradually changed from the aqueous value to the ethanol value, which may be indicative of a period of time in which there was a mixture of both solutions in the microchannel [2]. The high standard deviation immediately following the exchange from the aqueous solution to ethanol (shaded region, Figure 4.8b) also suggests that the fluctuation could be due to experimental error. This is in sharp contrast to the TOPAS microchannel, where upon changing from ethanol to water, the ζ-potential magnitude initially increased by 67% over the equilibrium value, and the standard deviation was nearly constant throughout the aqueous cycle. This large increase cannot be explained by a simple transition period involving a mixture of the two solvents. The constant ζ-potential values measured during the aqueous cycles in silica are in good agreement with data from our other experiments and the data found in the literature (Table 4.2) [35,42–44]. Solvent exchanges led to transients in hydrophobic TOPAS microchannels, while in hydrophilic silica microchannels, they did not.

Given the evidence for nanobubble formation on hydrophobic surfaces after ethanol–water solvent exchanges [41], a similar solvent exchange in our TOPAS microfluidic system is also likely to generate nanobubbles at the fluid–solid interface. The nanobubbles are thermodynamically unstable [16, 29–32, 65] owing to their small size ($\sim$ 10 nm in radius). The Young–Laplace pressure inside a bubble 10 nm in radius is on the order of 144 atm, and as such the bubbles are expected to dissipate nearly instantaneously [14, 16, 65]. On a hydrophilic surface, any nanobubbles that form do indeed

[2] Some ethanol from the previous phase of the experiment remained in the dead volume of the fluidic fixtures upstream from the capillary under study. At the applied flow rates, that volume of solution is estimated to have cleared from the system in about one hour. Water introduced in this phase of the experiment is expected to have mixed with the ethanol rapidly. For the geometry and velocities that were used in this experiment, Taylor dispersion is expected to have resulted in mixing on a time scale of less than 1 second [64].

dissipate instantaneously, as nanobubbles have not been observed on hydrophilic surfaces [59], and we did not observe any electrokinetic transients in hydrophilic, silica microchannels. In a hydrophobic system, on the other hand, nanobubbles have been shown to have longer than expected lifetimes (on the order of hours) [29–32], due to a reduction in total free energy afforded by low surface tension between the gas and the hydrophobic surface. The existence of nanobubbles on the surface introduces a local slip boundary condition due to the presence of a low viscosity gas layer near the surface. In a simple 1D approximation, the slip length, b, is given by

$$b = h\left(\frac{\eta_1}{\eta_2} - 1\right) , \tag{3.4}$$

where h is the height of the nanobubble, η_1 is the viscosity of the liquid phase, and η_2 is the viscosity of the gas phase [16]. For a bubble 10 nm in height, Equation 3.4 gives a slip length of 0.55 μm. Slip leads to an increase in the apparent ζ potential , ζ_a, given by the following expression in the Debye–Hückel, thin double layer limit [17].

$$\zeta_a = \zeta\left(1 + \frac{b}{\lambda_D}\right) \tag{3.5}$$

Equation 3.5 predicts that in a 1mM phosphate buffer solution, slip due to nanobubbles can lead to an apparent ζ potential that is a factor of 57 larger than the actual ζ potential . It should be noted, however, that nanobubbles are not expected to cover the entire surface, and there is recirculating flow within the nanobubbles [16], so Equation 3.4 overestimates the slip length. In this experiment, the ζ potential after solvent exchange was only 1.5 times larger than the equilibrium value. It is expected that nanobubble dissolution over time leads to a reduction in the effective macroscopic slip length, leading to a decay in the apparent ζ potential . Thus, the lifetime of nanobubbles in a hydrophobic, TOPAS microfluidic system after ethanol–water solvent exchanges is expected to coincide with the time scale of our observed electrokinetic transients. Further experiments involving direct observation of nanobubble populations as a function of time with AFM are necessary in order to explore this link further.

4.6 Conclusions

We have demonstrated that the electrokinetic properties of hydrophobic, TOPAS microfluidic substrates depend on the time history of the fluid–solid interface. In flow driven by a 20.2 kPa/cm pressure gradient, there is an initial transient where the inferred ζ potential is initially high in magnitude immediately following formation of the interface, and it ultimately decays to a steady-state value. Such a transient is not present in hydrophilic, silica microchannels. This decay is a function of time elapsed after interface formation and not experimental measurement time. This indicates that the transient is related to a physical phenomenon at the interface, and that the equilibrium is only a function of time, and not the measurement parameters or apparatus. There is no transient in either TOPAS or silica under electroosmotic flow. However, if a TOPAS microchannel is exposed to an initial short period of electroosmotic flow prior to a pressure driven flow, the inferred ζ potential is constant in time. The initial application of an electric field results in a rapid equilibration of the interface, disrupting the transient. Furthermore, we have shown that we can generate similar transients in TOPAS microchannels by replacing ethanol as the solvent in the system with water. A similar solvent exchange does not result in transients in hydrophilic, silica substrates. These transients are also likely caused a physical equilibration phenomenon at the interface, but are not caused by a permanent chemical change, since they can be induced repeatedly by subsequent solvent cycling between water and ethanol. It is also unlikely that slow, reversible chemical reactions can explain these transients, since the TOPAS substrate is chemically inert.

Future work will focus on quantifying the possible link between nanobubbles and macroscopically observable electrokinetic phenomena via AFM, and investigating other methods for generating nanobubbles, such as temperature and pressure cycling.

Understanding these transient phenomena is critical for both electrokinetic characterization of hydrophobic microfluidic substrates, and for the design and operation of microfluidic devices fabricated from hydrophobic substrates. ζ-potential measurements taken when the fluid–solid interface has not reached equilibrium may be inflated and therefore misleading. Furthermore, since many devices rely on solvent cycling, temperature cycling, and changing flow conditions, transient electrokinetic properties induced by fluctuating interfacial conditions may lead to unexpected behavior.

4.7 Acknowledgements

We would like to acknowledge our funding sources: Sandia National Labs (DOE PECASE) and ACS–PRF. We would also like to thank Aditya N. Sharma for useful discussions and his help in developing a correction factor for phase lag in phase-sensitive streaming potential experiments, Wyatt C. Nelson for his help in developing the automated current monitoring techniques, as well as Jonathan Posner (Arizona State) and Blake A. Simmons (Sandia National Labs) for useful discussions.

BIBLIOGRAPHY

[1] V. Tandon, S.K. Bhagavatula, and B.J. Kirby. Transient zeta-potential measurements in hydrophobic, topas microfluidic substrates. *Electrophoresis*, 30:2656–2667, 2009.

[2] P. Mela, A. van den Berg, Y. Fintschenko, E.B. Cummings, B.A. Simmons, and B.J. Kirby. The zeta potential of cyclo-olefin polymer microchannels and its effects on insulative (electrodeless) dielectrophoresis particle trapping devices. *Electrophoresis*, 26:1792–1799, 2005.

[3] H.A. Stone, A.D. Stroock, and A. Ajdari. Engineering flows in small devices: Microfluidics toward a lab-on-a-chip. *Annual Review of Fluid Mechanics*, 36:381–411, 2004.

[4] J.C. McDonald, D.C. Duffy, J.R. Anderson, D.T. Chiu, H. Wu, O.J.A. Schueller, and G.M. Whitesides. Fabrication of microfluidic systems in poly(dimethylsiloxane). *Electrophoresis*, 21:27–40, 2000.

[5] B.G. Hawkins, A.E. Smith, Y.A. Syed, and B.J. Kirby. Continuous-flow particle separation by 3d insulative dielectrophoresis using coherently shaped, dc-biased, ac electric fields. *Analytical Chemistry*, page Accepted, 2007.

[6] J. Gaudioso and H.G. Craighead. Characterizing electroosmotic flow in microfluidic devices. *Journal of Chromatography A*, 971(1):249–253, 2002.

[7] J. Kameoka, H.G. Craighead, H. Zhang, and J. Henion. A polymeric microfluidic chip for ce/ms determination of small molecules. *Analytical Chemistry*, 73:1935–1941, 2001.

[8] A. Tan, S. Benetton, and J.D. Henion. Chip-based solid-phase extraction pretreatment for direct electrospray mass spectrometry analysis using an array of monolithic columns in a polymeric substrate. *Analytical Chemistry*, 75:5504–5511, 2003.

[9] W. Schutzner and E. Kenndler. Electrophoresis in synthetic organic polymer capillaries: Variation of the electroosmotic velocity and zeta potential with ph and solvent composition. *Analytical Chemistry*, 64:1991–1995, 1992.

[10] C. Werner, H. Korber, R. Zimmermann, S. Dukhin, and H. Jacobasch. Extended electrokinetic characterization of flat solid surfaces. *Journal of Colloid and Interface Science*, 208(1):329–346, 1998.

[11] L.E. Locascio, C.E. Perso, and C.S. Lee. Measurement of electroosmotic flow in plastic imprinted microfluid devices and the effect of protein adsorption on flow rate. *Journal of Chromatography A*, 857(1):275–284, 1999.

[12] J. Caslavska and W. Thormann. Electrophoretic separations in pmma capillaries with uniform and discontinuous buffers. *Journal of Microcolumn Separations*, 13(2):69–83, 2001.

[13] B.J. Kirby and E.F. Jr. Hasselbrink. Zeta potential of microfluidic substrates: 2. data for polymers. *Electrophoresis*, 25:203–213, 2004.

[14] V. Tandon, S.K. Bhagavatula, W.C. Nelson, and B.J. Kirby. Zeta potential and electroosmotic mobility in devices fabricated from hydrophobic polymers: 1. the origins of charge. *Electrophoresis*, 29:1092–1101, 2008.

[15] R.J. Hunter. *Zeta Potential in Colloid Science*. Academic Press, London, 1981.

[16] E. Lauga, M.P. Brenner, and H.A. Stone. *Microfluidics: The No-Slip Boundary Condition*. Handbook of Experimental Fluid Dynamics. Springer, New York, 2005.

[17] V. Tandon and B.J. Kirby. Zeta potential and electroosmotic mobility in devices fabricated from hydrophobic polymers: 2. slip and interfacial water structure. *Electrophoresis*, 29:1102–1114, 2008.

[18] C.Y. Lee, J.A. McCammon, and P.J. Rossky. The structure of liquid water at an extended hydrophobic surface. *Journal of Chemical Physics*, 80(9):4448–4455, 1984.

[19] J.R. Grigera, S.G. Kalko, and J. Fischbarg. Wall-water interface. a molecular dynamics study. *Langmuir*, 12:154–158, 1996.

[20] S.I. Mamatkulov, P.K. Khabibullaev, and RR. Netz. Water at hydrophobic substrates: Curvature, pressure, and temperature effects. *Langmuir*, 20:4756–4763, 2004.

[21] L. Joly, C. Ybert, E. Trizac, and L. Bocquet. Hydrodynamics within the electric double layer on slipping surfaces. *Physical Review Letters*, 93:257805, 2004.

[22] L. Vrbka, M. Mucha, B. Minofar, and P. Jungwirth. Propensity of soft ions for the air/water interface. *Current Opinion in Colloid and Interface Science*, 9:67, 2004.

[23] R. Zangi and J.B.F.N. Engberts. Physisorption of hydroxide ions from aqueous solution to a hydrophobic surface. *Journal of the American Chemical Society*, 127:2272–2276, 2005.

[24] D.M. Huang, C. Cottin-Bizonne, C. Ybert, and L. Bocquet. Ion-specific anomalous electrokinetic effects in hydrophobic nanochannels. *Physical Review Letters*, 98:177801, 2007.

[25] D.M. Huang, C. Cottin-Bizonne, C. Ybert, and L. Bocquet. Aqueous electrolytes near hydrophobic surfaces: Dynamic effects of ion specificity and hydrodynamic slilp. *Langmuir*, 24(4):1442–1450, 2007.

[26] A. Poynor, L. Hong, I.K. Robinson, S. Granick, Z. Zhang, and P.A. Fenter. How water meets a hydrophobic surface. *Physical Review Letters*, 97:266101, 2006.

[27] D.A. Doshi, E.B. Watkins, J.N. Israelachvili, and J. Majewski. Reduced water density at hydrophobic surfaces: Effect of dissolved gases. *PNAS*, 102(27):9458–9462, 2005.

[28] L.X. Dang and T. Chang. Molecular mechanism of ion binding to the liquid/vapor interface of water. *Journal of Physical Chemistry B*, 106:235–238, 2002.

[29] P. Attard, M.P. Moody, and J.W.G. Tyrell. Nanobubbles: the big picture. *Physica A*, 314:696–705, 2002.

[30] P. Attard. Electrolytes and the electric double layer. *Advances in Chemical Physics*, 92:1–159, 1996.

[31] P. Attard. Thermodynamic analysis of bridging bubbles and a quantitative comparison with the measured hydrophobic attraction. *Langmuir*, 16:4455–4466, 2000.

[32] P. Attard. Nanobubbles and the hydrophobic attraction. *Advances in Colloid and Interface Science*, 104:75–91, 2003.

[33] R.J. Hunter. *Foundations of Colloid Science, Vol. 2*. Clarendon Press, Oxford, 1989.

[34] J. Lyklema. *Fundamentals of Interface and Colloid Science, Volume II: Solid-Liquid Interfaces*. Academic Press, London, 1995.

[35] B.J. Kirby and E.F. Jr. Hasselbrink. Zeta potential of microfluidic substrates:

1. theory, experimental techniques, and effects on separations. *Electrophoresis*, 25:203–213, 2004.

[36] *http://www.topas.com/topas_brochure_english.pdf*.

[37] X. Huang, M.J. Gordon, and R.N. Zare. Current-monitoring method for measuring the electroosmotic flow rate in capillary zone electrophoresis. *Analytical Chemistry*, 60:1837–1838, 1988.

[38] D. Ross and L.E. Locascio. Effect of caged fluorescent dye on the electroosmotic mobility in microchannels. *Analytical Chemistry*, 75(5):1218–1220, 2003.

[39] B.J. Kirby, D.S. Reichmuth, R.F. Renzi, T.J. Shepodd, and B.J. Wiedenman. Microfluidic routing of aqueous and organic flows at high pressurs: fabrication and characterization of integrated polymer microvalve elements. *Lab on a Chip*, 5:184–190, 2005.

[40] B. Ilic, D. Czaplewski, P. Neuzil, T. Stanczyk, J. Blough, and G.J. Maclay. Preparation and characterization of platinum black electrodes. *Journal of Materials Science*, 38:3447–3457, 2000.

[41] Xue H. Zhang, Nobuo Maeda, and Vincent S.J. Craig. Physical properties of nanobubbles on hydrophobic surfaces in water and aqueous solutions. *Langmuir*, 22:5025–5035, 2006.

[42] J.E. Dickens, J. Gorse, J.A. Everhart, and M. Ryan. Dependence of electroosmotic flow in capillary electrophoresis on group i and ii metal ions. *Journal of Chromatography B*, 657:401–407, 1994.

[43] P.J. Scales, F. Grieser, and T.W. Healy. Electrokinetics of the silica-solution interface: A flat plate streaming potential study. *Langmuir*, 8:965–974, 1992.

[44] M. Kosmulski and E. Matijevic. Zeta potentials of silica in water-alcohol mixtures. *Langmuir*, 8:1060–1064, 1992.

[45] C. Schwer and E. Kenndler. Electrophoresis in fused-silica capillaries: The influence of organic solvents on the electroosmotic velocity and zeta potential. *Analytical Chemistry*, 63(17):1801–1807, 1991.

[46] Y. Liu, J.C. Fanguy, J.M. Bledsoe, and C.S. Henry. Dynamic coating using polyelectrolyte multilayers for chemical control of electroosmotic flow in capillary electrophoresis microchips. *Analytical Chemistry*, 72:5939–5944, 2000.

[47] G. Ocvirk, M. Munroe, T. Tang, R. Oleschuk, K. Westra, and D.J. Harrison. Electrokinetic control of fluid flow in native poly(dimethylsiloxane) capillary electrophoresis devices. *Electrophoresis*, 21:107–115, 2000.

[48] A. Sze, D. Erickson, L. Ren, and D. Li. Zeta-potential measurement using the smoluchowski equation and the slop of the current-time relationship in electroosmotic flow. *Journal of Colloid and Interface Science*, 261:402–410, 2003.

[49] N.A. Lacher, N.F. de Rooij, E. Verpoorte, and S.M. Lunte. Comparison of the performance characteristics of poly(dimethylsiloxane) and pyrex microchip electrophoresis devices for peptide separations. *Journal of Chromatography A*, 1004:225–235, 2003.

[50] M.Y. Badal, M. Wong, N. Chiem, H. Salimi-Moosavi, and D.J. Harrison. Protein separation and surfactant control of electroosmotic flow in poly(dimethylsiloxane)-coated capillaries and microchips. *Journal of Chromatography A*, 947(2):277–286, 2002.

[51] M.A. Roberts, J.S. Rossier, P. Bercier, and H. Girault. Uv laser machined polymer substrates for the development of microdiagnostic systems. *Analytical Chemistry*, 69:2035–2042, 1997.

[52] S.L.R. Barker, M.J. Tarlov, H. Canavan, J.J. Hickman, and L.E. Locascio. Plastic microfluidic devices modified with polyelectrolyte multilayers. *Analytical Chemistry*, 72(20):4899–4903, 2000.

[53] A. Voigt, H. Wolf, S. Lauckner, G. Neumann, R. Becker, and L. Richter. Electrokinetic properties of polymer and glass surfaces in aqueous solutions: Experimental evidence for swollen surface layers. *Biomaterials*, 4(4):299–304, 1983.

[54] F. Bianchi, F. Wagner, P. Hoffmann, and H.H. Girault. Electroosmotic flow in composite microchannels and implications in microcapillary electrophoresis systems. *Analytical Chemistry*, 73:829–836, 2001.

[55] J.C. Reijenga, G.V.A. Aben, T.P.E.M. Verheggen, and F.M. Everaerts. Capillary zone electrophoresis: Effect of physical parameters on separation efficiency and quantitation. *Journal of High Resolution Chromatography*, 8:407–411, 1983.

[56] K.D. Lukacs and J.W. Jorgenson. Capillary zone electrophoresis: Effect of physical parameters on separation efficiency and quantitation. *Journal of High Resolution Chromatography*, 8(8):407–411, 1985.

[57] U. Lappan, H.-M. Buchhammer, and K. Lunkwitz. Surface modification of poly(tetrafluoroethylene) by plasma pretreatment and adsorption of polyelectrolytes. *Polymer*, 40(14):4087–4091, 1999.

[58] T.-L. Huang. On the ph hysteresis of electroosmotic mobility with capillary zone electrophoresis in silica capillary. *Chromatographia*, 35(7/8):395–398, 1993.

[59] N. Ishida, T. Inoue, M. Miyahara, and K. Higashitani. Nano bubbles on a hydrophobic surface in water observed by tapping-mode atomic force microscopy. *Langmuir*, 16:6377–6380, 2000.

[60] S. Lou, J. Gao, X. Xiao, X. Li, G. Li, Y. Zhang, M. Li, J. Sun, X. Li, and J. Hu. Studies of nanobubbles produced at liquid/solid interfaces. *Materials Characterization*, 48:211–214, 2002.

[61] J.W.G. Tyrrell and P. Attard. Images of nanobubbles on hydrophobic surfaces and their interactions. *Physical Review Letters*, 87(17), 2001.

[62] J.W.G. Tyrrell and P. Attard. Atomic force microscope images of nanobubbles on a hydrophobic surface and corresponding force-separation data. *Langmuir*, 18:160–167, 2002.

[63] Kai Fischer and Michael Wilken. Experimental determination of oxygen and nitrogen solubility in organic solvents up to 10 mpa at temperatures between 298 k and 398 k. *J. Chem. Thermodynamics*, 33:1285–1308, 2001.

[64] K.C. Pratt and W.A. Wakeham. The mutual diffusion coefficient of ethanol-water mixtures: Determination by a rapid, new method. *Proceedings of the Royal Society of London A*, 336:393–406, 1974.

[65] S. Ljunggren and J.C. Eriksson. The lifetime of a colloid-sized gas bubble in water and the cause of the hydrophobic attraction. *Colloids and Surfaces A*, 130:151–155, 1997.

CHAPTER 5

ELECTROKINETIC POTENTIAL OF HYDROPHOBIC, ZEONOR MICROFLUIDIC SUBSTRATES IS A FUNCTION OF AMBIENT PRESSURE

5.1 Abstract

Using phase-sensitive streaming potential experiments in a vacuum chamber, we demonstrate that lowering the ambient pressure of the air surrounding a hydrophobic, Zeonor microfluidic substrate results in a decrease in the time scale required for equilibration of the electrokinetic potential. At ambient air pressures below 0.74 atm, the electrokinetic potential changes from $\sim$ -84 mV to $\sim$ -11 mV in 5 h, while the same decrease occurs in a period of over 200 h when the system is at 1 atm. Returning a sub-atmospheric system (where the electrokinetic potential had equilibrated to -11 mV) to atmospheric pressure did not result in any additional change in the electrokinetic potential. This can be described as a type of hysteresis of the electrokinetic potential with dissolved gas concentration. No time or pressure dependence was observed for the electrokinetic potential of hydrophilic (silica) substrates.

5.2 Introduction

Polymers are often used as substrates for microfluidic systems, as they are inexpensive, relatively easy to fabricate, and have potential for favorable biological, chemical, and optical properties [1–4]. Modeling electrokinetics in polymeric substrates is challenging, however, because many of them are hydrophobic, and interfacial phenomena in

[0]The content of this chapter is a draft of a manuscript that may be submitted to Physical Review E.

water–hydrophobe systems are not well understood. While significant electrokinetic potentials have been observed in hydrophobic substrates [1,5–10], some have reported the electrokinetic potential in those substrates to be immeasurable or unpredictable [11–13]. The lack of understanding of water–hydrophobe interfaces [10] limits predictive capabilities for device design, and can lead to inaccurate analytical results.

The complexity of hydrophobic interfaces arises from poorly defined chemical, electrical, and fluid velocity boundary conditions; the origin of charge is unknown, and there is uncertainty regarding slip [14, 15]. Furthermore, these phenomena are dependent on the structure of water and the putative presence of gas at the fluid-solid interface. Regions of depleted water density [16–18], ice-like hydrogen-bonded water molecule networks [16, 19, 20], and nanobubbles [21] have been postulated as interfacial structures. In particular, the presence of interfacial nanobubbles would affect both surface charge and slip, and their thermodynamic instability [14, 21–24] has been proposed as a potential explanation for the variation of electrokinetic properties of hydrophobic substrates as a function of the time history of the fluid-solid interface [25]. Both slip [26] and nanobubbles [27–31] have been shown to depend on the type and amount of gas dissolved in solution. This suggests that the electrokinetic properties of hydrophobic substrates also depend on dissolved gas concentration, which is a function of the ambient pressure and temperature.

Here we use phase-sensitive streaming potential experiments to measure the electrokinetic properties of hydrophobic substrates surrounded by air at sub-atmospheric pressures. Results are compared to measurements at atmospheric pressure, which are carried out to long times (200 h) in order to estimate equilibrium properties. Hydrophilic substrates (silica) are also measured for comparison. Our goal is to determine how the ambient pressure of air in contact with a water–Zeonor system affects both the equilib-

rium electrokinetic potential and the kinetics that govern the approach to equilibrium.

5.3 Reagents and Substrates

Reagents were purchased from Sigma–Aldrich (St. Louis, MO). Phosphate buffer solutions were prepared from stock solutions of monobasic and dibasic potassium phosphate. A mixture of equal parts 0.5 mM monobasic potassium phosphate and 0.5 mM dibasic potassium phosphate was used as the working solution for all experiments ($pH = 7.1$, $pC = -\log C = 2.8$, where C is the molar counterion concentration, consisting of potassium and hydrogen ions in this case). A dual pH/conductivity meter (Mettler Toledo SevenMulti, Columbus, OH) with specialized electrodes (Mettler Toledo Inlab 730 and Inlab 413, Columbus, OH) was used for solution conductivity and pH measurements. Prior to each experiment, buffers were checked to ensure that there were no pH or conductivity changes over time. Solution oxygen content was measured using an electrochemical dissolved oxygen sensor (PASCO PS-2108, Roseville, CA). Oxygen content was used to estimate overall dissolved gas content, relative to the dissolved O_2 concentration at atmospheric pressure (O_2 is about twice as soluble in water at room temperature as N_2 [32], and both gases have nearly the same diffusivity [33, 34]). All buffers were at room temperature (T = 25 °C) for all experiments.

Silica capillaries were purchased from Polymicro Technologies Inc. (Phoenix, AZ) and Zeonor capillaries were purchased from Paradigm Optics (Vancouver, WA). The silica capillaries had outer and inner diameters of 360 μm and 25 μm, while the Zeonor capillaries had outer and inner diameters of 300 μm and 30 μm. A fresh section of capillary was used in each trial of each experiment.

5.4 Streaming Potential Measurements

Phase-sensitive streaming potential experiments were used to measure the electrokinetic potential of silica and Zeonor capillaries as a function of time [10, 25]. Pressure was applied to the inlet of a 4-cm-section capillary composed of the material under study using a push/pull syringe pump (KD Scientific, Holliston, MA). Sinusoidal pressure waveforms with 240-s periods were established via PID control of syringe actuation realized by LabView. Pressure at the capillary inlet was measured by a strain-gauge transducer (Senso-Metrics SP70D, Simi Valley, CA). PEEK-ULTEM fittings (LabSmith, Livermore, CA) and 360-μm stainless steel tubing were used to make the fluid connections between the syringe, capillary, electrodes, and pressure transducer [35].

A 10 TΩ electrometer (6514 Electrometer, Keithley, Cleveland, OH) along with platinized platinum electrodes were used to measure the generated voltage across the capillary. They were fabricated using an electrochemical reaction as described in [36]. The platinizing solution consisted of 3.5% w/v hydrogen hexachloroplatinate, 0.005% w/v lead acetate, and 2.5% v/v 1M HCl solution. The working platinum electrode was immersed in the platinizing solution against a counter electrode, and a potential of 7 V was applied for 120 s, resulting in a macroscopically black (platinized) platinum electrode. Electrodes were visually inpsected in order to check for degradation prior to each experiment.

For experiments at atmospheric pressure, pressure was applied to drive fluid from a syringe through the capillary under test into a reservoir. The pressure waveform ($\Delta P = P_{\text{inlet}} - P_{\text{reservoir}}$) varied from 0 to 27.6 kPa. Sub-atmospheric pressure experiments were conducted inside a vacuum oven (VWR 1430M, Radnor, PA). Pressure was applied by a syringe pump situated outside of the oven, and was transferred

from the syringe pump to a syringe in the oven via a linear positioner (Huntington Mechanical Laboratories L2121-6-A, Grass Valley, CA). Electrical signals were transferred into and out of the experimental vacuum chamber using an electrical feedthrough (Huntington Mechanical Laboratories P-22328-CF, Grass Valley, CA). For these experiments, negative pressure was applied by the syringe pump at the capillary inlet so as to move fluid in the opposite direction as in the experiments at atmospheric pressure. The fluid from a large (20 ml) reservoir that was open to the local atmosphere moved through the capillary under test into a syringe. This ensured that the fluid in the capillary had been exposed to the local atmosphere, allowing for adequate gas transfer between the fluid and the air. In those experiments, the pressure difference between the inlet and the reservoir varied from -41.4 to -13.8 kPa. The flow was laminar in all cases (Reynolds number below 1200), and hydrodynamic starting lengths could be ignored. Electrical signals (i.e. the streaming potential and pressure waveforms) were sampled by a DAQ card at 20 kHz, and averaged over a period of 200 ms.

The measured pressure and streaming potential waveforms were Fourier processed in 12-min segments, and the response at the fundamental mode was used to calculate the electrokinetic potential as a function of time. The electrokinetic potential was calculated from the Smoluchowski Equation as follows:

$$|\zeta| = \frac{\eta\sigma}{\epsilon}\left(\frac{|\mathcal{F}\{\phi(t)\}|}{|\mathcal{F}\{\Delta P(t)\}|}\right)\Bigg|_{f=f_0}, \tag{4.4}$$

where $\mathcal{F}$ denotes the discrete Fourier transform, and f_o is the driving frequency of the pressure waveform. Errors due to surface conductivity, non-Debye-Hückel charge distributions, and wall curvature were ignored as they were small as compared to conductivity and temperature uncertainties, which were of the order of 10%. Because Equation 4.4 holds strictly at equilibrium, the period of the applied pressure waveform was chosen to be slow enough (240 s) to allow for a quasi-static measurement. If the system does not reach equilibrium, there is a phase lag between the streaming-potential waveform and

the pressure waveform. The damping of the streaming potential waveform magnitude that occurs in a system with a phase lag can be corrected for if the phase lag is measured simultaneously:

$$\zeta = \zeta_0 \left(1 + \tan^2 \alpha\right) \ , \tag{4.5}$$

where ζ_0 is the uncorrected electrokinetic potential, and $\alpha = \angle\mathcal{F}(\phi) - \angle\mathcal{F}(\Delta P)$ is the phase difference between the streaming potential and pressure waveforms. The phase lag, however, was negligible in all of our experiments.

In order to compare experiments conducted with solutions of different ionic strengths, we normalize our electrokinetic potential data by $\mathrm{pC} = -\log C$, where C is the counterion concentration in mol/L, as described in [37].

5.5 Results and Discussion

5.5.1 Time dependence of the ζ potential at reduced ambient pressure

We used phase-sensitive streaming potential experiments to measure the electrokinetic potential of Zeonor microchannels as a function of time at ambient pressures of 1 atm, 0.87 atm, 0.74 atm, and 0.47 atm. In these experiments, Zeonor microchannels were filled with aqueous working solution and sealed inside a vacuum-oven chamber. At this point, all of the working solution in the system was at equilibrium with air at atmospheric pressure and room temperature. The pressure was then lowered to the desired value using a mechanical pump, and simultaneous sinusoidal pressure actuation and streaming potential measurement were initiated immediately thereafter. The specified

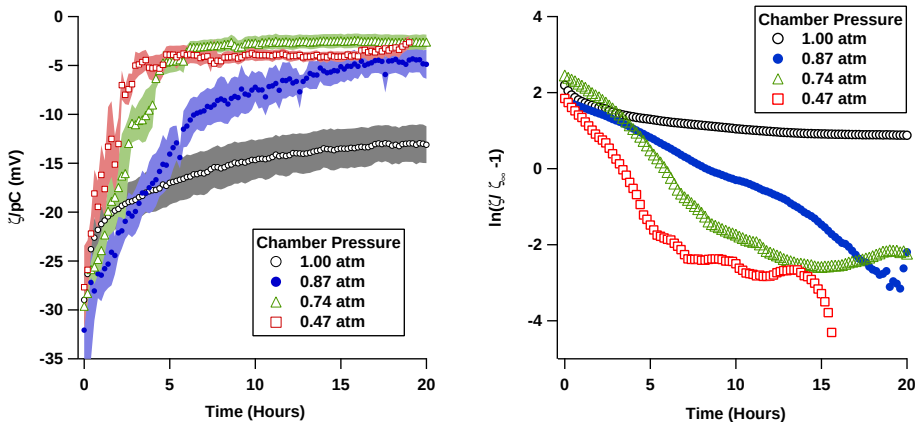

(a) (b)

Figure 5.1: Comparison of ζ-potential measurements in Zeonor at 1 atm to those at lower ambient pressures. (a) Data shown is the electrokinetic potential, ζ, normalized by pC$= -\log C$ (C is the counterion concentration in M) as a function of time for a Zeonor substrate. 1 mM, pH 7 phosphate buffer was the working solution. The experiment was set up with all solutions in equilibrium with air at atmospheric pressure, the pressure was lowered to the indicated values, and the measurement immediately initiated thereafter. All data shown represents the mean of at least 4 replicates, where the shaded areas represent the standard error of the mean. One point from one trial of the 0.74 atm data, and two points from one trial of the 0.47 atm data were determined to be statistical outliers by Chauvenet's criterion, and removed (there were 101 total time points for each replicate of each pressure condition). (b) The same data, plotted as $\ln\left(\frac{\zeta}{\zeta_\infty} - 1\right)$ vs. time, where ζ_∞ is the projected value of ζ at $t = \infty$. A smoothing filter (25-point moving average) was applied to the data prior to plotting for clarity, and points where the logarithm was complex were omitted.

Table 5.1: Summary of Results.

Pressure (atm)	$\frac{\zeta}{pC}$ at $t = 0$ **(mV)**	$\frac{\zeta}{pC}$ at $t = 20$ h **(mV)**
0.47	-27.7	-2.6
0.74	-29.6	-2.6
0.87	-32.1	-4.9
1.00	-28.9	-13.1

sub-atmospheric pressures were maintained throughout the duration of each experiment.

As a test case for a hydrophilic substrate, this experiment was also run for silica in air at 0.47 atm.

Table 5.2: Comparison of electrokinetic-potential measurements for Zeonor from different studies. In [10], the reported data was taken after the solution and Zeonor substrate equilibrated for 4 h, so our data at t = 4 h is shown for comparison.

	Experiment	$\frac{\zeta}{pC}$ **(mV)**
Tandon, et al. [10]	Current Monitoring	-23.8
Tandon, et al. [10]	Streaming Potential	-20.7
This study	Streaming Potential (at t = 4 h)	-17.8

At all pressures, the normalized electrokinetic potential in Zeonor was initially large in magnitude at ~ -30 mV, but decayed to a smaller magnitude over time (Fig. 5.1a). The temporal variations in the electrokinetic potential can be described as exponential decays with one or more time constants (Figure 5.1b; this is discussed further in the next section). At the end of the 20 hour period in which the experiments were run, the electrokinetic potential was smaller in magnitude at lower ambient pressures (Table 5.1). This suggests that pressure affects the equilibrium state of the electrokinetic potential and/or the kinetics of the approach toward equilibrium. This change was not caused by an increase in solution conductivity due to evaporation, as the conductivity increased by less than 3% in all experiments. The data at 0.47, 0.74, and 0.87 atm all decay to the same ζ potential at the end of the 20-h period, though it is not clear from this experiment whether the system at 1 atm would have reached the same electrokinetic potential at times greater than 20 h (see next section). For these experimental conditions, the pressure dependence is weaker below 0.47 atm, as the electrokinetic-potential traces for 0.74 atm and 0.47 atm were nearly identical.

The measured electrokinetic potential as a function of time for Zeonor at atmospheric pressure agrees well with previously reported results for TOPAS [25], a thermoplastic that is chemically similar to Zeonor, but is manufactured with less stringent processes. While the effects of incubating Zeonor with aqueous solutions over long time periods on the electrokinetic potential have been investigated [1], to the authors'

knowledge, no previous results for the temporal dependence of the electrokinetic potential of Zeonor with high temporal resolution (12 min) have been reported. In Table 5.2, several reported values for the (phenomenologically defined) equilibrium electrokinetic potential of Zeonor are shown to be in good agreement. Meaningful comparison is challenging, however, since equilibrium is defined differently in each of the experiments.

The electrokinetic potential of silica did not show any pressure or time dependence, with a normalized time-averaged value of -25.8 mV in air at 0.47 atm (the normalized standard deviation of the time-average was 3%, suggesting that the electrokinetic potential was constant). This agrees well with our measured value at 1 atm (-27.8 mV), and with previously published results [25, 38–40].

We have previously postulated that the time dependence of the electrokinetic potential in hydrophobic substrates may be related to the nucleation and dissipation of nanobubbles at the fluid-solid interface [25]. Nanobubbles are gas bubbles of diameter on the order of 50–200 nm, which form at hydrophobic interfaces, and are classically predicted by the Young–Laplace equation to be highly unstable. They have been observed via AFM to form at water–hydrophobe interfaces [21, 24, 29, 41–43], but not at hydrophilic interfaces [29], and, since they are thermodynamically unstable, they have a lifetime on the order of hours [21–24]. The presence of gas at the interface changes the fluid velocity boundary condition, and introduces an apparent slip [14]. For a given interfacial potential, ψ_0, slip leads to an increase in the electrokinetic potential , ζ, which can be estimated using the following expression in the Debye-Hückel, thin double layer limit [15].

$$\zeta = \psi_0 \left(1 + \frac{b}{\lambda_D}\right) \tag{5.1}$$

Here, ζ is the measured electrokinetic potential, ψ_0 is the interfacial potential, b is the Navier slip length, and λ_D is the Debye length. Experiments [44] and MD simulations

[45, 46] have demonstrated the significance of slip in electrokinetic systems, though the phenomena is not well-understood, and the effects of surface roughness and non-uniform surface conduction within thin double layers have been shown to be important, setting a limit to the effect of slip [47, 48]. Since nanobubbles are unstable, their decay over time is expected to result in the reduction of the apparent electrokinetic potential.

While the origin of slip on hydrophobic substrates is unclear [14], slip has been shown to be modulated by the type of dissolved gas in solution [26]. In addition, the state of dissolved gases has been observed to affect the density of water near the fluid-solid interface [18]. Nanobubble thermodynamic stability is also expected to depend on the concentration of dissolved gas in the fluid [21, 49], which depends on the pressure of gas in equilibrium with the fluid, as given by Henry's law.

$$P = k_H C \tag{5.2}$$

Here, C is the concentration of dissolved gas, k_H is the Henry coefficient for the particular fluid-gas system at a given temperature, and P is the partial pressure of the gas in equilibrium with the fluid. The dependence of electrokinetic potential equilibration kinetics on the ambient atmospheric pressure observed in this study is consistent with nanobubbles as a mechanism for introducing apparent slip, leading to an inflated electrokinetic potential. Reduced ambient pressure results in a lower dissolved gas concentration, faster dissolution of nanobubbles, and a more rapid approach to the equilibrium electrokinetic potential.

5.5.2 Very-long-term behavior of ζ at atmospheric pressure

In order to better establish the equilbrium electrokinetic potential for the Zeonor–water interface in air at 1 atm, we conducted a long-term (200 h), phase-sensitive stream-

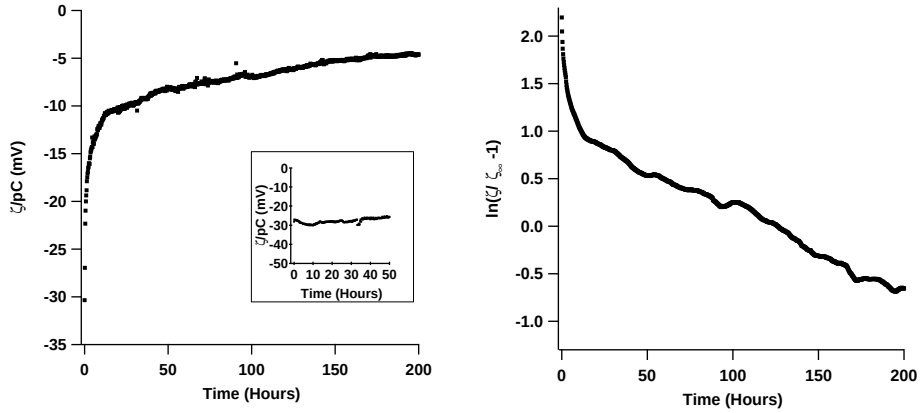

(a) (b)

Figure 5.2: (a) ζ-potential measurement in Zeonor at 1 atm over a time period of 200 hours. The Zeonor data shown is an average of two replicates. The inset shows the electrokinetic potential in silica over a time period of 50 hours for comparison. Data shown is ζ normalized by pC$= -\log C$ (C is the counterion concentration in M) as a function of time for a Zeonor substrate. 1 mM, pH 7 phosphate buffer was the working solution. (b) The same data, plotted as $\ln\left(\frac{\zeta}{\zeta_\infty} - 1\right)$ vs. time, where ζ_∞ is the projected value of ζ at $t = \infty$.

Table 5.3: The sub-atmospheric data sets in Figure 5.1a, and the data in Figure 5.2a were fit to double exponential functions($\zeta = \zeta_\infty + \zeta_1 e^{-t/\tau_1} + \zeta_2 e^{-t/\tau_2}$, where ζ_1 and ζ_2 are fit parameters, τ_1 and τ_2 are the time constants, and ζ_∞ is the value of ζ at $t = \infty$), using a non-linear least-squares optimization. All fits had an R^2 value greater than 0.99.

Pressure (atm)	ζ_∞/pC **(mV)**	τ_1 **(h)**	τ_2 **(h)**
1.00	-3.0	115.21	2.85
0.87	-4.4	4.23	1.91
0.74	-2.5	1.48	1.26
0.47	-3.8	1.99	1.96

ing potential experiment (Fig. 5.2). As was the case with the 20 h experiment, the magnitude of the normalized electrokinetic potential was initially large at ~ -30 mV. The electrokinetic potential continued to decrease beyond the value observed at 20 h, however, to -4.62 mV after 200 h. In comparison, the electrokinetic potential of the silica–water interface was constant over 50 h, with a normalized, time-averaged value of -27.8 mV and a normalized standard deviation of 4%.

The temporal dependence of the electrokinetic potential at atmospheric pressure is characterized by an exponential decay with two time constants, one long and one short (Figure 5.2b). The data in Figure 5.1 was fit to exponential functions in order to determine the dependence of these time constants on ambient pressure (Table 5.3). As the ambient pressure is decreased, the long time constant decreases dramatically, while the short time constant is affected less (The 0.74 and 0.47 atm cases were nearly the same). In all cases, the electrokinetic potential approached nearly the same value at $t = \infty$ ($\zeta_\infty/pC \sim -3$ mV). For the 0.47 and 0.74 atm cases, the long and short time constants are very similar to each other, indicating that those data may be well-described by an exponential decay with a single time constant.

The steady state is independent of pressure, but pressure regulates the kinetics of the approach to steady-state. This suggests that lower ambient pressure results in a more rapid approach to steady-state, rather than a change in the equilibrium electrokinetic potential. To the authors' knowledge, no previous data on the electrokinetic potential of Zeonor substrates after long-term equilibration with aqueous solution has been published. Mela et. al [1] showed that incubating a Zeonor substrate with phosphate buffer solution for 10 days, and then flushing with new solution, resulted in a slight increase in the electrokinetic potential. This is consistent with our observations, as flushing would likely expose Zeonor microchannels to air, resulting in a temporary increase in the electrokinetic potential.

5.5.3 Electrokinetic-potential hysteresis with dissolved gas concentration

Given the postulated role of nanobubbles in electrokinetic potentials of hydrophobic substrates, we expect that the observed pressure dependence of the electrokinetic potential of the Zeonor–water system is fundamentally due to the state of dissolved gases in solution. When the ambient pressure is decreased, a finite amount of time is required for the solution to come to equilibrium with the surrounding gas (Fig. 5.3). Using the data in Fig. 5.3 and a model for gas transfer kinetics, we calculated the dissolved O_2 concentration in the working solution as a function of time in each of our low-pressure experiments. The electrokinetic potential as a function of dissolved O_2 concentration is nearly the same for all of the sub-atmospheric pressures examined (Fig. 5.4). It decreases in magnitude approximately linearly with dissolved O_2 concentration until the normalized (with respect to the equilibrium concentration at 1 atm air pressure) concentration is ~ 0.9, at which point ζ is constant with further decrease in the O_2 content.

The collapse of data taken at different sub-atmospheric pressures shown in Fig. 5.4 suggests that the response of ζ to changes in dissolved gas content is relatively rapid as compared to the natural equilibration time of the electrokinetic potential seen at atmospheric pressure. Thus, the timescales of the electrokinetic-potential decay associated with the sub-atmospheric pressures in Fig. 5.1 are expected to be more representative of the equilibration time of dissolved gas in the system. The faster approach to equilibrium seen at lower pressures is due to the faster decrease in dissolved gas content.

We also investigated whether the altered time dependence of the electrokinetic potential of the Zeonor–water interface at low ambient pressures is reversible by starting a phase-sensitive streaming potential experiment at low (0.47 atm) pressure, and then

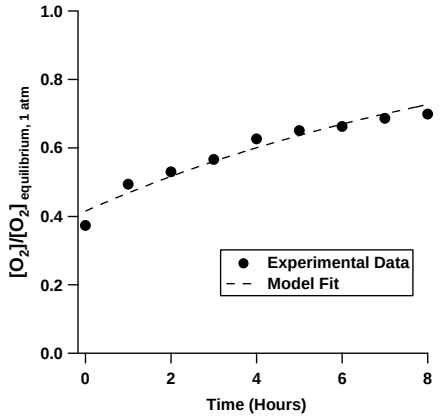

Figure 5.3: Dissolved O_2 content in pH7, 1 mM phosphate buffer as a function of time. The solution was first allowed to equilibrate at low pressure (0.47 atm) for 20 h. It was then removed from vacuum (returned to 1 atm ambient pressure), and the dissolved O_2 concentration was measured as a function of time. Data was fit to a model for oxygen transfer between air and solution based on first order kinetics, assuming a well-stirred solution in contact with an infinite reservoir of air, and equilibrium conditions defined by Henry's Law. The time constant for O_2 entering solution was calculated from the fit to be 10.5 h. Data shown is normalized by the dissolved O_2 content of a solution in equilibrium with air at 1 atm.

increasing the pressure to 1 atm after 5 h (Fig. 5.5). At the start of the experiment, the working solution was at equilibrium with air at atmospheric pressure, the pressure in the experimental chamber was lowered, and the streaming potential experiment was initiated immediately thereafter. The electrokinetic potential as a function of time is very similar to that seen in Fig. 5.1 for 0.47 atm, and the return to 1 atm pressure did not have an observable effect on the electrokinetic potential, as it remained constant across the changeover at 5 h. This, combined with the long-term experiment, suggests that the equilibrium electrokinetic potential is not a function of pressure in the observed range, though pressure affects the kinetics of equilibration.

Examination of the electrokinetic potential data in Fig. 5.5 as a function of dissolved O_2 content reveals a type of hysteresis (Fig. 5.6). When the ambient pressure is 0.47 atm, the electrokinetic potential magnitude decreases with decreasing solution O_2 concentration until it reaches the equilibrium value, as was the case in all of the

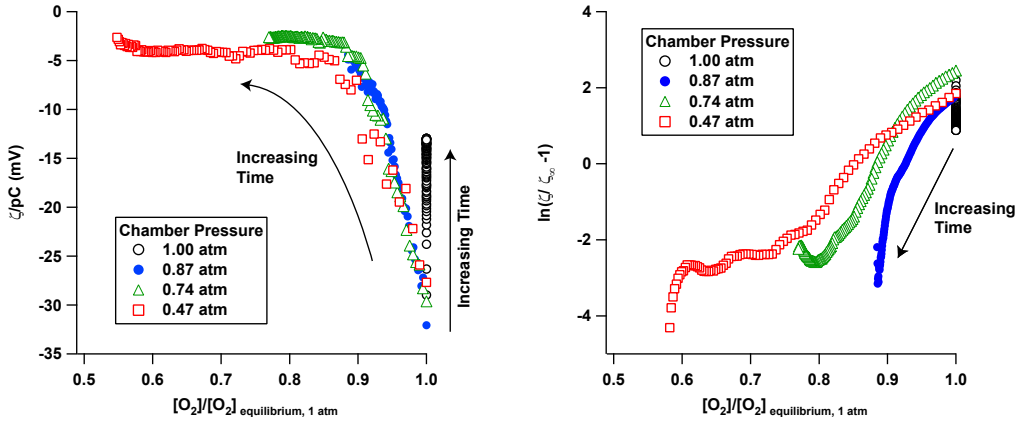

(a) (b)

Figure 5.4: (a) The electrokinetic potential, ζ, normalized by pC$= -\log C$ (C is the counterion concentration in M) as a function of dissolved O_2 concentration for several ambient pressures. Dissolved O_2 concentration as a function of time was calculated using the model and data described in Fig. 5.3. The points are evenly spaced in time, at 12 min intervals. Dissolved O_2 concentration is normalized by the dissolved O_2 content of a solution in equilibrium with air at 1 atm. (b) The same data, plotted as $\ln\left(\frac{\zeta}{\zeta_\infty} - 1\right)$ vs. time, where ζ_∞ is the projected value of ζ at $t = \infty$. A smoothing filter (25-point moving average) was applied to the data prior to plotting for clarity, and points where the logarithm was complex were omitted.

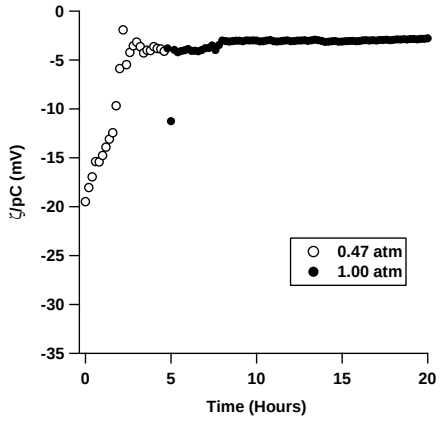

Figure 5.5: The electrokinetic potential, ζ, normalized by pC$= -\log C$ (C is the counterion concentration in M) as a function of time for a Zeonor substrate. 1 mM, pH 7 phosphate buffer was the working solution. The experiment was initiated at 0.47 atm ambient pressure, and the pressure was raised to 1 atm after 5 hours.

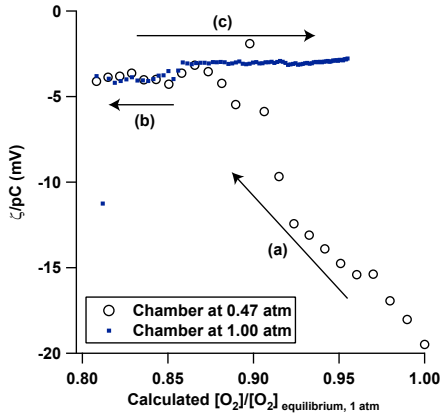

Figure 5.6: The electrokinetic potential of a Zeonor substrate exhibits a type of hysteresis with changing dissolved gas conditions. The ζ/pC data from Fig. 5.5 is shown here as a function of dissolved O_2 concentration. The points are evenly spaced in time, at 12 min intervals. Dissolved O_2 concentration as a function of time was calculated using the model and data described in Fig. 5.3. (a) A solution that was in equilibrium with air at 1 atm is suddenly exposed to air at 0.47 atm. ζ/pC decreases in magnitude as the dissolved O_2 concentration decreases. (b) ζ/pC has stopped decreasing in magnitude, but the dissolved O_2 concentration continues to decrease. (c) The air in the chamber is returned to a pressure of 1 atm. The dissolved O_2 concentration increases, but ζ/pC does not change.

sub-atmospheric experiments. Returning the ambient pressure to 1 atm results in the O_2 concentration increasing towards its original value. The electrokinetic potential magnitude, however, does not increase back to its original value, but rather remains constant with the increasing gas concentration.

Though the electrokinetic potential magnitude decreased with decreasing solution gas content, it stopped decreasing at a particular solution gas concentration. This is consistent with unstable nanobubbles that nucleate at the water-Zeonor interface upon replacing air in the capillary with aqueous solution, and that dissipate at a rate that depends on the amount of dissolved gas in solution. Once the electrokinetic potential has reached equilibrium (i.e. the nanobubbles have dissipated), increasing the ambient atmospheric pressure back to 1 atm may stabilize existing nanobubbles, but it is not expected to result in the formation of new ones. The air content in solution at most

reaches the same value it was at the start, which is not sufficient to stabilize nanobubbles [21].

5.6 Conclusions

We have demonstrated that the kinetics governing equilibration of the electrokinetic potential of Zeonor microfluidic substrates are dependent on the ambient air pressure. Upon initial formation of the fluid-solid interface, Zeonor substrates have a electrokinetic potential that is initially high in magnitude that ultimately decays to a steady-state value. Across ambient air pressures ranging from 0.47 atm to 1 atm, the normalized electrokinetic potential tends to the same equilibrium value (-5 to -3 mV). The approach to equilibrium, however, is faster at lower ambient air pressures. In silica substrates, the electrokinetic potential does not change with time, or with ambient pressure. Once the electrokinetic potential has reduced in magnitude, increasing the ambient air pressure does not increase it again, suggesting hysteresis of the electrokinetic potential with solution dissolved gas content.

For hydrophobic substrates, in addition to pH, conductivity, temperature, etc., the electrokinetic potential must also be considered as a function of the history of the solution dissolved gas concentration. While the dependence of the electrokinetic potential on ambient pressure and ethanol–water solvent exchanges [25] suggest that the amount of dissolved gas in solution affects the electrokinetic potential, future work will involve investigating different types of dissolved gases. Carbon dioxide, for example, has anomalously high solubility owing to its ability to form hydrogen bonds with water, and it can react to form carbonic acid [50–52]. In addition, direct observation of nanobubble dynamics using AFM will help strengthen the putative link between nanobubbles and

macroscopically observable electrokinetic phenomena.

Understanding the effect of the state of dissolved gases on electrokinetics impacts characterization of surface charge and slip at hydrophobic interfaces, as well as design and optimization of microfluidic devices fabricated from hydrophobic polymers. Since pressure, temperature, and solution components can all affect gas solubility, heat, flow, and solvent cycling may lead to unexpected variations in device performance.

5.7 Acknowledgements

We would like to acknowledge our funding sources: Sandia National Labs (DOE PECASE) and ACS-PRF. We would also like to thank Sharath K. Bhagavatula for his help in developing the phase-sensitive streaming potential techniques, as well as Abraham D. Stroock (School of Chemical and Biomolecular Engineering, Cornell University) Blake A. Simmons (Sandia National Labs) for useful discussions.

BIBLIOGRAPHY

[1] P. Mela, A. van den Berg, Y. Fintschenko, E.B. Cummings, B.A. Simmons, and B.J. Kirby. The zeta potential of cyclo-olefin polymer microchannels and its effects on insulative (electrodeless) dielectrophoresis particle trapping devices. *Electrophoresis*, 26:1792–1799, 2005.

[2] H.A. Stone, A.D. Stroock, and A. Ajdari. Engineering flows in small devices: Microfluidics toward a lab-on-a-chip. *Annual Review of Fluid Mechanics*, 36:381–411, 2004.

[3] J.C. McDonald, D.C. Duffy, J.R. Anderson, D.T. Chiu, H. Wu, O.J.A. Schueller, and G.M. Whitesides. Fabrication of microfluidic systems in poly(dimethylsiloxane). *Electrophoresis*, 21:27–40, 2000.

[4] B.G. Hawkins, A.E. Smith, Y.A. Syed, and B.J. Kirby. Continuous-flow particle separation by 3d insulative dielectrophoresis using coherently shaped, dc-biased, ac electric fields. *Analytical Chemistry*, page Accepted, 2007.

[5] W. Schutzner and E. Kenndler. Electrophoresis in synthetic organic polymer capillaries: Variation of the electroosmotic velocity and zeta potential with ph and solvent composition. *Analytical Chemistry*, 64:1991–1995, 1992.

[6] C. Werner, H. Korber, R. Zimmermann, S. Dukhin, and H. Jacobasch. Extended electrokinetic characterization of flat solid surfaces. *Journal of Colloid and Interface Science*, 208(1):329–346, 1998.

[7] L.E. Locascio, C.E. Perso, and C.S. Lee. Measurement of electroosmotic flow in plastic imprinted microfluid devices and the effect of protein adsorption on flow rate. *Journal of Chromatography A*, 857(1):275–284, 1999.

[8] J. Caslavska and W. Thormann. Electrophoretic separations in pmma capillaries with uniform and discontinuous buffers. *Journal of Microcolumn Separations*, 13(2):69–83, 2001.

[9] B.J. Kirby and E.F. Jr. Hasselbrink. Zeta potential of microfluidic substrates: 2. data for polymers. *Electrophoresis*, 25:203–213, 2004.

[10] V. Tandon, S.K. Bhagavatula, W.C. Nelson, and B.J. Kirby. Zeta potential and electroosmotic mobility in devices fabricated from hydrophobic polymers: 1. the origins of charge. *Electrophoresis*, 29:1092–1101, 2008.

[11] J. Gaudioso and H.G. Craighead. Characterizing electroosmotic flow in microfluidic devices. *Journal of Chromatography A*, 971(1):249–253, 2002.

[12] J. Kameoka, H.G. Craighead, H. Zhang, and J. Henion. A polymeric microfluidic chip for ce/ms determination of small molecules. *Analytical Chemistry*, 73:1935–1941, 2001.

[13] A. Tan, S. Benetton, and J.D. Henion. Chip-based solid-phase extraction pretreatment for direct electrospray mass spectrometry analysis using an array of monolithic columns in a polymeric substrate. *Analytical Chemistry*, 75:5504–5511, 2003.

[14] E. Lauga, M.P. Brenner, and H.A. Stone. *Microfluidics: The No-Slip Boundary Condition*. Handbook of Experimental Fluid Dynamics. Springer, New York, 2005.

[15] V. Tandon and B.J. Kirby. Zeta potential and electroosmotic mobility in devices fabricated from hydrophobic polymers: 2. slip and interfacial water structure. *Electrophoresis*, 29:1102–1114, 2008.

[16] S.I. Mamatkulov, P.K. Khabibullaev, and RR. Netz. Water at hydrophobic substrates: Curvature, pressure, and temperature effects. *Langmuir*, 20:4756–4763, 2004.

[17] A. Poynor, L. Hong, I.K. Robinson, S. Granick, Z. Zhang, and P.A. Fenter. How water meets a hydrophobic surface. *Physical Review Letters*, 97:266101, 2006.

[18] D.A. Doshi, E.B. Watkins, J.N. Israelachvili, and J. Majewski. Reduced water density at hydrophobic surfaces: Effect of dissolved gases. *PNAS*, 102(27):9458–9462, 2005.

[19] L.X. Dang and T. Chang. Molecular mechanism of ion binding to the liquid/vapor interface of water. *Journal of Physical Chemistry B*, 106:235–238, 2002.

[20] R. Zangi and J.B.F.N. Engberts. Physisorption of hydroxide ions from aqueous solution to a hydrophobic surface. *Journal of the American Chemical Society*, 127:2272–2276, 2005.

[21] P. Attard, M.P. Moody, and J.W.G. Tyrell. Nanobubbles: the big picture. *Physica A*, 314:696–705, 2002.

[22] P. Attard. Electrolytes and the electric double layer. *Advances in Chemical Physics*, 92:1–159, 1996.

[23] P. Attard. Thermodynamic analysis of bridging bubbles and a quantitative comparison with the measured hydrophobic attraction. *Langmuir*, 16:4455–4466, 2000.

[24] P. Attard. Nanobubbles and the hydrophobic attraction. *Advances in Colloid and Interface Science*, 104:75–91, 2003.

[25] V. Tandon, S.K. Bhagavatula, and B.J. Kirby. Transient zeta-potential measurements in hydrophobic, topas microfluidic substrates. *Electrophoresis*, 30:2656–2667, 2009.

[26] S. Granick, Y. Zhu, and H. Lee. Slippery questions about complex fluids flowing past solids. *Nature Materials*, 2(4):221–227, 2003.

[27] L. Meagher and V.S.J. Craig. Effect of dissolved gas and salt on the hydrophobic force between polypropylene surfaces. *Langmuir*, 10:2736–2742, 1994.

[28] J. Mahnke, J. Stearnes, R.A. Hayes, D. Fornasiero, and J. Ralston. The influence of dissolved gas on the interactions betwen surfaces of different hydrophobicity in aqueous media. *Physical Chemistry Chemical Physics*, 1:2793–2798, 1999.

[29] N. Ishida, T. Inoue, M. Miyahara, and K. Higashitani. Nano bubbles on a hydrophobic surface in water observed by tapping-mode atomic force microscopy. *Langmuir*, 16:6377–6380, 2000.

[30] X.H. Zhang, X.D. Zhang, S.T. Lou, Z.X. Zhang, J.L. Sun, and J. Hu. Degassing and temperature effects on the formation of nanobubbles at the mica/water interface. *Langmuir*, 20:3813–3815, 2004.

[31] R.F. Considine, R.A. Hayes, and R.G. Horn. Forces measured between latex spheres in aqueous electrolyte: Non-dlvo behavior and sensitivity to dissolved gas. *Langmuir*, 15:1657–1659, 1999.

[32] W.M. Haynes, editor. CRC Handbook of Chemistry and Physics. CRC Press, 91 edition, 2010.

[33] E.L. Cussler. *Diffusion - mass transfer in fluid systems*. Cambridge University Press, Cambridge, United Kingdom, 1984.

[34] P. Han and D.M. Bartels. Temperature dependence of oxygen diffusion in H_2O and D_2O. *Journal of Physical Chemistry*, 100:5597–5602, 1996.

[35] B.J. Kirby, D.S. Reichmuth, R.F. Renzi, T.J. Shepodd, and B.J. Wiedenman. Microfluidic routing of aqueous and organic flows at high pressurs: fabrication and characterization of integrated polymer microvalve elements. *Lab on a Chip*, 5:184–190, 2005.

[36] B. Ilic, D. Czaplewski, P. Neuzil, T. Stanczyk, J. Blough, and G.J. Maclay. Preparation and characterization of platinum black electrodes. *Journal of Materials Science*, 38:3447–3457, 2000.

[37] B.J. Kirby and E.F. Jr. Hasselbrink. Zeta potential of microfluidic substrates: 1. theory, experimental techniques, and effects on separations. *Electrophoresis*, 25:203–213, 2004.

[38] P.J. Scales, F. Grieser, and T.W. Healy. Electrokinetics of the silica-solution interface: A flat plate streaming potential study. *Langmuir*, 8:965–974, 1992.

[39] M. Kosmulski and E. Matijevic. Zeta potentials of silica in water-alcohol mixtures. *Langmuir*, 8:1060–1064, 1992.

[40] J.E. Dickens, J. Gorse, J.A. Everhart, and M. Ryan. Dependence of electroosmotic flow in capillary electrophoresis on group i and ii metal ions. *Journal of Chromatography B*, 657:401–407, 1994.

[41] S. Lou, J. Gao, X. Xiao, X. Li, G. Li, Y. Zhang, M. Li, J. Sun, X. Li, and J. Hu. Studies of nanobubbles produced at liquid/solid interfaces. *Materials Characterization*, 48:211–214, 2002.

[42] J.W.G. Tyrrell and P. Attard. Images of nanobubbles on hydrophobic surfaces and their interactions. *Physical Review Letters*, 87(17), 2001.

[43] J.W.G. Tyrrell and P. Attard. Atomic force microscope images of nanobubbles on a hydrophobic surface and corresponding force-separation data. *Langmuir*, 18:160–167, 2002.

[44] N.V. Churaev, J. Ralston, I.P. Sergeeva, and V.D. Sobolev. Electrokinetic properties of methylated quartz capillaries. *Advances in Colloid and Interface Science*, 96:265–278, 2002.

[45] L. Joly, C. Ybert, E. Trizac, and L. Bocquet. Hydrodynamics within the electric double layer on slipping surfaces. *Physical Review Letters*, 93:257805, 2004.

[46] C.I. Bouzigues, P. Tabeling, and L. Bocquet. Nanofluidics in the Debye layer at hydrophilic and hydrophobic surfaces. *Physical Review Letters*, 101:114503, 2008.

[47] T.M. Squires. Electrokinetic flows over inhomogeneously slipping surfaces. *Physics of Fluids*, 20:092105, 2008.

[48] A.S. Khair and T.M. Squires. The influence of hydrodynamic slip on the electrophoretic mobility of a spherical colloidal particle. *Physics of Fluids*, 21:042001, 2009.

[49] M.P. Brenner and D. Lohse. Dynamic equilibrium mechanism for surface nanobubbles. *Phys. Rev. Lett.*, 101:214505, 2008.

[50] H. Sato, N. Matubayasi, M. Nakahara, and F. Hirata. Which carbon oxide is more soluble? ab initio study on carbon monoxide and dioxide in aqueous solution. *Chemical Physics Letters*, 323:257–262, 2000.

[51] G.K. Anderson. Enthalpy of dissociation and hydration number of carbon dioxide hydrate from the clapeyron equation. *J. Chem. Thermodynamics*, 35:1171–1183, 2003.

[52] A. Khan. Theoretical studies of $CO_2(H_2O)$ 20,24,28 culsters: stabilization of cages in hydrates by CO_2 guest molecules. *J. Mol. Struct. (Thermochem)*, 664-665:237–245, 2003.

CHAPTER 6

FUNDAMENTALS OF MICROFLUIDICS FOR HIGH SCHOOL PHYSICS STUDENTS WITH NO PRIOR KNOWLEDGE OF FLUID MECHANICS

6.1 Abstract

Three microfluidics-based laboratory exercises were developed and implemented in a high school physics classroom. The first exercise demonstrated ways in which flows are characterized, including viscosity, turbulence, shear stress, reversibility, compressibility, and hydrodynamic resistance. Students characterized flows in PDMS microfluidic devices in the other two exercises, where they observed the mixing characteristics of laminar flows, and conservation of volumetric flow rate for incompressible flows. In surveys, the students self-reported increased knowledge of microfluidics, and an improved attitude toward science and nanotechnology.

6.2 Introduction

Inquiry-based learning, learning by posing questions and designing experiments to answer them, has the potential to both improve science education, and to motivate previously uninterested students when incorporated alongside more traditional pedagogy [1, 2]. A positive attitude toward science, in particular, has been shown to correlate with achievement, and incorporation of hands-on activities tends to improve attitudes toward science [1]. In addition to incorporating more inquiry-based laboratory exercises, the

[0]The content of this chapter is a draft of a manuscript that was invited to be submitted as a book chapter in "Methods in Molecular Biology Microfluidic Diagnostics".

Figure 6.1: Teaching staff that implemented these lab exercises at Whitney Point High School in Whitney Point, NY. From left to right: Vishal Tandon (Cornell University, Ithaca, NY), Walter Peck (Physics Teacher), and Matt Beattie (Student Teacher, SUNY Cortland, Cortland, NY).

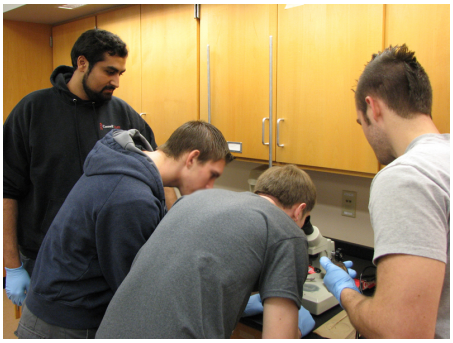

(a)

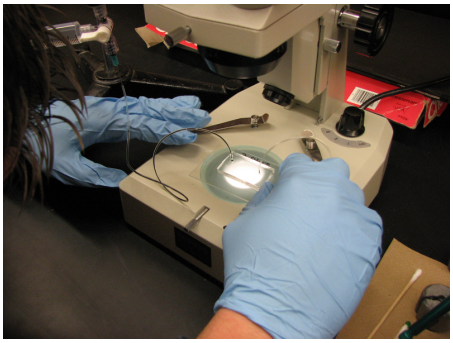

(b)

Figure 6.2: Pictures of students engaged in working on analyzing flows in PDMS microfluidic devices. In (a), Vishal Tandon (far left) supervises.

inclusion of cutting-edge research topics has been proposed as a way of improving attitudes toward science [3].

One example of a rapidly growing field of modern research is microfluidics, which has applications in bioanalysis, chemical synthesis, and point-of-care medical diagnostic devices [4]. Microfluidics is an interdisciplinary area of research, that traditionally, would be considered too specialized to be taught at the K–12 level. Many high school physics students have had little or no training in fluid mechanics at all, as it

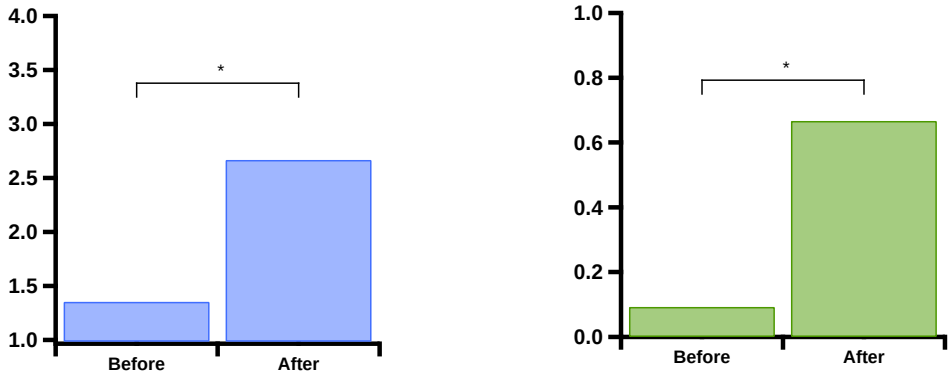

(a) (b)

Figure 6.3: (a) Self-reported understanding of what microfluidics is, on a scale of 1–4 (1 indicates no understanding, whereas 4 indicates a strong understanding). (b) Fraction of students that claim the ability to give an example of microfluidics in everyday life. $p < 10^{-9}$ and $n = 54$ for both data sets.

is often not emphasized in standard, state-sanctioned curricula (see, for example, [5]). Microfluidics-based laboratory exercises have the potential to increase student education in several areas, including: fluids, mechanics, chemistry, biology, and electromagnetism.

The laboratory activities described in the following sections were successfully implemented in a physics classroom at Whitney Point High School (Whitney Point, NY), led by Walter Peck (physics teacher) and Vishal Tandon (Ph.D. student in biomedical engineering, Cornell University)(Figure 6.1). Students engaged in three lab activities; one designed to teach basic fluid mechanics (Section 6.4.1), and two that allowed students to characterize flows in PDMS microfluidic devices (Sections 6.4.2 and 6.4.3, Figure 6.2). Honors students also designed their own method for measuring average fluid velocities in microfluidic devices.

Students initially reported little or no understanding of microfluidics, but indicated an improvement in their knowledge of the field after participating in the exercises (Figure 6.3). In addition, 9 out 22 students in the honors class indicated that they would be

more interested in doing research in science after the activity, and 6 out of the 22 students indicated that they would be more interested in doing research in nanotechnology specifically. The activities described here were also integrated as curricula as part of the CLIMB (Cornell's Learning Initiative in Medicine and Bioengineering) program [6].

6.3 Materials

6.3.1 Basic Fluid Mechanics

1. Deionized Water[1]
2. Dye (e.g. Food Coloring)
3. Glycerin[2] (Sigma Aldrich, St. Louis, MO)
4. Transfer Pipettes
5. Stirring Sticks
6. 5 mL BD Luer–Lok plastic syringes (VWR, West Chester, PA)
7. Luer–Lok Adapters (Labsmith, Livermore, CA, Catalog #C360–300)
8. Plugs (Labsmith, Livermore, CA, Catalog #C360–101)
9. PEEK fittings for 360 μm capillaries (Labsmith, Livermore, CA, Catalog #C360–100)
10. 60 mm petri dishes (VWR, West Chester, PA)
11. 100 mm petri dishes (VWR, West Chester, PA)
12. Silica Capillary[3] — 360 μm OD/100 μm ID (Polymicro Technologies, Phoenix, AZ, Catalog #TSP100375)

6.3.2 Laminar Flow PDMS Device

1. Laminar Flow PDMS Device[4]
2. 23 Ga. Tygon tubing fit with stainless steel pins[5]
3. 5 mL BD Luer–Lok plastic syringes (VWR, West Chester, PA)
4. 23 Ga. Syringe Needles[6] (VWR, West Chester, PA)
5. Deionized Water
6. Dye (Food Coloring)
7. Microscope
8. Cotton Swabs
9. Syringe Pump[7] (with space for at least 2 syringes)

6.3.3 Step-Down Device

1. Straight Channel Step-Down PDMS Device[4]
2. 23 Ga. Tygon tubing fit with stainless steel pins[5]
3. 5 mL BD Luer–Lok plastic syringes (VWR, West Chester, PA)
4. 23 Ga. Syringe Needles (VWR, West Chester, PA)[6]
5. Deionized Water
6. Dye (Food Coloring)
7. Fluorinert Solution (3M, St. Paul, MN)
8. Microscope
9. Cotton Swabs
10. Syringe Pump[7]

11. Ruler
12. Stopwatch

6.4 Methods

6.4.1 Basic Fluid Mechanics

This laboratory exercise is intended to give students a basic understanding of different ways in which fluids are characterized, and how flows can change dramatically depending on the nature of the fluid involved, the speed of flow, and the size of the system. In particular it focuses on giving students an intuitive understanding of viscosity, turbulence, reversibility of Stokes Flow, compressibility, and hydraulic resistance.

Preparation to be done by the teacher

1. Photocopy printed materials (lab instructions for the students)
2. For each group of students, prepare 4 beakers of solution;
    - Glycerin
    - Water
    - Dyed Glycerin
    - Dyed Water
3. For each group of students, place the lid of a 60 mm Petri dish into the base of a 100 mm dish. Pour glycerin into the 100 mm dish so that it surrounds, but does not cover the 60 mm lid.

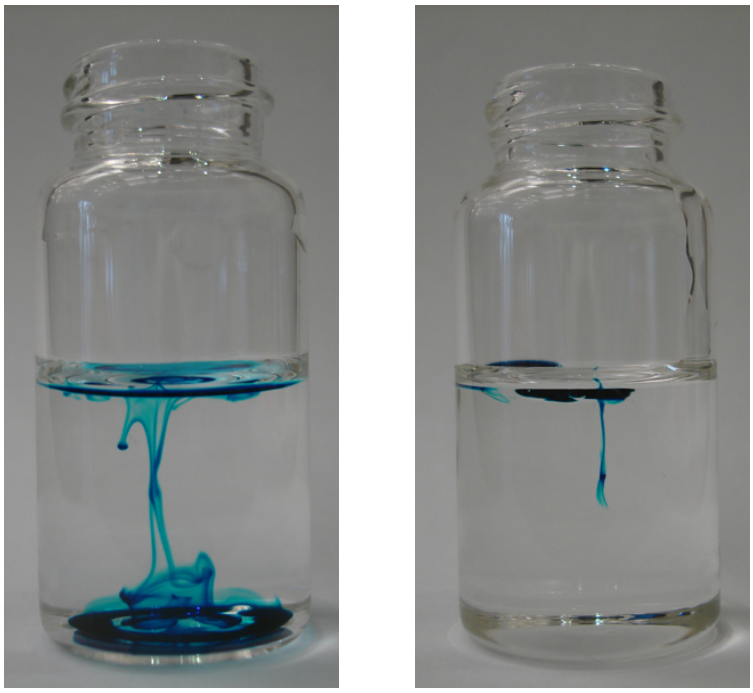

(a) (b)

Figure 6.4: Comparison of relatively low viscosity flow of dye in water to relatively high viscosity flow of dye in glycerin. (a) A drop of dye is added to water, and photographed after about 5 s. (b) A drop of dye is added to glycerin, and photographed after about 5 s. Some of the dye was pushed down with a transfer pipette to make it visible in the picture. With stirring, this is also a demonstration of high (water) vs. low (glycerin) Re flow.

4. Fill one 5 ml syringe with air, and one with water. Plug the ends of the syringes using Labsmith Luer–Lok adapters and plugs [9].

5. Fill two 5 ml syringes with water. Using Labsmith Luer–Lok adapters and PEEK fittings, attach a 3 cm length of silica capillary to each syringe, one with ID 100 μm, and one with ID 25 μm.

6. Allocate stirring sticks and transfer pipettes for each group.

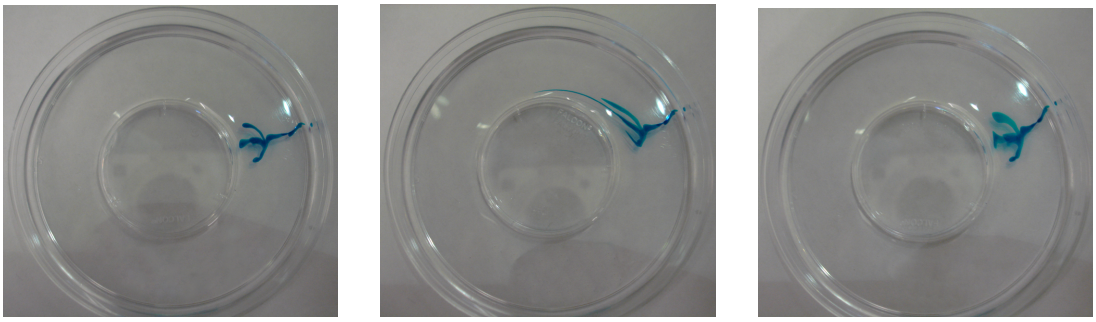

(a) (b) (c)

Figure 6.5: Experiment that demonstrates the reversibility of Stokes Flow. (a) A pattern is drawn with dye in glycerin. (b) The center Petri dish is rotated counter-clockwise, causing shear and deforming the pattern. (c) The center Petri dish is rotated clockwise, reversing the deformation and (nearly) restoring the original pattern.

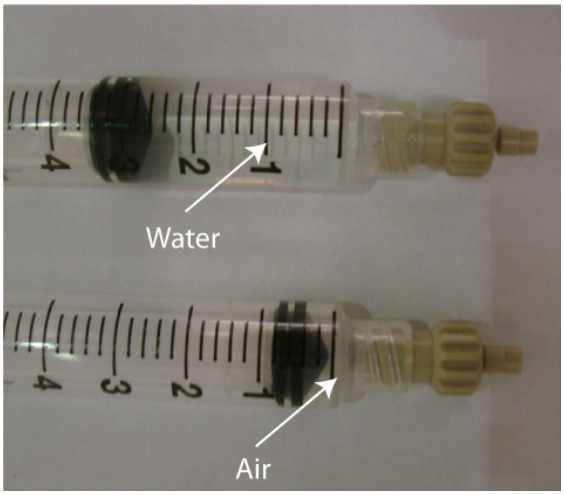

Figure 6.6: Demonstration of fluid compressibility. The top syringe was initially filled with 3 ml of water, while the bottom syringe was initially filled with 3 ml of air. Both syringes are sealed at their ends. After depressing the plunger of each syringe (by hand), the air reduces in volume, while the water does not.

Student Experimental Procedure

1. Give students a few minutes to observe the water and glycerin utilizing the stirring sticks. Point out that the glycerin is more viscous than water, and ask them to write down what viscosity means based on their observations.

2. Using a transfer pipette, students add a drop of dye to the water beaker without

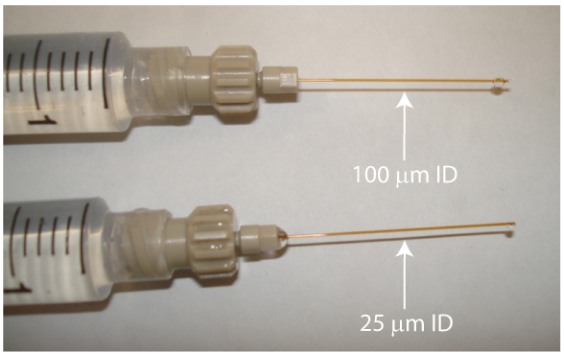

Figure 6.7: Demonstration of hydraulic resistance. For the same applied pressure, flow rates are much large in the capillary with 100 μm ID than for the capillary with 25 μm ID. This can be seen by the size of the droplets at the outlets pictured above. Students applied pressure by hand, giving them a tactile demonstration of hydraulic resistance as well (they found it harder to push fluid through the smaller capillary).

stirring. They should write down their observations of the resulting flow, and they should pay close attention as to whether or not the fluid is mixing. Ask students if they think the fluids can be "unmixed." Students can stir the fluid, and estimate the time it takes for the fluids to fully mix.

3. Repeat step 2 with the glycerin beaker. In addition to asking students the same questions as in step 2, point out the differences between turbulent (water) and laminar (glycerin) flow (Figure 6.4), and ask students which they think is more difficult to model mathematically.

4. Using a transfer pipette, students add dye to the glycerin in the 100 mm petri dish. They should draw a simple, recognizable pattern, such as a square or circle (Figure 6.5).

5. Have students rotate the 60 mm petri dish (keeping its position fixed concentric with the 100 mm dish) slowly, about a half turn. Ask students to describe the deformation pattern of the dye, noting how it changes as a function of distance from the rotating dish.

6. Ask students to rotate the 60 mm dish the back to the starting position by rotating

slowly in the opposite direction. Students should comment on the resulting pattern (it should be very similar to the starting pattern). This is a crude demonstration of the reversibility of Stokes flow.

7. Give students a set of plugged syringes; one filled with air, and one filled with water. Ask students which fluid they think they will be able to compress by pressing down on the plunger of the syringe. Students should then attempt to compress each of the fluids; they can write down a rough quantitative estimate of compression by noting the change in volume as measured by the graduations on the syringes (Figure 6.6). It should be clear that the air is compressible, while the water is not. Ask students how they know that the air is actually being compressed, and not leaking out of the syringe (the answer is that the plunger rebounds to its original position when released).

8. Give students a set of water-filled syringes with silica capillaries attached; one with a 25 μm inner diameter (ID) and one with a 100 μm ID. Students should try to force water to flow out of a given capillary by pushing on the syringe plunger. Upon comparing the two capillaries, students will find that it is much easier to push fluid through the larger capillary (Figure 6.7). Ask students whether this difference is proportional to the size difference between the capillaries (factor of 4), or whether it is larger or smaller (it takes a pressure gradient 16 time larger to drive fluid at the same flow rate in a capillary that has a diameter a factor of 4 smaller). Make analogies to electrical circuits and resistivity, as they are much more likely to have been covered in a standard high school physics curriculum.

6.4.2 Laminar Flow PDMS Device

Devices fabricated from poly(dimethylsiloxane) (PDMS) are ubiquitous in microfluidics for bioanalytical applications [4, 7]. Protocols for inexpensive Jell–O based devices that demonstrate fabrication and laminar flow have been developed previously [8]. Here we present experiments that utilize actual, small-scale PDMS devices, and do not focus on fabrication. The challenges in implementing such devices in a high school classroom include; (a) fabrication is expensive and will likely require assistance/donation from a local university[10], (b) working with them requires microscopes, and (c) working with these devices is non-trivial, and may frustrate less-motivated students. The advantages of using real PDMS devices include; (a) students get a visual sense of how small microfluidic devices are, (b) students will learn about challenges in interfacing microfluidic devices with the macroscopic world, and (c) using pre-fabricated devices shortens the length of the activity to one class period (approximately 1 hour). Fabrication protocols for PDMS devices are established elsewhere [6, 7, 9], so we do not present details here. Briefly, masters were patterned in SU–8 photoresist on Si wafers using UV lithography, developed, and cured. PDMS was poured over the masters, cured with a cross linker, peeled off the master, and bonded to glass slides to make the completed devices.

The laminar flow PDMS device (Figure 6.8) consists of two inlets and two outlets. The inlet channels converge into a single channel, and then diverge again at the outlets. It is designed to demonstrate how low Re flow may differ from students' intuitions, which are likely based on high Re flow. Students will expect the fluids to mix in the single channel, but the fluids will remain mostly separated since convective transport from the inlet to the outlet dominates over diffusive transport in the transverse direction.

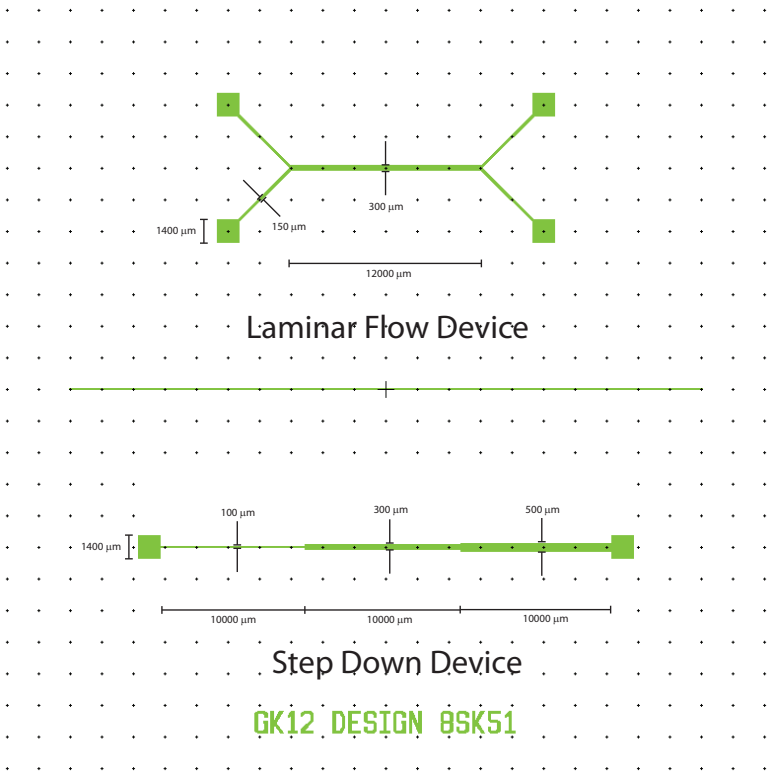

Figure 6.8: CAD drawings of two PDMS devices; one that demonstrates laminar flow (top), and one that demonstrates constant flow rate for an incompressible fluid (bottom). These devices were designed and fabricated by Sowmya Kondapalli at Cornell University.

Preparation to be done by the teacher

1. Photocopy printed materials (lab instructions for the students)
2. For each group of students, set up a microscope, a laminar flow device, inlet and outlet tygon tubing, two syringes, two syringe needles, and beakers with dye and with clear water (or dye of a different color). The dye should be concentrated; otherwise it is difficult to see at small scales.
3. Set up a syringe pump or clamp stands with clamps and weights at each station (Figure 6.9) depending on whether syringe pumps are available[7].

Student experimental procedure

1. Draw 2 ml of the dye into one 5 ml syringe, and 2 ml of water (or dye of a different color) into another syringe.
2. Attach syringe needles to both syringes. Leave the caps on the needles while you are doing this.
3. Mount the syringes on the syringe pump.
4. Remove the caps from the needles and slide tygon tubes onto them. Use the end of the tube that does not have a pin.
5. Place the laminar flow PDMS device onto the microscope stand, and insert the pins from the tygon tubes connected to the syringes into the inlets of the device (the device is symmetrical, so either side is fine). There are holes punctured in the PDMS where you should put the pins.
6. Connect two tygon tubes to the outlets of the device, pushing the pin ends of the tubes into the holes in the PDMS. These tubes should go to a waste container
7. Bring the center part of the device into focus in the microscope.
8. Lightly press on one syringe fill the channel with dye solution[11] (this may temporarily require removing it from the syringe pump).
9. Set the syringe pump to infusion mode at 10 μl/h. Adjust the flow rate as necessary[12].
10. Observe the flow with the microscope, and record your observations[13].
11. Move the chip so that you're looking at the branch point near the outlets. Record your observations.

6.4.3 Step-Down PDMS Device

The step-down flow PDMS device (Figure 6.8) consists of one channel that reduces in size in three stages. As fluid travels from a wider channel to a smaller one, the average fluid velocity must increase (for an incompressible flow) in order to maintain conservation of mass. This device is designed to allow students to observe, and potentially quantify these velocity changes.

Preparation to be done by the teacher

1. Photocopy printed materials (lab instructions for the students)
2. For each group of students, set up a microscope, a step-down flow device, inlet and outlet tygon tubing, two syringes, two syringe needles, and beakers with dye and fluorinert solution. The dye should be concentrated; otherwise it is difficult to see at small scales.
3. Set up a syringe pump or clamp stands with clamps and weights at each station (Figure 6.10) depending on whether syringe pumps are available.
4. Have rulers and stopwatches available to allow students to come up with a way to quantify velocity changes.

Student experimental procedure

1. Draw 2 ml of food dye solution into one 5 ml syringe. Try to remove all the air bubbles from the syringe.
2. Draw 2 ml of fluorinert into another 5 ml syringe. Fluorinert is a liquid that is immiscible with water, but has similar viscosity. Again, remove the air bubbles.

3. Connect both syringes to the two-way valve using the Luer–Lok connection. Screw them in tightly so that they don't leak.

4. Screw a syringe needle onto the two-way valve. Leave the cap on the syringe needle while you do this.

5. Mount the food dye syringe onto the syringe pump[14]. The fluorinert syringe will be at a right angle to the dye syringe. Make sure it is accessible, and not obstructing anything.

6. Remove the cap from the syringe needle, and slide a tygon tube over it (the end that does not have a pin in it).

7. Place the step-down PDMS device on the microscope stage, and insert the pin from the tygon tube connected to the syringe needle into the inlet of the device (the side with the widest channel).

8. Place a pin from another tygon tube into the outlet of the device. The other end of the tube should go into a waste container.

9. The valve stops flow in the direction it's pointing. Turn the valve toward the food dye syringe. Gently press on the fluorinert syringe to fill the device. Fluorinert is transparent, so it may be difficult to see it in the channel. Watch for fluid coming out of the outlet[11].

10. Turn the valve to the fluorinert syringe. Manually apply pressure from the syringe pump until dye solution fills the inlet tube and is about to enter the device. Set the syringe pump infusion rate to 10 μL/hr. The infusion rate can be adjusted as necessary[15].

11. Observe the interface between the dye and the fluorinert solution moving through the channel. Pay attention to how the flow velocity changes as the interface moves through the smaller sections of the channel. If the interface is lost, the valve may

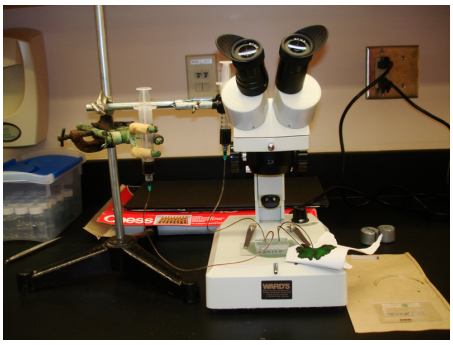

(a)

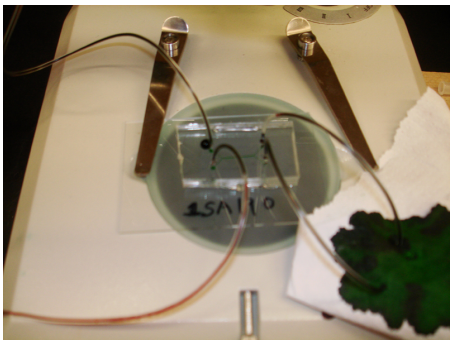

(b)

Figure 6.9: (a) Overview of the experimental setup for studying the laminar flow PDMS device on a microscope. (b) Close-up picture of the laminar flow PDMS device set up on a microscope.

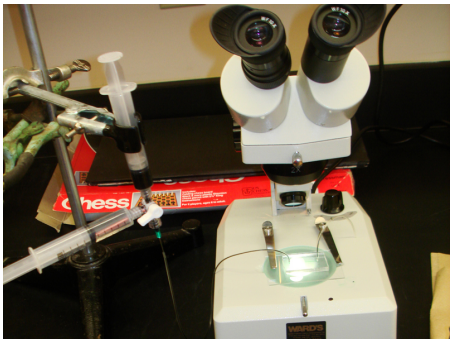

(a)

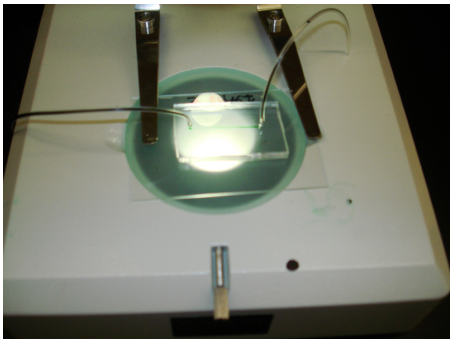

(b)

Figure 6.10: (a) Overview of the experimental setup for studying the step-down PDMS device on a microscope. (b) Close-up picture of the step-down PDMS device set up on a microscope.

be turned and plugs of fluorinert can be injected. An optical interface is necessary in order to observe the fluid velocity[16].

12. Design an experiment to quantitatively measure the speed with which the interface moves through the step-down device[17].

Notes

[1]Some standard laboratory equipment is listed in the materials section, since it may not be commonly found in a high school classroom.

[2]Corn syrup may be substituted, but is messier to work with.

[3]Silica capillary may be too expensive to buy for the classroom, though it may be possible to obtain samples from Polymicro or other capillary manufacturers. Only a few cm of capillary are necessary, and they can be reused.

[4]Protocols for fabricating PDMS devices are available [6, 7, 9], though they may be difficult to implement in a high school setting. Collaboration with a local university is recommended.

[5]$\sim$ 0.5 cm pins are cut from stainless steel tubing with an outer diamter of 0.025" (McMaster–Carr, Princeton, NJ). The steel tubing should be cut with a saw or Dremel tool to ensure that the ends are not pinched off. It is easier to insert a long stainless steel tube into a tygon tube, and cut the steel tube off to the desired length.

[6]For safety concerns, blunt syringe needles may be used instead of standard needles, though standard needles are easier to work with.

[7]A syringe pump enables precise control of flow rates, allowing students to make quantitative measurements. Syringe pumps are expensive, and may not be available, however. If syringe pumps are not available, an alternative method using clamp stands, clamps, and weights may be used. Syringes are clamped in a vertical position with the plunger on top and the needle below. A mass may be balanced on the plunger to apply pressure, and students can estimate the pressure by dividing the weight of the mass by the area of the plunger ($\frac{4mg}{\pi d^2}$).

[8]Time in a high school classroom tends to be extremely limited. Any preparation for the activity that is not an explicit part of the experiment and does not aid in teaching the students should be done ahead of time.

[9]Labsmith fittings are expensive, so the syringes can be plugged in some other way (e.g. with epoxy)

if necessary.

[10]It may also be possible to purchase and use capillary electrophoresis devices, though they may be expensive

[11]The device may leak at the inlet if the pressure is too high. If this happens, clean up the leak with a cotton swab or a napkin.

[12]If using the clamp stand setup, use the following procedure instead: Try to press on both syringes equally. Once you get both fluids into the channel, balance the weights on top of the plungers so that you apply a roughly equal pressure to both syringes. Use what you know about force and pressure to estimate the pressure applied

[13]Students may get frustrated if they have trouble setting up the device. Try to give them new things to try if this happens, e.g. a new device, reversing the direction of the device, different inlet/oulet tubing, etc. Avoid setting the device up for them, though since time is limited, it may become necessary.

[14]If no syringe pump is available, mount the food dye syringe to a clamp stand using a clamp, such that the plunger is facing vertically upward. The fluorinert syringe will be at a right angle (parallel to the lab bench) to the dye syringe.

[15]If no syringe pump is available, apply pressure to the food dye syringe either by hand or by carefully balancing a weight on top of the plunger for the syringe. Using the weight gives you a quantitative estimate of the applied pressure.

[16]Tracer particles, such as polystyrene beads are often used to observe the velocity field. In order for the particles to be visible, they either need to be large enough, or fluorescently labeled and observed in a fluorescence microscope. For the former, challenges arise from particle sedimentation, and for the latter, an expensive fluorescence microscope is necessary; something not commonly found in high schools. In addition, the tracer particles are expensive as compared to fluorinert solution

[17]Give students stopwatches and rulers at this point. It may also be useful to give students a diagram showing the dimensions of the device, and an equation for the hydraulic resistance of a rectangular channel ($R = \frac{12\mu L}{1-0.63(h/w)}\frac{1}{h^3 w}$)

6.5 Acknowledgements

We would like to acknowledge our funding source, NSF GK–12 (Grant # 0841291). We would also like to think to thank: Whitney Point High Schohol (Whitney Point, NY) for allowing us to work with students; Brian J. Kirby (Sibley School of Mechanical Engineering, Cornell University, Ithaca, NY) for useful discussion, and for donating equipment and resources; Michael Shuler, Chris B. Schaffer, and Shivaun Archer (Department of Biomedical Engineering, Cornell University) for their guidance and suggestions; Nev Singhota and Kevin Dilley (Biomedical Engineering GK–12 Coordinators, Cornell University) for their organizational efforts.

BIBLIOGRAPHY

[1] M.P. Freedman. Relationship among laboratory instruction, attitude toward science, and achievement in science knowledge. *Journal of research in science teaching*, 34(4):343–357, 1997.

[2] R.D. Anderson. Reforming science teaching: what research says about inquiry. *Journal of Science Teacher Education*, 13(1):1–12, 2002.

[3] *http://www.gk12.org*.

[4] H.A. Stone, A.D. Stroock, and A. Ajdari. Engineering flows in small devices: Microfluidics toward a lab-on-a-chip. *Annual Review of Fluid Mechanics*, 36:381–411, 2004.

[5] *http://www.p12.nysed.gov/ciai/mst/sci/ls*.

[6] *http://climb.bme.cornell.edu/flow.php*.

[7] J.C. McDonald, D.C. Duffy, J.R. Anderson, D.T. Chiu, H. Wu, O.J.A. Schueller, and G.M. Whitesides. Fabrication of microfluidic systems in poly(dimethylsiloxane). *Electrophoresis*, 21:27–40, 2000.

[8] C.W.T. Yang, E. Ouellet, and E.T. Lagally. Using inexpensive Jell-O chips for hands-on microfluidics education. *Analytical Chemistry*, 82:5408–5414, 2010.

[9] S. Kondapalli and B.J. Kirby. Refolding of beta-galactosidase: microfluidic device for reagent metering and mixing and quantification of refolding yield. *Microfluid Nanofluid*, 7:275–281, 2009.

CHAPTER 7

CONCLUSIONS

The primary goal of this work was to characterize electrokinetics in hydrophobic microfluidic substrates with aqueous working solutions as a function of history of the fluid–solid interface. We have shown that in hydrophobic substrates, the electrokinetic potential is a function of time after (i) initial formation of the fluid–solid interface, and (ii) exchanging water as the solvent in the system for ethanol. The time dependence is affected by exposure to electric fields (which result in electroosmotic flow) and the ambient pressure of the air surrounding the system. In hydrophilic substrates, no such dependence of the electrokinetic potential on the history of the fluid–solid interface was observed.

7.1 Summary of Accomplishments

In **Chapters 2 and 3**, we identified the main challenges in modeling electrokinetics in hydrophobic substrates: the origin of surface charge is unknown, the potential presence of slip leads to a poorly defined fluid velocity boundary condition, and the physical structure of the fluid–solid interface is complex and poorly understood. We measured the electrokinetic potential as a function of pH for several hydrophobic substrates (PTFE, Zeonor, TOPAS), and showed that with careful experiments, the electrokinetic properties of a given material were consistent for different measurement techniques and different substrate manufacturers. Based on our experiments, spectroscopic data [1], and molecular dynamics simulations [2–9], we concluded that hydroxyl ion adsorption best explains surface charge on hydrophobic substrates, though further study is needed.

We demonstrated that the electrokinetic potential is a function of the history of the

fluid–solid interface in TOPAS and Zeonor substrates. In these substrates (but not in silica), the electrokinetic potential is initially large in magnitude immediately after formation of the fluid–solid interface, and the magnitude decays exponentially with a time constant that is on the order of hours (**Chapters 4 and 5**). In **Chapter 4**, we show that the initial magnitude of the electrokinetic potential is greatly reduced when the system is briefly (12 min) exposed to an electric field. In addition, exchanging water as the solvent in the system for ethanol results in an electrokinetic potential that is initially large and decays as well.

The kinetics governing the approach of the electrokinetic potential of a water–Zeonor system to equilibrium are a function of the ambient air pressure. In **Chapter 5**, we presented time-resolved measurements of the electrokinetic potential of Zeonor at various sub-atmospheric ambient pressures. At lower ambient pressures, the approach of the electrokinetic potential to equilibrium is faster. Once the electrokinetic potential has reduced in magnitude at low ambient air pressure, increasing the air pressure does not increase it again, suggesting hysteresis of the electrokinetic potential with solution dissolved gas content. The dependence on ambient pressure and ethanol–water solvent exchanges strongly suggests that the amount of dissolved gas in solution must be considered among the parameters that affect the electrokinetic potential.

7.2 Future Work

The origin of charge in hydrophobic substrates is still unclear. Further study should be focused on (i) bridging thermodynamic models with experimental data, and (ii) attempting to isolate the effects of each of the charge forming mechanisms independently through carefully designed experiments. Examination of the temperature dependence of

these systems can lead to progress with the former, as chemical equilibria and ion distributions are both temperature-dependent. For the latter, there are several experiments which would lead to progress in this field, e.g.: (a) a methodical study of the effects of impurities, where impurities are implanted into a hydrophobic microfluidic substrate, and (b) electrokinetic characterization of hydrophobic substrates using solutions of high (> 0.1 M) salt concentration.

The effect of dissolved gasses on time-dependent electrokinetic phenomena in hydrophobic substrates can be further explored by investigating different types of gases. Carbon dioxide is of particular interest, owing to its anomalously high solubility in aqueous solutions [10–12]. Because the concentration of dissolved gas in solution is also a strong function of temperature, the temporal dependence of the electrokinetic potential is also expected to vary with temperature cycling. The chemical reactions leading to surface charge and condensed ion distributions are also functions of temperature, however, so modeling temperature effects are more challenging.

The link between nanobubbles and macroscopically observable electrokinetic phenomena can be strengthened by direct observation of nanobubble dynamics via AFM. Nanobubbles have been observed to exist at water–hydrophobe interfaces for hours [13–16]; their lifetime is similar to the time scale of our observed electrokinetic-potential decays. A measurement of the fraction of substrate surface covered by nanobubbles as a function of time can demonstrate whether nanobubble decay rates are quantitatively similar to electrokinetic potential decay rates.

BIBLIOGRAPHY

[1] C. Raduge, V. Pflumio, and Y.R. Shen. Surface vibrational spectroscopy of sulfuric acid-water mixtures at the liquid-vapor interface. *Chemical Physics Letters*, 274(1):140–144, 1997.

[2] C.Y. Lee, J.A. McCammon, and P.J. Rossky. The structure of liquid water at an extended hydrophobic surface. *Journal of Chemical Physics*, 80(9):4448–4455, 1984.

[3] J.R. Grigera, S.G. Kalko, and J. Fischbarg. Wall-water interface. a molecular dynamics study. *Langmuir*, 12:154–158, 1996.

[4] S.I. Mamatkulov, P.K. Khabibullaev, and RR. Netz. Water at hydrophobic substrates: Curvature, pressure, and temperature effects. *Langmuir*, 20:4756–4763, 2004.

[5] L. Joly, C. Ybert, E. Trizac, and L. Bocquet. Hydrodynamics within the electric double layer on slipping surfaces. *Physical Review Letters*, 93:257805, 2004.

[6] L. Vrbka, M. Mucha, B. Minofar, and P. Jungwirth. Propensity of soft ions for the air/water interface. *Current Opinion in Colloid and Interface Science*, 9:67, 2004.

[7] R. Zangi and J.B.F.N. Engberts. Physisorption of hydroxide ions from aqueous solution to a hydrophobic surface. *Journal of the American Chemical Society*, 127:2272–2276, 2005.

[8] D.M. Huang, C. Cottin-Bizonne, C. Ybert, and L. Bocquet. Ion-specific anomalous electrokinetic effects in hydrophobic nanochannels. *Physical Review Letters*, 98:177801, 2007.

[9] D.M. Huang, C. Cottin-Bizonne, C. Ybert, and L. Bocquet. Aqueous electrolytes near hydrophobic surfaces: Dynamic effects of ion specificity and hydrodynamic slilp. *Langmuir*, 24(4):1442–1450, 2007.

[10] H. Sato, N. Matubayasi, M. Nakahara, and F. Hirata. Which carbon oxide is more soluble? ab initio study on carbon monoxide and dioxide in aqueous solution. *Chemical Physics Letters*, 323:257–262, 2000.

[11] G.K. Anderson. Enthalpy of dissociation and hydration number of carbon dioxide hydrate from the clapeyron equation. *J. Chem. Thermodynamics*, 35:1171–1183, 2003.

[12] A. Khan. Theoretical studies of $CO_2(H_2O)$ 20,24,28 culsters: stabilization of cages in hydrates by CO_2 guest molecules. *J. Mol. Struct. (Thermochem)*, 664-665:237–245, 2003.

[13] P. Attard. Electrolytes and the electric double layer. *Advances in Chemical Physics*, 92:1–159, 1996.

[14] P. Attard. Thermodynamic analysis of bridging bubbles and a quantitative comparison with the measured hydrophobic attraction. *Langmuir*, 16:4455–4466, 2000.

[15] P. Attard, M.P. Moody, and J.W.G. Tyrell. Nanobubbles: the big picture. *Physica A*, 314:696–705, 2002.

[16] P. Attard. Nanobubbles and the hydrophobic attraction. *Advances in Colloid and Interface Science*, 104:75–91, 2003.